COASTAL WAVE GENERATION AND WAVE BREAKING OVER TERRAIN: TWO PROBLEMS IN MESOSCALE WAVE DYNAMICS

A Dissertation

by

TINGTING QIAN

Submitted to the Office of Graduate Studies of
Texas A&M University
in partial fulfillment of the requirements for the degree of

DOCTOR OF PHILOSOPHY

May 2009

Major Subject: Atmospheric Sciences

COASTAL WAVE GENERATION AND WAVE BREAKING OVER TERRAIN: TWO PROBLEMS IN MESOSCALE WAVE DYNAMICS

A Dissertation

by

TINGTING QIAN

Submitted to the Office of Graduate Studies of
Texas A&M University
in partial fulfillment of the requirements for the degree of

DOCTOR OF PHILOSOPHY

Approved by:

Co-Chairs of Committee,	Craig C. Epifanio
	Fuqing Zhang
Committee Members,	John Nielsen-Gammon
	Robert Hetland
Head of Department,	Kenneth Bowman

May 2009

Major Subject: Atmospheric Sciences

ABSTRACT

Coastal Wave Generation and Wave Breaking over Terrain: Two Problems in Mesoscale Wave Dynamics. (May 2009)

Tingting Qian, B.S., Nanjing University;

M.S., Peking University

Co–Chairs of Advisory Committee: Dr. Craig C. Epifanio
Dr. Fuqing Zhang

Two problems in mesoscale wave dynamics are addressed: (i) wave-turbulence interaction in a breaking mountain wave and (ii) gravity wave generation associated with coastal heating gradients.

The mean and turbulent structures in a breaking mountain wave are considered using an ensemble of high-resolution (essentially LES) wave-breaking calculations. A turbulent kinetic energy budget for the wave shows that the turbulence production is almost entirely due to the mean shear. Most of the production is at the top of the leeside shooting flow, where the mean-flow Richardson number is persistently less than 0.25. Computation of the turbulent heat and momentum fluxes shows that the dissipation of mean-flow wave energy is due primarily to the momentum fluxes. The resulting drag on the leeside shooting flow leads to a loss of mean flow Bernoulli function as well as a cross-stream PV flux. The dependence of both the resolved-scale and subgrid turbulent fluxes on the grid spacings is examined by computing a series of ensembles with varying grid spacings. The subgrid parameterization is shown to produce an overestimate of the PV flux at low grid resolution.

The generation of gravity waves by coastal heating gradients is explored using

linear theory calculations and idealized numerical modeling. The linear theory for flow without terrain shows that the solution depends on two parameters: a nondimensional coastal width $\mathcal{L}$ and a nondimensional wind speed $\mathcal{U}$. For $\mathcal{U} \neq 0$ the solution is composed of three distinct wave branches. Two of these branches correspond to the no-wind solution of Rotunno, except with Doppler shifting and dispersion. The third branch exists only for $\mathcal{U} \neq 0$ and is shown to be broadly similar to flow past a steady heat source or a topographic obstacle. The relative importance of this third branch is determined largely by the parameter combination $\mathcal{U}/\mathcal{L}$.

The effect of terrain is explored in the linear context using an idealized linear model and associated diagnostic computations. These results are then extended to the nonlinear problem using idealized nonlinear model runs.

To Duozhi Zhu, my Dad, my Mom and my Gram

I would like to dedicate this work to the love of my life, Duozhi Zhu, my Dad, my Mom and my Gram in China. Your love and encouragement are my source to pursue my dream and follow my heart. Thank you and love you.

ACKNOWLEDGMENTS

There are many people whom I wish to thank for their help and support. I would like to thank my co-chairs Craig C. Epifanio and Fuqing Zhang for giving me the chance to be here, supporting me and instructing me through all these years. I have learned not only a lot of knowledge in wave dynamics but also your attitude toward science. All you taught me has affected me in a good way and will affect me in my whole life. I would like to thank my committee members John W. Nielsen-Gammon and Robert Hetland for the valuable suggestions and corrections for my dissertation. I would like to thank the people who work and who have ever worked in our main office for their effort to make our life easier. I would like to thank my dear friends Caihong Wen, Zhibo Zhang, Shuguang Wang, Yonghui Weng, Wei Li, Zhiyong Meng, Larry Hopper and others for their help and encouragement. I would like to thank all my relatives and my friends in China for their encouragement and help. Finally, I would like to thank my husband, Duozhi Zhu, my Dad, my Mom and my Gram for their constant support, encouragement and love.

Thanks for the life in Texas A&M University, College Station, Texas. I think my experience here is more like a beautiful dream. It will always be a colorful memory when I think about it in the future. It will be the priceless treasure in my whole life.

TABLE OF CONTENTS

CHAPTER Page

CHAPTER Page

LIST OF TABLES

LIST OF FIGURES

FIGURE Page

FIGURE Page

FIGURE Page

FIGURE Page

FIGURE Page

CHAPTER I

INTRODUCTION

A. Introduction

Gravity waves play an important role in many aspects of atmospheric dynamics. At smaller scales, the vertical motion in gravity waves is one of the primary triggering mechanisms for atmospheric convection. Gravity waves can also feature significant shear and instability, which can sometimes lead to hazardous clear-air turbulence. Gravity waves also play a role in many larger-scale circulations through the associated transfer of momentum and energy away from heat sources and topography. This wave transport has an important influence on many regional circulations, such as the sea breeze and mesoscale convective systems. Gravity wave momentum transport away from topography in particular plays an important role in the momentum budget of the atmosphere and hence the general circulation.

The present study addresses two aspects of gravity wave dynamics. The first is the turbulent wave breakdown of large-amplitude waves over topogarphy. The second is the sea breeze wave response in flows with background wind and terrain.

B. Overview of the Topography Work

It is well known that flow past a topographic obstacle of sufficient height will produce a mountain wave that overturns and breaks ([1]; [2]; [3]; [4]). Such wave breaking can be a significant source of clear-air turbulence and can also lead to the onset of severe downslope winds at the ground ([5]; [6]). Wave breaking is also of fundamental

---

The journal model is *IEEE Transactions on Automatic Control.*

importance for the momentum balance of the atmosphere, in that the breaking ultimately provides the mechanism for wave / mean-flow interaction ([7]). With these fundamental concerns, the dynamics of breaking mountain waves has received much attention.

Most prior studies have focused on one of two aspects. Low-resolution modeling studies with parameterized turbulence have focused mainly on mesoscale wave and wave/mean-flow interaction dynamics and on the formation of mountain wakes ([8]; [9]; [10]; [11]; [12]; [13]). On the other hand, a number of very high-resolution modeling studies have focused on the detailed turbulent breakdown of the wave ([14]; [15]; [16]). Such studies have lead to improve understanding of both the wave-scale and turbulence scale phenomena in the breaking wave. However, few studies have explored the detailed interaction between these two scales.

The objective of our topography work was to provide a first step towards understanding the detailed scale interactions between the small-scale turbulent eddies and the larger-scale mean wave structure in a breaking mountain wave. Our study attempted to address this issue through considering an ensemble of 40 high-resolution wave-breaking simulations for 3D flow past a 2D ridge.

C. Overview of the Sea Breeze Work

The sea breeze circulation is an atmospheric response to the differential surface heating between the land and the sea. It impacts many atmospheric processes over coastal regions including, but not limited to, the initiation and modulation of thunderstorms, fog and air pollution. Since these atmospheric processes strongly affect the life of people who live in coastal areas, the structure of the sea breeze has been studied for a long time. Over the past two centuries since the first known published study on the

sea breeze by [17], there have been numerous studies on the subject based on different approaches: observational ([18], [19], [20], [21], [22], [23]), analytical ([24], [25], [26], [27], [28], [29]), numerical ([30], [31], [32], [33]) and laboratory ([34], [35]).

Most of the aforementioned studies focus on the local features of the sea breeze and its associated low-level front and density current. However, a few studies have noted that the sea breeze also has a mesoscale gravity wave signature ([36], [37, hereafter R83], [38], [39], [40], [41, 42]). Recently, a number of observational studies (e.g., [40] and [41, 42]) have suggested that such mesoscale coastal gravity waves may play a role in initiating convection far offshore. This costal wave hypothesis has received significant attention in recent years. However, from a theory perspective the detailed study of these waves has been limited to relatively simple cases–particularly, the no-wind and no-terrain case studied by R83 and others. The role of background wind and terrain in these flows has by comparison received relatively little attention.

The general objective of our sea breeze work is to explore the role of background wind and terrain in modifying the mesoscale sea-breeze wave response. Our approach to this problem involves both linear theory calculations and idealized numerical modeling.

D. Dissertation Outline

The following chapter describes our work on wave / turbulence scale interactions in a breaking mountain wave. The results in this chapter are taken from an article published in *J. Atmos. Sci.* (see [43], hereinafter EQ08 for details). A transition to the sea-breeze problem is made in Chapter III, which provides background material on the sea-breeze wave response. Chapter IV explores the linear theory of this wave response including the effects of a background wind. The results in Chapter IV are

taken from a manuscript in press for *J. Atmos. Sci.* (see [44], hereinafter Q08, and http://atmo.tamu.edu/people/faculty/epifanio.php for details). Chapter V explores both the role of terrain in the wave response as well as the role of nonlinear processes at large heating amplitudes. The final chapter provides a general summary and discussion.

CHAPTER II

WAVE-TURBULENCE INTERACTIONS IN A BREAKING MOUNTAIN WAVE

A. Background for Topographic Gravity Waves

Flow of the atmosphere past hills and mountains can often lead to vertically propagating gravity wave disturbances called mountain waves. Mountain waves can have an important influence on local weather and can also lead to clear-air turbulence when the waves break. The waves also exert a pressure drag on the ground and thus play an important role in the momentum balance of the atmosphere.

Early work on mountain waves relied mainly on results from linear theory (e.g., [45], [46], [47], [48], [49]). This work revealed many basic features of mountain waves – e.g., the flow decelerates on the front side of the mountain and accelerates on the lee side – and also characterized how the wave patterns aloft vary with the flow and terrain parameters. Perhaps most importantly, they showed that the mountain wave produces a pressure difference across the terrain, implying a net pressure stress on the ground. This stress is then transported vertically by the mountain-wave vertical mementum flux and is ultimately exerted at heights above the ground where the waves dissipate ([50]).

The study of nonlinear effects in mountain waves began with the analytical and laboratory studies of [51, 52] and the subseqent extensions by [1], [53] and others. These studies showed that as the height of the obstacle increases, the wave pattern steepens. At a critical height the wave overturns and breaks, leading to small-scale turbulence. This prediction has been verified by numerous laboratory studies over the years ([52], [3], [2]) and also by a growing number of observational studies documenting breaking mountain waves in nature ([54], [55], [4], [56]).

The most useful tool for investigating nonlinear effects and wave breaking in mountain waves has been numerical simulation. The first numerical calculations of breaking waves were those of [57] and [58]. These studies showed that wave overturning and turbulent mixing produces a weakly stratified and nearly stagnant layer aloft and downstream of the lee slope. Below this layer the flow is strongly accelerated, much like transcritical shallow-water flow over a hill ([59] and [60]). The early numerical work also showed that breaking leads to dissipation of the mountain wave, resulting in divergence of wave momentum flux and the local drag on the mean flow. Subsequent studies of wave breaking have explored a wide range of topics, including upstream influence (e.g., [61]), 3D effects (e.g., [62], [63]), downslope windstorms (e.g., [64], [59], [65]), PV generation ([9], [10], [66, 11]) and wave instability mechanisms (e.g. [67], [14]).

1. Wake formation

In recent years, a main focal point for the study of wave breaking has been the problem of orographic wake formation and the associated wave / mean-flow interaction dynamics. It is well understood from the linear theory that mountain waves transport disturbance momentum in the vertical (see, e.g., [68], chapter 8). In absence of dissipation this transport of momentum is uniform with height, so that the momentum flux has zero divergence at all levels ([50]). However, when wave breaking occurs the wave is dissipated, causing the momentum flux to decrease with height locally. The result is a local momentum flux convergence and an associated drag on the mean flow, often leading to the formation of a decelerated wake region downstream. Integrated globally, this wave / mean-flow interaction process and associated drag has an important impact on the global momentum budget of the atmosphere.

Most recent studies have approached the wake formation and wave / mean-flow

interaction problems from the perspective of potential vorticity (PV) generation. The turbulent fluxes of heat and momentum and associated dissipation in breaking wave cause the production of mean-flow PV in the breaking region. This PV is then advected downstream, with positive PV on the right side of the mountain (facing downstream) and negative PV on the left. As suggested by [69], [70] and [71], the dynamics of the wake and its interaction with larger scales could in principle be diagnosed from this PV distribution. Many subsequent studies of breaking waves have focused on PV production, including theoretical and numerical studies (e.g., [8], [72], [9], [10], [11], [13] and others) and a number of recent observational and real-world modeling efforts (e.g., [12]; [73]; [13]; [74]; [75]).

2. Wave breakdown study

The aforementioned and other similar studies have improved our understanding of topographic wave breaking and wake formation. However, it should be noted that the turbulent dissipation by small-scale eddies and resulting PV production in the breaking wave have not actually been resolved in these studies. Instead, parameterizations are applied to imitate these processes.

By contrast, there have also been a number of very high-resolution numerical studies to investigate the detailed turbulent breakdown of the wave. Most of these calculations have focused on wave overturning and instability near a critical level in a background shear flow. Of course the trade-off is that to date these studies have been limited to relatively small domain sizes with doubly periodic boundaries and short integration times.

The first high-resolution wave breaking study was that of [67], who focused mainly on differences between 2D and 3D breaking waves. The comparison between the 2D and 3D results indicated that the dynamic process of wave instability and

turbulent breakdown is fundamentally 3D in nature. The calculation of the eddy kinetic energy sources showed that the buoyancy source was important in the early stages of wave breakdown while shear generation was dominant in the later time. The calculation of [76] confirmed the roles of buoyancy and wind shear effects and pointed out that the interaction between the two effects led to the 3D nature of the instability. The detailed examination of this subject was then extended by [77], [14], [15], [16].

3. Chaper outline

The above two aspects of mountain wave breaking – namely, the larger-scale dynamics of wake formation and the much smaller-scale turbulent wave breakdown – are in principle very closely related. However, in practice the work on these two aspects has been seperated by considerable gaps in both scale and approach. The goal of the present work is to provide a first step toward bridging these gaps. The approach of the study is to consider an ensemble of relatively high-resolution large-eddy wave breaking calculations for the problem of 3D flow past a 2D ridge. Our interest is then to explore the interaction between the larger-scale ensemble-mean flow and the smaller-scale turbulent eddies, with a particular interest in the role of the turbulent heat and momentum fluxes in helping to shape the ensemble mean.

The following section describes the basic problem formulation, the numerical model used in the study and the ensemble design for our calculations. Section C presents the evolution of breaking wave as seen from the ensemble mean. The turbulence characteristics of the breaking wave are analyzed in detail in section D. The turbulent eddy structure, TKE budget, and the turbulent fluxes and dissipation of mean-flow wave energy are all discussed. Section E provides a detailed look at the impact of the breaking wave on the large-scale environment. The resolution depen-

dence of the eddy fluxes is considered in section F. A summary of the topography work is given in the last section.

B. Basic Physics and Computational Framework

1. Basic problem formulation

We consider a 3D, nonrotating, compressible Boussinesq flow with constant background wind, as described by

$$\frac{\partial u_i}{\partial t} + u_j \frac{\partial u_i}{\partial x_j} = -\frac{\partial P}{\partial x_i} + \delta_{i3} b - \frac{\partial T_{ij}}{\partial x_j} \tag{2.1}$$

$$\frac{\partial b}{\partial t} + u_j \frac{\partial b}{\partial x_j} + N^2 w = -\frac{\partial B_j}{\partial x_j} \tag{2.2}$$

$$\frac{\partial P}{\partial t} + u_j \frac{\partial P}{\partial x_j} + c_s^2 \frac{\partial u_j}{\partial x_j} = 0 \tag{2.3}$$

where $\mathbf{x} = (x_1, x_2, x_3) = (x, y, z)$ is the position vector; $\mathbf{u} = (u_1, u_2, u_3) = (u, v, w)$ is the velocity; P is the Boussinesq disturbance pressure and b is the buoyancy; c_s is the Boussinesq sound speed; and δ_{i3} is the Kronecker delta, which is 1 in the vertical momentum equation (i.e., $i = 3$) and 0 in the horizontal equations. The background Brunt-Väisälä frequency N is taken to be constant, implying that the Boussinesq background potential temperature variable is

$$\theta_0 = N^2 z + \text{constant} \tag{2.4}$$

The total Boussinesq potential temperature variable is then defined by $\theta = \theta_0 + b$.

The viscous stress is given by

$$T_{ij} = -\kappa \sigma_{ij}, \qquad \text{where} \tag{2.5}$$

$$\sigma_{ij} = \frac{\partial u_i}{\partial x_j} + \frac{\partial u_j}{\partial x_i} - \frac{2}{3} \delta_{ij} \nabla \cdot \mathbf{u} \tag{2.6}$$

is the deformation and κ is the kinematic viscosity. The diffusive heat flux is defined by

$$B_j = -\kappa \frac{\partial \theta}{\partial x_j}. \tag{2.7}$$

Note that the viscosity and thermal diffusivity are assumed to be equal in our study. This viscosity /diffusivity is defined as the sum of a background viscosity κ_0 and a turbulent eddy viscosity κ_e, with further discussion of κ_e given below. Free-slipe and thermal insulation conditions are applied for the stresses and heat fluxes at the lower boundary.

The shape of the 2D ridge is described by

$$h(x,y) = \begin{cases} \frac{h_0}{16}[1+\cos(\frac{\pi x}{4L})]^4, & \text{if } |x| \le 4L, \\ 0, & \text{otherwise}, \end{cases} \tag{2.8}$$

where h_0 is the height of the topography and L is roughly the half width. The lower boundary condition is then defined by

$$w = u_j \frac{\partial h}{\partial x_j} \tag{2.9}$$

at $z = h(x,y)$. In principle, the domain is unbounded in both the horizontal and positive vertical directions. Note that the flow is 3D even though the obstacle shape is 2D – that is, we consider 3D flow past a 2D obstacle.

The system is nondimensionalized by a standard nonlinear mountain-wave scaling given by

$$x = L\hat{x}, \qquad y = L\hat{y}, \qquad z = \frac{U}{N}\hat{z}, \qquad t = \frac{L}{U}\hat{t}, \qquad u = U\hat{u},$$
$$v = U\hat{v}, \qquad w = \frac{U^2}{NL}\hat{w}, \qquad b = NU\hat{b}, \qquad P = U^2\hat{P}, \qquad h = h_0\hat{h},$$

where U is the background wind and the hat indicates nondimensional quantity. With

this scaling, the property of the flow is determined by 4 nondimensional parameters: the dynamical aspect ratio $\delta = U/NL$, the Mach number $Ma = U/c_s$, Reynolds number $Re = \delta^2 UL/\kappa_0$ and the nondimensional mountain height $\epsilon = Nh_0/U$. For the problem in present study, we require

I) effectively incompressible (small Ma), nearly hydrostatic (small δ) and essentially inviscid flow (large Re),

II) the appearance of wave breaking ($\epsilon > 1$ or so),

III) negligible upstream blocking ($\epsilon < 2$ or so).

On the base of these limits, we set $\delta = 0.1$, $Ma = 0.03$, Re $= 125$ and $\epsilon = 1.6$ in all simulations.

The disturbance is initiated by implusive expansion of the lower boundary to add a mountain at time $t = 0$. The initial adjustment to this expansion is assumed incompressible, implying that the initial velocity is given by a potential flow solution for the terrain (2.8). As shown by EQ08, the initial buoyancy field produced by the expansion is given by

$$\nabla^2 b = 0 \qquad \text{with} \tag{2.10}$$

$$b = -N^2 h \qquad \text{at} \qquad z = h(x) \qquad \text{and} \tag{2.11}$$

$$b \to 0 \qquad \text{as} \qquad x^2 + z^2 \to \infty. \tag{2.12}$$

Detailed explanation can be found in E08. The initial condition for pressure is deduced on the basis of associated buoyancy and velocities.

Note that this expansion initial condition eliminates the θ gradients along the topography surface and thereby simplifies the early evolution of the flow. This early evolution is depicted in Fig. 1

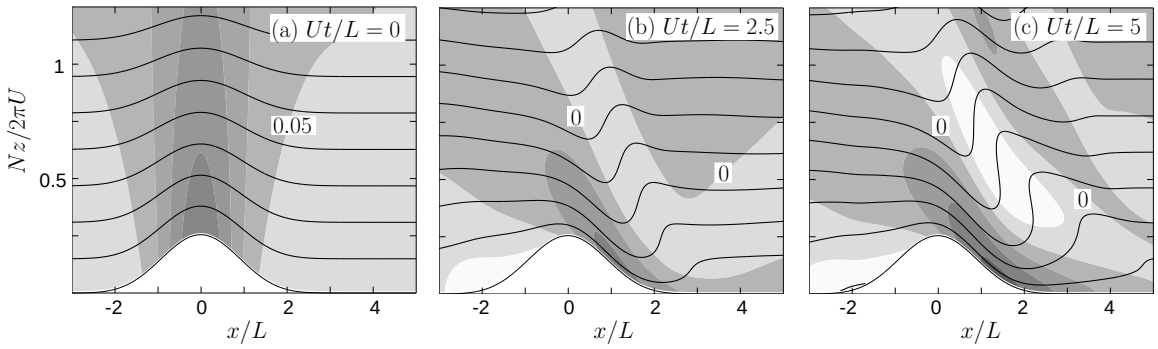

Fig. 1. Early evolution of the flow following an impulsive expansion of the obstacle. (a) Disturbance wind $(u - U)/U$ [contour interval (c.i.) $= 0.05$; light shading less than 0.05, dark shading greater than 0.05] and θ/NU [c.i. $= 1$] at time $Ut/L = 0$. (b) $(u - U)/U$ [c.i. $= 0.6$; light shading negative, dark shading positive] and θ/NU at time $Ut/L = 2.5$. (c) As in (b) but for $Ut/L = 5$.

2. Model description and simulation detail

The simulations are conducted using the three-dimensional compressible Boussinesq model described by [63]. The model uses the splitting method of [58], in which acoustic terms are integrated with a small time step to improve stability while the remaining terms are integrated with a larger time step to improve efficiency. The lateral and upper boundary conditions are realized through the damping layer. The lower boundary is free-slip and thermally insulating. Terrain is included through the use of the terrain-following vertical coordinate

$$q = \frac{z - h}{z_T - h} z_T \tag{2.13}$$

where z_T is the domain depth.

The mixing coefficient in the model follows a Smagorinsky-type formulation in which the kinematic viscosity κ is composed of the constant background viscosity κ_0 plus a variable eddy viscosity κ_e. Further discussion is given in section F. In order to eliminate high-wavenumber numerical noise and keep the model stable, the model

introduces additional filter terms to the basic equations (2.1) and (2.2). The form of the filters is $-\alpha\nabla_H^4 u_i$ and $-\alpha\nabla_H^4 b$, where α is the filter coeffient and where ∇_H^4 is a horizontal fourth-derivative operator. For convenience in the later discussion, we define the total subgrid-scale dissipation terms to be the sum of the parameterized eddy term and the filter term as

$$S_i = \frac{\partial}{\partial x_j}(\kappa_e \sigma_{ij}) - \alpha\nabla_H^4 u_i \qquad \text{and} \tag{2.14}$$

$$Q = \frac{\partial}{\partial x_j}(\kappa_e \frac{\partial \theta}{\partial x_j}) - \alpha\nabla_H^4 b, \tag{2.15}$$

where $S_i = (S_1, S_2, S_3) = (S_x, S_y, S_z)$.

Finally, the simulations are carried out in a domain with the horizontal extent being around $22L$ in the x direction and $0.54L$ in the y direction and the domain depth being $5\pi U/N$ (see the schematic in figure 2). Periodic boundary conditions are applied at the grid edges in the y direction. The choice of this set of model dimensions makes it possible for the results to include the effect from 3D turbulent eddies. The damping layers are imposed for the outer $4L$ of the domain in x and the upper half of the domain in z. The horizontal grid spacing is $\triangle x = \triangle y \approx L/56$. The vertical grid spacing is stretched with factor 1.005. The bottom grid spacing is given by $N\triangle z/U \approx 2\pi/63$. In dimensional terms, $L = 10$ km, $U = 10$ m/s, $N = 0.01s^{-1}$, $\triangle x = \triangle y = 180$m and $\triangle z \approx 100$m.

3. Ensemble averaging

We compute M ensemble members and write each member with subscript k, such as u_k, v_k, etc. Each member is seeded with a small random potential temperature perturbation, which is added to the simulation shortly before the onset of the wave breaking. In this way, the turbulent wave breakdown is made different in every run.

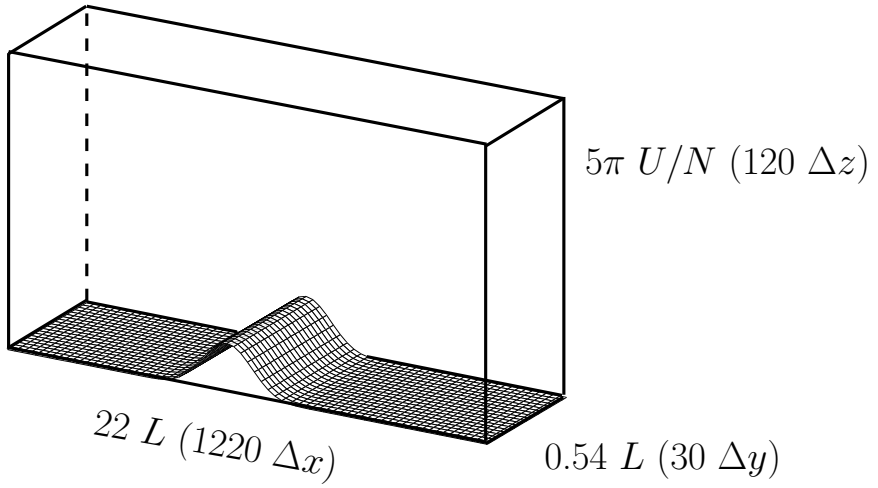

Fig. 2. Schematic illustration of the model domain for our calculations. (The along-ridge domain extent has been exaggerated for clarity.)

The definition of the mean flow is obtained by the ensemble and along-ridge average over all the members; specifically

$$\bar{u}(x,z,t) = \frac{1}{YM}\int_0^Y \sum_{k=1}^{M} u_k(x,y,z,t)dy \tag{2.16}$$

where Y is the along-ridge width of the domain. For convenience, we refer to this average simply as the *ensemble mean* in the following. Then the total field can be written as

$$u(x,y,z,t) = \bar{u}(x,z,t) + u'(x,y,z,t),$$

where $u'(x,y,z,t)$ is the disturbance flow.

As an approximation we assume the mean flow to be imcompressible. Applying the above average to the nonrotating Boussinesq equations (2.1), (2.2) and (2.3) then

leads to

$$\frac{\partial \bar{u}}{\partial t} + \bar{u}\frac{\partial \bar{u}}{\partial x} + \bar{w}\frac{\partial \bar{u}}{\partial z} = -\frac{\partial \bar{P}}{\partial x} + \kappa_0 \nabla^2 \bar{u} + \bar{F}_x + \bar{S}_x, \tag{2.17}$$

$$\frac{\partial \bar{w}}{\partial t} + \bar{u}\frac{\partial \bar{w}}{\partial x} + \bar{w}\frac{\partial \bar{w}}{\partial z} = -\frac{\partial \bar{P}}{\partial z} + \bar{b} + \kappa_0 \nabla^2 \bar{w} + \bar{F}_z + \bar{S}_z, \tag{2.18}$$

$$\frac{\partial \bar{b}}{\partial t} + \bar{u}\frac{\partial \bar{b}}{\partial x} + \bar{w}\frac{\partial \bar{b}}{\partial z} + N^2 \bar{w} = \kappa_0 \nabla^2 \bar{b} + \bar{H} + \bar{Q}, \tag{2.19}$$

$$\frac{\partial \bar{u}}{\partial x} + \frac{\partial \bar{w}}{\partial x} = 0 \tag{2.20}$$

where

$$\bar{F}_x = -\frac{\partial \overline{u'u'}}{\partial x} - \frac{\partial \overline{u'w'}}{\partial z}, \tag{2.21}$$

$$\bar{F}_z = -\frac{\partial \overline{w'u'}}{\partial x} - \frac{\partial \overline{w'w'}}{\partial z}, \tag{2.22}$$

$$\bar{H} = -\frac{\partial \overline{b'u'}}{\partial x} - \frac{\partial \overline{b'w'}}{\partial z}. \tag{2.23}$$

Here the primes indicate turbulent quantities on the resolved scale so that $\bar{F}_x$, $\bar{F}_z$ and $\bar{H}$ are the resolved-scale eddy forcings. $\bar{S}_x$, $\bar{S}_z$, and $\bar{Q}$ are the mean parameterized forces including the effects of filters as defined by (2.14) and (2.15). As discussed by EQ08, for our high-resolution calculations the $\bar{S}_x$, $\bar{S}_z$ and $\bar{Q}$ terms are relatively small.

4. Instantaneous and averaging field

Because of computational contraints, our ensemble size was limited to 40 members. To check the degree to which the averaging result with $M = 40$ approximates the true mean (i.e., $M \to \infty$), we consider two criteria: (i) we compare the instantaneous unaveraged computations and the ensemble-mean results so as to tell if the turbulence is mostly smoothed out; and (ii) we check that the ensemble-mean result is almost unchangable with M when the ensemble size reaches some number. We evaluate that

these criteria from three perspectives: the mean flow, the resolved-scale turbulent eddy and the area-average of eddy forcings.

Fig. 3(a) shows the instantaneous horizontal velocity u and the isentropes θ as taken from one ensemble member at a fixed y. It is obvious that the flow is turbulent over the lee slope. With 10 ensemble members [Fig. 3(b)], the ensemble-mean result removes most of the turbulent fluctuations and the mean flow pattern is obviously recognizable. However, some fluctuations can still be seen over some of the more turbulent regions in the downstream areas. Figs. 3(c) and 3(d) show that for the mean flow, the mean results for 20 members is very close to the mean result for 40 members.

Fig. 4 shows that the turbulent eddy force $\bar{F}_x$ is more difficult to compute. As expected, the distribution of the force term for $M = 1$ and $M = 10$ is relatively noisy. When $M = 40$, the pattern of postive and negative $\bar{F}_x$ becomes easily apparent; however, there are still some local peaks. To produce smoother results, an additional time average is applied to the ensemble mean. In particular, our model data contains a high time-resolution output sequence from $Ut/L = 17$ to $Ut/L = 18$ with output interval of $U\triangle t/L = 0.1$. Fig. 4(d) shows that averaging $\bar{F}_x$ over $17 \leq Ut/L \leq 18$ smooths the results and produces a more reliable estimation.

Finally, figure 5 shows that computing the area average of the turbulent flux terms is easier than computing the terms directly. Shown in Fig. 5 is the area-averaged mean flow PV flux defined by

$$\langle J_y^{PV} \rangle = \frac{1}{A} \int_A (\bar{F}_x \frac{\partial \bar{\theta}}{\partial z} - \bar{F}_z \frac{\partial \bar{\theta}}{\partial x} - \bar{H}\bar{\eta}) dA \tag{2.24}$$

where $\bar{\eta} = \partial \bar{u}/\partial z - \partial \bar{w}/\partial x$ is the mean plane-normal vorticity. The integral area A is the effective x - z domain of the simulation not including the damping layers. As shown in figure 5 for small M the averaged PV flux varies rapidly with M. But then

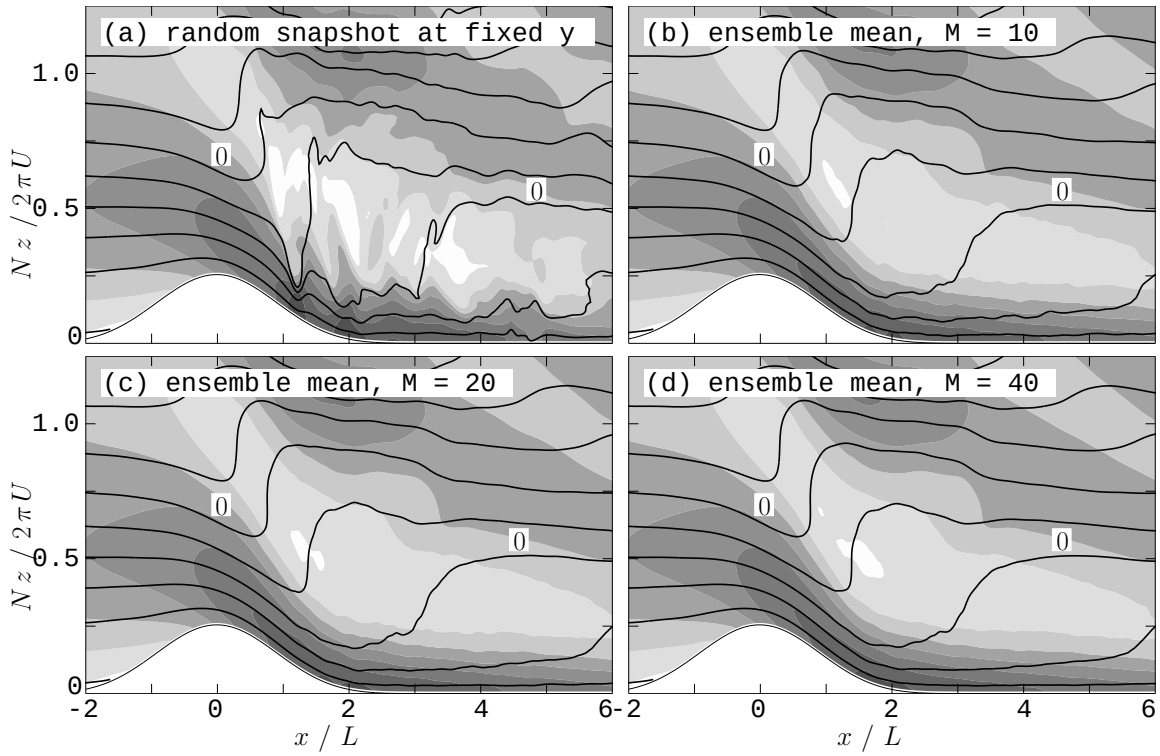

Fig. 3. Averaging out the turbulence in our ensemble calculations. (a) Random snapshot of the flow at fixed y from one ensemble member. Shown are $(u-U)/U$ [c.i. $= 0.5$; darker shading positive, lighter shading negative] and θ/NU [c.i. $= 1$] at time $Ut/L = 12.5$. (b),(c) The corresponding ensemble-mean fields $(\bar{u}-U)/U$ [same c.i. and shading] and $\bar{\theta}/NU$ for the cases (b) $M = 10$, (c) $M = 20$ and (d) $M = 40$.

as M approaches 40 the averaged flux appears to roughly converge, suggesting that $M = 40$ provides a reliable approximation.

C. Mean Fields

The present section descibes the ensemble-mean structure of the flow. The mean isentropes and cross-mountain wind at time $Ut/L = 6.25$, 17.5 and 35 are displayed in Fig. 6. The time $Ut/L = 6.25$ is the first output time at which the wave is just beginning to break. The isentropes at this time have begun to overturn above the lee

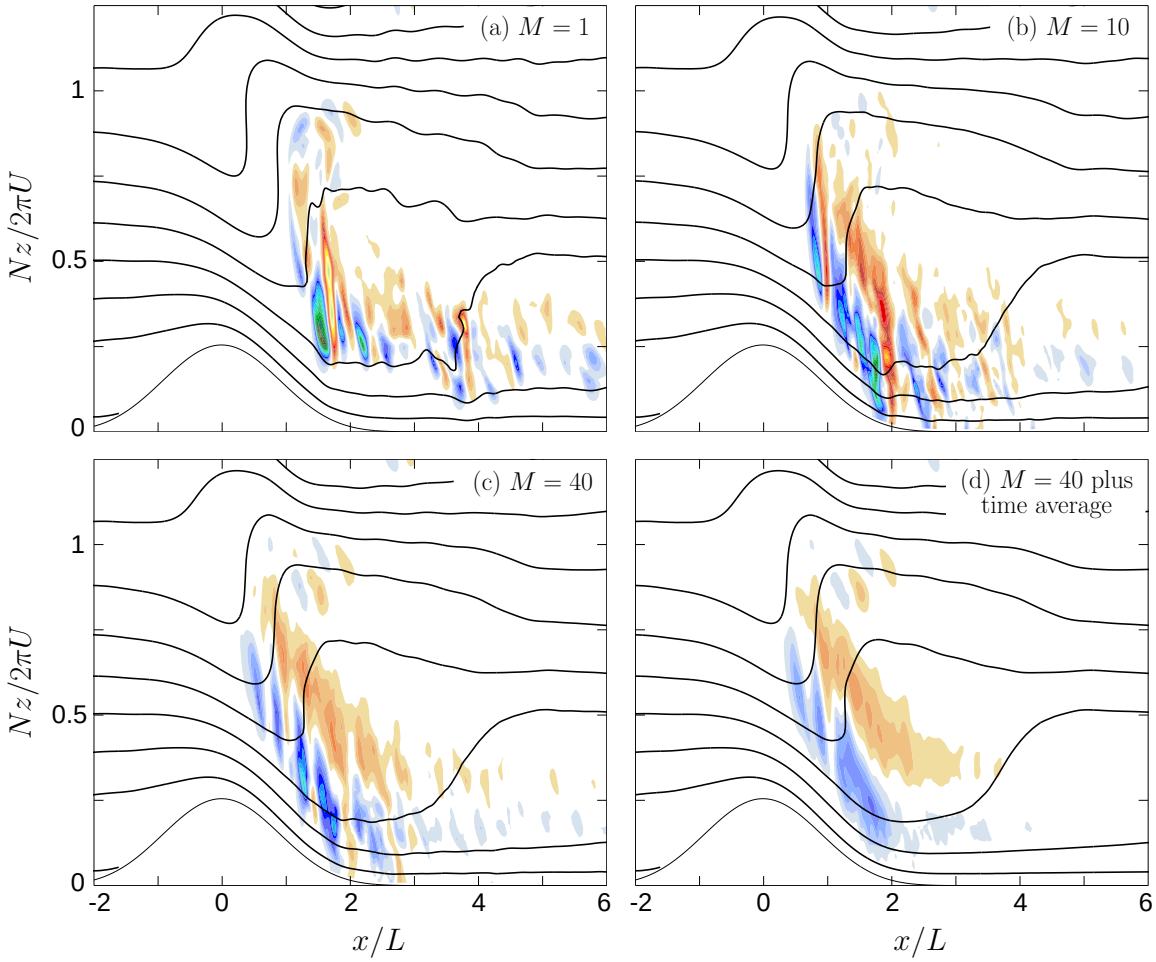

Fig. 4. Computing the eddy-flux forcings. Black lines show $\bar{\theta}/NU$ [c.i. = 1] and color contours show $L\bar{F}_x/U^2$ at time $Ut/L = 17.5$ for (a) $M = 1$ [c.i. = 0.15], (b) $M = 10$ [c.i. = 0.12] and (c) $M = 40$ [c.i. = 0.1]. Red colors indicate values greater than the contour interval, blue colors show less than minus the contour interval. (d) as in (c) but averaged over the time interval $17 \leq Ut/L \leq 18$.

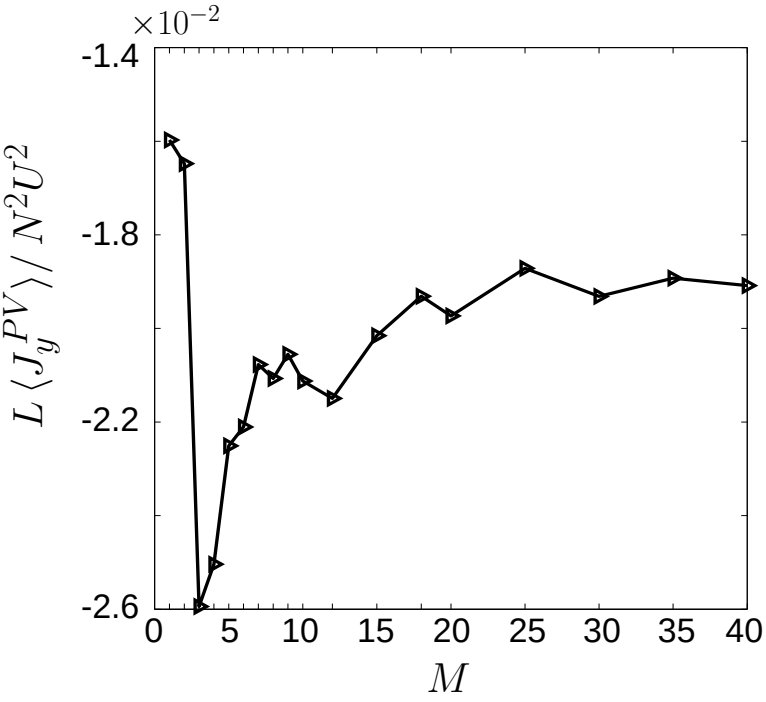

Fig. 5. Area-averaged mean-flow PV flux $L\,\langle J_y^{PV}\rangle\,/\,N^2U^2$ [see (2.24)] as a function of the ensemble size M at time $Ut/L = 17.5$.

slope of the mountain and wind reversal region is apparent over a significant portion of the wave. A small but non-zero value of TKE (as computed in section D2) suggests that the wave at this time has begun to break.

At time $Ut/L = 17.5$, the structure of the mean-flow is changed significantly by the breaking mountain wave. A well-mixed region is formed over lee slope (Fig. 6b) and this region spreads downstream with time (Fig. 6c). At time $Ut/L = 35$, the flow fields almost reached steady state. The flow in the well-mixed region is almost stagnant while the flow above and below this region is strongly accelerated. Trapped steady waves are clearly seen above the well-mixed region at this time.

For nearly incompressible flow, the plane-normal vorticity $\bar{\eta}$ completely determines the mean velocity distribution. Figure 7 shows the mean vorticity $\overline{\eta}$ and the velocity vectors at the last output time. It is apparent that the stagnant wake region

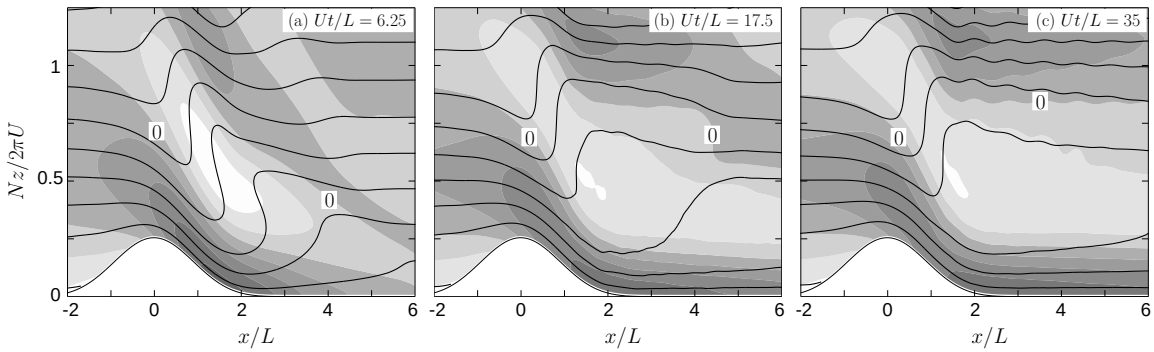

Fig. 6. Ensemble-mean potential temperature $\bar{\theta}/NU$ [c.i. = 1] and cross-ridge wind component $(\bar{u} - U)/U$ [c.i. = 0.5; darker shading positive, lighter shading negative] at times $Ut/L =$ (a) 6.25, (b) 17.5 and (c) 35.

extends downstream. Above the stagnant region the vorticity is positive into the page and below this layer the vorticity is negative. The superposition of the two vorticity anomalies implies the stagnant wake layer.

D. Turbulence Characteristics

The turbulent characteristics of the flow are described in the present section. Section D1 gives an example to document a typical turbulent eddy structure in the flow. Section D2 discusses the TKE budget as a function of time. The turbulent fluxes and dissipation of mean-flow wave energy are calculated in section Section D3.

1. Turbulent eddy structure

Figure 8 shows the plane-normal vorticity and the isentropes from one chosen ensemble member at a fixed value of y at time $Ut/L = 17.0$, 17.2, 17.4, 17.6 and 17.8. The overlaid thick black solid line is the time-averaged mean-flow Richardson number; that is, $Ri = \partial\bar{\theta}/\partial z/def^2$ where $def^2 = \bar{\sigma}_{ij}\bar{\sigma}_{ij}/2$ is the mean-flow deformation. The time average of Ri is taken over the interval from $Ut/L = 17$ to 18 as described in

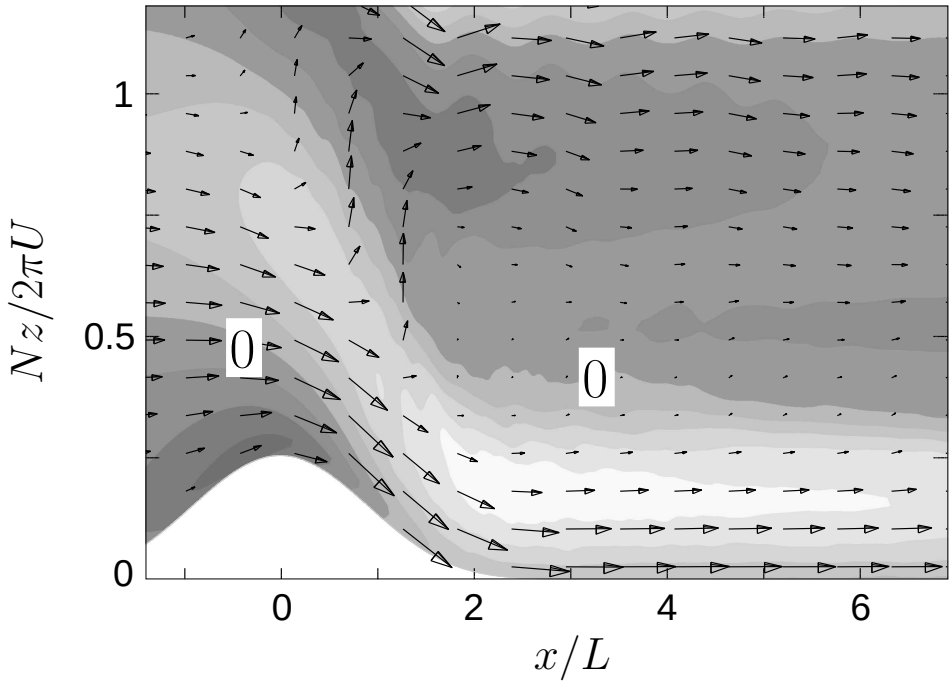

Fig. 7. Mean plane-normal vorticity component $\bar{\eta}/N$ [c.i. = 0.4; darker shading positive, lighter shading negative] and mean velocity vectors $(\bar{u}, \bar{w})/U$ at time $Ut/L = 35$.

section B4. Only the $Ri = 0.25$ contour is shown.

Figure 8 shows that the flow becomes turbulent only downstream of the first point where $Ri = 0.25$. Upstream of this point the flow is laminar. The turbulence appears as a series of eddies that initiate at the front of the low-Ri region and then move downstream. As an example one obviously large turbulent eddy is observed at point $x/L = 2$, $Nz/2\pi U = 0.25$ at time $Ut/L = 17$. With increasing time, eddy is advected downstream and a new eddy appears upstream. Note that the example in Fig. 8 is the cleanest case of eddy evolution observed from all 40 ensemble members. In most cases the eddies are less coherent. We thus move to averaged measures of the turbulence in the following sections.

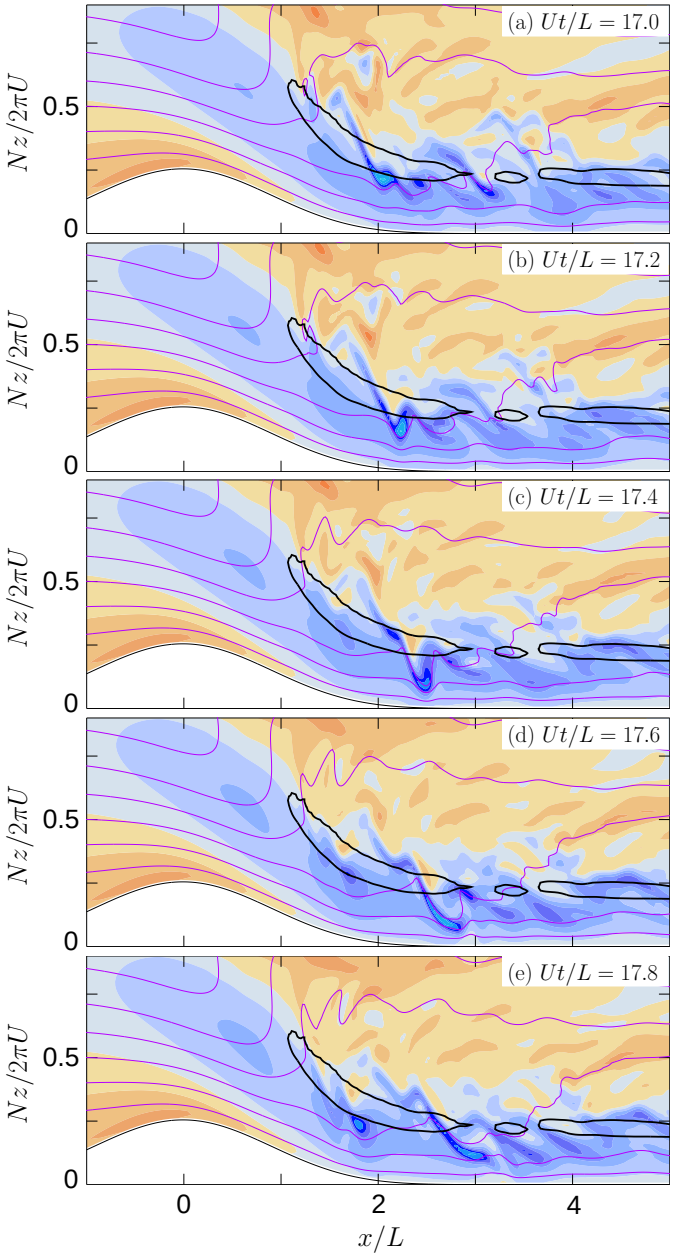

Fig. 8. Snapshots of vorticity η/N [color shading; c.i. = 0.6, red shading positive and blue shading negative] and potential temperature θ/NU [violet contour; c.i. = 1] taken from one ensemble member at a fixed value of y. Shown are times $Ut/L =$ (a) 17, (b) 17.2, (c) 17.4, (d) 17.6 and (e) 17.8. Black lines show the $Ri = 0.25$ contour, where Ri is the Richardson number for the ensemble-mean flow as averaged over $17 \leq Ut/L \leq 18$.

2. TKE budget

The resolved-scale TKE of the breaking wave is given by $\bar{\epsilon} = \overline{u_i' u_i'}/2$, where again the prime indicates the deviation from the ensemble mean. Substracting (2.17)-(2.18) from (2.1) and multiplying the ith turbulent moumentum equation by u_i', the TKE equation can be obtained as

$$\frac{\overline{D}\overline{\epsilon}}{Dt} = -\overline{u_i' \frac{\partial P'}{\partial x_i}} - \overline{u_i' u_j' \frac{\partial u_i'}{\partial x_j}} - \overline{u_i' u_j'} \frac{\partial \overline{u_i}}{\partial x_j} + \overline{b' w'} + \overline{u_i' (D_i - \overline{D}_i)}, \tag{2.25}$$

where

$$\frac{\bar{D}}{Dt} = \frac{\partial}{\partial t} + \bar{u}\frac{\partial}{\partial x} + \bar{w}\frac{\partial}{\partial z}$$

and

$$D_i = \frac{\partial}{\partial x_j}(\kappa_0 \sigma_{ij}) + S_i$$

is the sum of the background viscous, parameterized eddy, and filter dissipation terms. For the equation (2.25), the terms on the right are: the pressure-gradient work term, the turbulent transport term, the shear generation term, the buoyancy generation term and the TKE dissipation term.

Figure 9a displays the time evolution of the TKE. At $Ut/L = 6.25$ the isentropes are overturned and the wave starting to break. Time $Ut/L = 7.5$ is the first output time following the onset of the breaking wave (Fig. 9b). The TKE at this time is maximized near the ground with the largest TKE value exceeding $0.47U^2$ (or root-mean-square u_i' of nearly $\pm U$). By $Ut/L = 8.75$ the burst of TKE near the ground is dissipated and the maximum TKE region is located above the lee side of the mountain (as shown in Fig. 9c). With increasing time, the amplitude of TKE decreases (as in Figs. 9d-f).

Figure 10a shows the evolution of the area-averaged TKE as well as the dominant forcing terms in TKE equation. As should be expected, a rapid burst of TKE appears

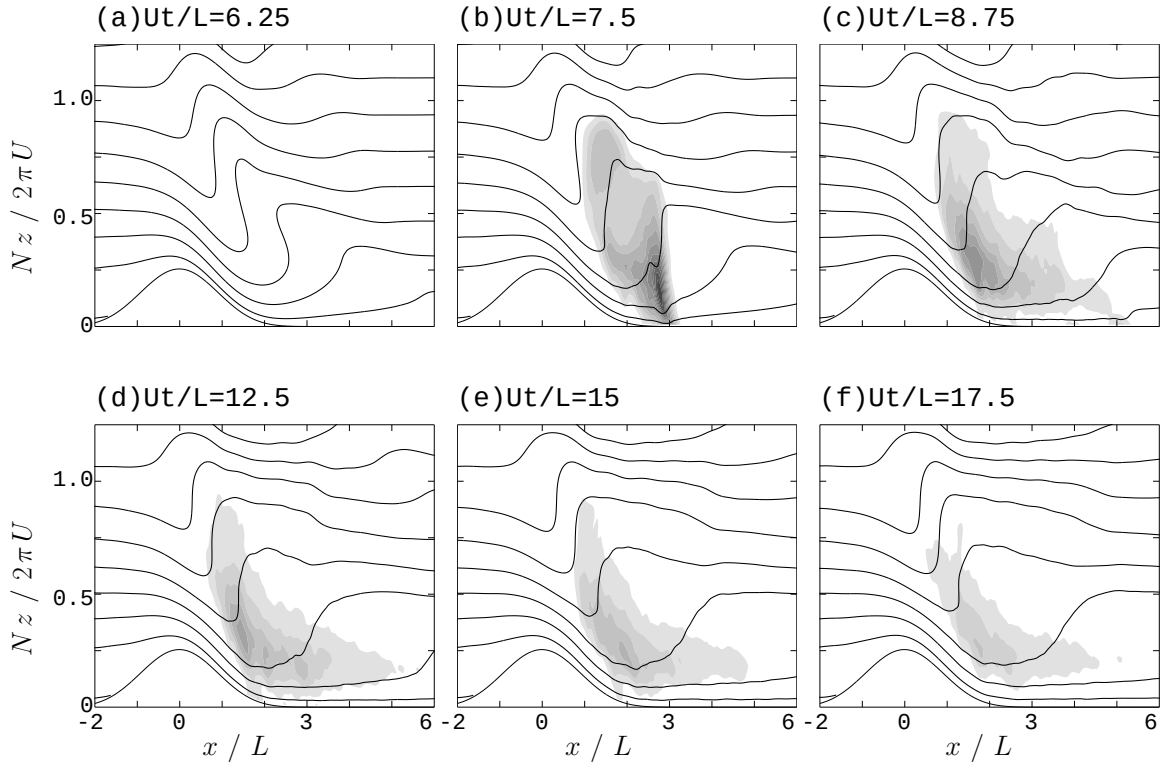

Fig. 9. Resolved-scale turbulent kinetic energy $\bar{\epsilon}/U^2$ [shaded; c.i. = 0.04 with values greater than 0.04 shown] and ensemble-mean isentropes $\bar{\theta}/NU$ [c.i. = 1] at time Ut/L = (a) 6.25, (b) 7.5, (c) 8.75, (d) 12.5, (e) 15, and (f)17.5.

at the output time $Ut/L = 7.5$. The mean TKE then increases slightly until it reaches a maximum at the output time $Ut/L = 10$. At later times the TKE steadily decreases until reaching a relatively constant value after $Ut/L = 20$. The three dominant forcing terms in the TKE equation are the shear generation term, the dissipation term and the buoyancy term. Among them, the shear generation term is essentially balanced by the dissipation term. The buoyancy term is only noticeable during the burst of TKE and is negative for the output times shown.

Figures 10b,c indicate the spatial distribution of the two largest terms –shear generation term and dissipation term – in the TKE equation at time $Ut/L = 12.5$. Consistent with Figs. 8 and 9, both of them appear along the upper edge of lee-slope

shooting flow. The shear generation term has the larger amplitude but the dissipation term is greater in spatial extent.

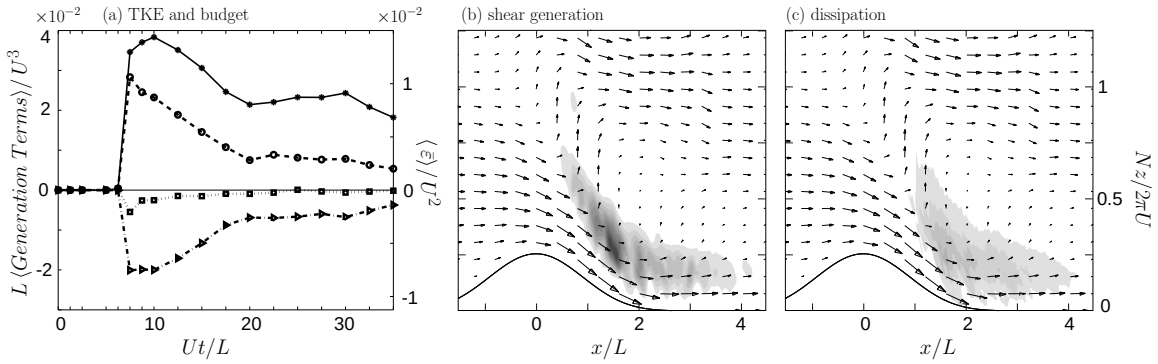

Fig. 10. Resolved-scale TKE and generation terms. (a) Area-averaged TKE $\langle\bar{\epsilon}\rangle/U^2$ [solid line; uses right axis label] and associated area-averaged budget terms [scaled by U^3/L; left axis label] as functions of Ut/L. The budget terms include shear generation [dashed-circle], buoyant generation [dotted-square], and dissipation [dash-dotted-triangle]. Axis labels in (a) [both left and right] include factors of 10^{-2}. (b) The shear generation [scaled by U^3/L; shaded c.i. = 0.1] and (c) dissipation [scaled by U^3/L; shaded c.i. = 0.1] terms at time $Ut/L = 12.5$.

3. The turbulent fluxes

The effect of the turbulent eddies on the mean flow is described by the eddy-flux convergence terms defined by (2.21-2.23). Figures 11a,b,c display the distribution of these terms as derived from the high-resolution ensemble. The results in the figure are averaged over $17 \leq Ut/L \leq 18$ as described in section B4.

The horizontal flux convergence $\bar{F}_x$ is illustrated in Fig. 11a. The distribution of $\bar{F}_x$ is centered roughly on the region of the large TKE in Fig. 9. The sense of $\bar{F}_x$ is to deccelerate the shooting flow over the lee slope and accelerate the nearly stagnant flow in the wake. A closer look into the contribution of two parts of $\bar{F}_x$ shows that

$-\partial\overline{u'u'}/\partial x$ and $-\partial\overline{u'w'}/\partial z$ contribute roughly the same amount. The contribution from the horizontal flux $\overline{u'u'}$ is thus not small, as is sometimes assumed in turbulence parameterizations. In terms of magnitude, $\bar{F}_x$ is in the same order as (but smaller than) the pressure gradient $-\partial\overline{P}/\partial x$.

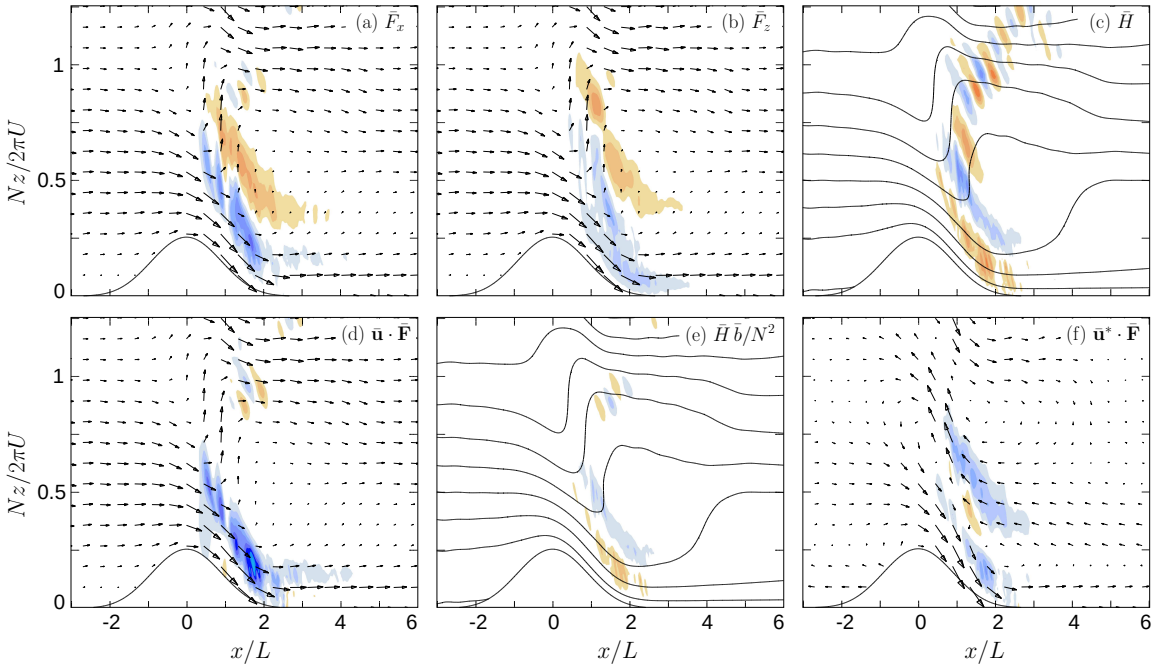

Fig. 11. Resolved-scale eddy forcing, Bernoulli reduction and wave dissipation terms as averaged over $17 \leq Ut/L \leq 18$. Eddy forcings are (a) $L\bar{F}_x/U^2$ [c.i. $= 0.1$], (b) $L\bar{F}_z/\delta U^2$ [c.i. $= 1$] and (c) $L\bar{H}/NU^2$ [c.i. $= 0.05$]. The associated Bernoulli terms are (d) $L\left(\bar{\mathbf{u}}\cdot\bar{\mathbf{F}}\right)/U^3$ [c.i. $= 0.1$] and (e) $L\left(\bar{H}\bar{b}/N^2\right)/U^3$ [c.i. $= 0.1$]. (f) Frictional wave energy dissipation rate $L\left(\bar{\mathbf{u}}^*\cdot\bar{\mathbf{F}}\right)/U^3$ [c.i. $= 0.1$] where $\bar{\mathbf{u}}^* = (\bar{u}-U, \bar{w})$ is the mean disturbance wind. Color shading is as described in Fig. 4. Vectors in (a), (b) and (d) show the mean velocity $\bar{\mathbf{u}}/U$ and vectors in (f) show $\bar{\mathbf{u}}^*/U$. Solid lines show $\bar{\theta}/NU$ [c.i. $= 1$].

Fig. 11b shows that the vertical momentum flux convergence term $\bar{F}_z$ is also mostly located in the area of large TKE. Negative $\bar{F}_z$ is seen along the downstream shooting flow above the lee slope and positive $\bar{F}_z$ is found along the upward branch

of the wave. The net effect of $\bar{F}_z$ is thus to enhance the bifurcation of the mean flow around the stagnant wake region.

In contrast to $\bar{F}_x$ and $\bar{F}_z$, the pattern for $\bar{H}$ shows three main anomalies – two positive and one negative. (The smaller-scale $\bar{H}$ pattern above $Nz/2\pi U \approx 0.75$ is apparently associated with trapped gravity waves rather than turbulent fluxes.) Below $Nz/2\pi U \approx 0.5$ both $\overline{b'u'}$ and $\overline{b'w'}$ terms in (2.23) contribute to $\bar{H}$ and the net effect is to transfer heat downward. For the anomaly above $Nz/2\pi U \approx 0.5$ the $\overline{b'w'}$ is dominant and the net heat flux is upward. The upward heat flux occurs roughly where the isentropes in many of the ensemble members are overturned (compare to Fig. 8), leading to upward fluxes of heat. However, note that the heating pattern tends to counteract the overturning of isentropes in the mean flow.

The net effect of the eddies on the mean flow is indicated by the mean Bernoulli function. For the moment we just focus on the resolved-scale eddy contributions and neglect the background viscous, parameterized eddy and numerical filter terms (all of which are small) in equations (2.17)-(2.19). Then the equations reduce to

$$\frac{\partial \bar{u}}{\partial t} + \bar{u}\frac{\partial \bar{u}}{\partial x} + \bar{w}\frac{\partial \bar{u}}{\partial z} = -\frac{\partial \bar{P}}{\partial x} + \bar{F}_x, \tag{2.26}$$

$$\frac{\partial \bar{w}}{\partial t} + \bar{u}\frac{\partial \bar{w}}{\partial x} + \bar{w}\frac{\partial \bar{w}}{\partial z} = -\frac{\partial \bar{P}}{\partial z} + \bar{b} + \bar{F}_z, \tag{2.27}$$

$$\frac{\partial \bar{b}}{\partial t} + \bar{u}\frac{\partial \bar{b}}{\partial x} + \bar{w}\frac{\partial \bar{b}}{\partial z} + N^2\bar{w} = \bar{H}. \tag{2.28}$$

Taking $\bar{u}\times(2.26) + \bar{w}\times(2.27) + \bar{b}/N^2\times(2.28)$ gives us

$$\frac{\overline{D}R}{Dt} = \frac{\partial \bar{P}}{\partial t} + \overline{\mathbf{u}} \cdot \overline{\mathbf{F}} + \frac{\bar{H}\bar{b}}{N^2} \tag{2.29}$$

where $\overline{\mathbf{u}} = (\bar{u}, 0, \bar{w})$, $\overline{\mathbf{F}} = (\bar{F}_x, 0, \bar{F}_z)$ and where the mean-flow Bernoulli function is defined by

$$R = \frac{\overline{\mathbf{u}} \cdot \overline{\mathbf{u}}}{2} + \bar{P} + \frac{\bar{b}^2}{2N^2}. \tag{2.30}$$

The distribution of Bernoulli function shows that R tends to have reduced values in the wake (not shown), suggesting the presence of dissipation in the breaking region. Fig. 11d,e show the two dissipative terms in (2.29): the frictional term $\bar{\mathbf{u}} \cdot \bar{\mathbf{F}}$ and the diabatic term $\bar{H}\bar{b}/N^2$. The main dissipation source is clearly the frictional term. This suggests that the main role of the eddies is the work done by $\bar{\mathbf{F}}$ in decelerating the lee-side shooting flow (compare Fig. 11a and 11d). The diabatic term acts counter to the frctional term in the shooting flow but is much smaller and has a limited effect.

Suppose we define the mean-flow wave energy E to be the total energy as seen in the intrinsic frame (i.e., the frame in which the background wind is zero). Letting $\bar{\mathbf{u}}^* = \bar{\mathbf{u}} - (U, 0, 0)$, the wave energy E is then given by

$$E = \frac{\bar{\mathbf{u}^*} \cdot \bar{\mathbf{u}}^*}{2} + \frac{\bar{b}^2}{2N^2}.$$

and the budget for E derived from (2.28)-(2.30) and (2.20) is

$$\frac{\overline{D}E}{Dt} = -\nabla \cdot (\bar{P}\bar{\mathbf{u}}^*) + \bar{\mathbf{u}}^* \cdot \bar{\mathbf{F}} + \frac{\bar{H}\bar{b}}{N^2}. \tag{2.31}$$

In the area mean, only terms $\bar{\mathbf{u}}^* \cdot \bar{\mathbf{F}}$ and $\bar{H}\bar{b}/N^2$ in in (2.31) describe the disspative sources and sinks. Figures 11e, f show that the dissipation of wave energy mainly depends on the turbulent momentum fluxes and the work done by these fluxes counter to $\bar{\mathbf{u}}^*$.

E. Wave-mean Interaction Process

As discussed in section A1, a main effect of the turbulent eddies is to dissipate the mountain wave. This dissipation leads to an interaction of the wave with the larger-scale environment. In this section, the wave-mean interaction process will be investigated from two aspects: the vertical transfer of momentum by the wave and the

cross-stream flux of mean-flow PV. Note that we will again neglect the background viscous, parameterized eddy and numerical filter terms in this section so that the emphasis is put on resolved-scale eddy fluxes. A more detailed analysis of the wave-mean problem can be found in EQ08.

1. Momentum forcing

The equation (2.26) can be written by

$$\frac{\partial \bar{u}}{\partial t} = -\frac{\partial(\bar{P} + \bar{u}\bar{u})}{\partial x} - \frac{\partial \bar{u}\bar{w}}{\partial z} + \bar{F}_x \tag{2.32}$$

If we assume that the disturbance vanishes as $x \to \pm a$ as long as a is sufficiently large, then a horizontal average of (2.32) gives

$$\frac{\partial \langle \bar{u} \rangle}{\partial t} = -\frac{\partial \langle \bar{u}\bar{w} \rangle}{\partial z} + \langle \bar{F}_x \rangle \tag{2.33}$$

where the bracket indicates the horizontal average.

Fig. 12a shows $\langle \bar{u}\bar{w} \rangle$ as a function of z at 3 different times, suggesting dissipation of the wave in the breaking region. Fig. 12b displays the two forcing terms on the right in (2.33) as well as the sum of these two terms. The averaged momentum forcing is dominated by the wave-scale momentum flux rather than the small-scale turbulent fluctuations, i.e., the effect of the eddy fluxes is indirect. The role of the eddies is to dissipate the mountain wave so as to produce a momentum-flux convergence at the wave scale.

2. PV fluxes

With the Boussinesq approximation, the potential vorticity (PV) for the ensemble-mean flow is defined by

$$q = \overline{\boldsymbol{\zeta}} \cdot \nabla \overline{\theta} \tag{2.34}$$

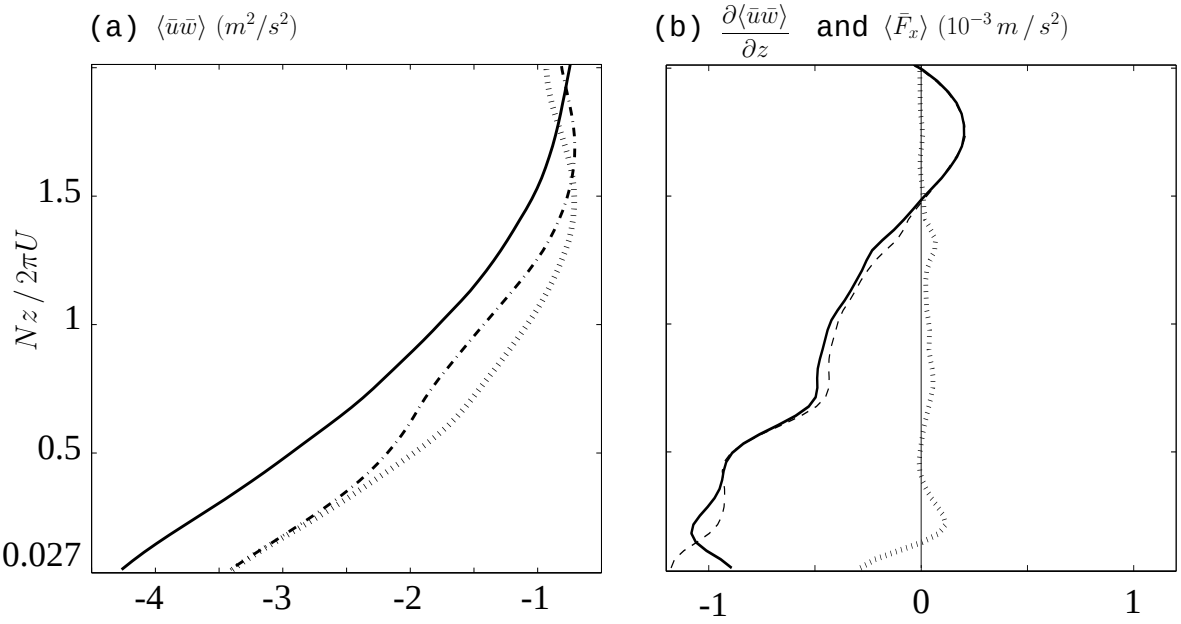

Fig. 12. (a) Horizontal average of $\langle \bar{u}\bar{w} \rangle$ as a function of z at $Ut/L = 8.75$ (solid), 17.5 (dashdot), 35 (dotted). (b) Horizontal average of $-\frac{\partial \langle \bar{u}\bar{w} \rangle}{\partial z}$ (solid), $\langle \bar{F}_x \rangle$ (dotted) and sum of them (dash) at time $Ut/L = 35$.

where $\overline{\boldsymbol{\zeta}} = \nabla \times \overline{\mathbf{u}}$. The conservation relation for the PV can be written in the form

$$\frac{\partial q}{\partial t} + \nabla \cdot \mathbf{J} = 0 \tag{2.35}$$

where $\mathbf{J}$ is the PV flux as obtained by [69] as

$$\mathbf{J}^{PV} = \bar{\mathbf{u}} q + \nabla \bar{\theta} \times \bar{\mathbf{F}} - \bar{\boldsymbol{\zeta}} \bar{H}. \tag{2.36}$$

The first term on the right side is the advection of PV, and the last two terms are dissipative flux terms which consist of the frictional PV flux and the diabatic PV flux.

In our 2D ensemble-mean study, the PV for the ensemble-mean flow is zero everywhere. However, the dissipative cross-stream PV flux exists with non-zero value (effectively transferring PV between $y = -\infty$ and $y = \infty$). This dissipative PV flux

component is given from (2.36) by

$$J_y^{PV} = \bar{F}_x \frac{\partial \bar{\theta}}{\partial z} - \bar{F}_z \frac{\partial \bar{\theta}}{\partial x} - \bar{\eta}\bar{H} \tag{2.37}$$

where $\bar{\eta}$ is again the plane-normal component of vorticity.

Figure 13 shows the cross-stream PV flux as well as the frictional and the diabatic parts of the flux. The net PV flux (Fig. 13a) is concentrated within the shear zone between the wake and the shooting flow. The dominant contribution to the flux is from the frictional term (Fig. 13b). The diabatic part (Fig. 13c) is small by comparison and has the opposite sense along the shooting flow.

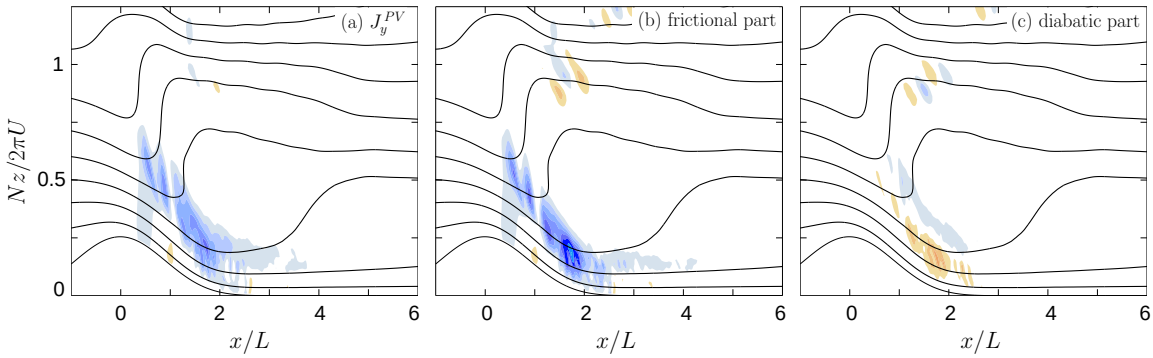

Fig. 13. (a) The dissipative cross-stream PV flux $L\,J_y^{PV}/\,N^2U^2$ [see (2.37)] as averaged over times $17 \leq Ut/L \leq 18$ [c.i. $= 0.1$; red colors positive, blue negative; color shading as in Fig. 4]. (b) The frictional and (c) the diabatic parts of the flux. Solid lines in each panel show $\bar{\theta}/NU$ [c.i. $= 1$].

F. Resolution Dependence

The change in the resolved-scale and parameterized eddy fluxes as a function of grid spacing is documented in this section. Ensemble results are presented for horizontal grid spacings ranging from $L/56$ to $L/3.7$. We will see that the forcing terms in (2.17)-

(2.19) are dominated by the resolved-scale forcings for the high-resolution results, while they are dominated by the parameterized terms for the low resolution.

1. The subgrid model

For the subgrid parameterization, we apply a standard Smagorinsky-Lilly formulation in all calculations. The eddy viscosity in the subgrid model is defined by

$$\kappa_m = \begin{cases} (c_m l)^2 \sigma \left(1 - \frac{\mathcal{R}}{\mathcal{R}_c}\right)^{1/2} & \text{for } \mathcal{R} < \mathcal{R}_c, \\ 0, & \text{otherwise,} \end{cases} \tag{2.38}$$

and

$$\kappa_h = \kappa_m / \mathcal{P} \tag{2.39}$$

where κ_m is the kinematic eddy viscosity, κ_h is the thermal diffusivity, $\mathcal{R}$ is the resolved-scale Richardson number and $\sigma = \sqrt{\sigma_{ij}\,\sigma_{ij}/\,2}$ is the resolved-scale deformation as defined by (2.6). The free parameters for the parameterization include the mixing constant c_m, the mixing length l, the cutoff Richardson number $\mathcal{R}_c$, and the Prandtl number $\mathcal{P}$.

For the stratified problem, the choice of the parameters in the subgrid model does not yet rely on a solid foundation ([78]). However, experience with LES shows that the simulations are not sensitive as long as these parameters are chosen within a reasonable range (e.g., [78] and [79]). In our calculations, the mixing coefficient is $c_m = 0.21$, the mixing length is $l = \sqrt{\Delta x \Delta z}$, the cutoff Richardson number is $\mathcal{R}_c = 0.5$, and the Prandtl number is $\mathcal{P} = 1$ so that $\kappa_m = \kappa_h = \kappa_e$. This set of parameter values is representative of those used in many research and weather prediction models.

Our simulations also include a fourth-order filter, as described in section B2. The

Table I. Grid spacings for the resolution experiments

Ensemble	1	2	3	4	5	6	7	8
Grid increment	Δ	2Δ	3Δ	3.75Δ	5Δ	6Δ	10Δ	15Δ
Number of points per L	55.5	27.8	18.5	14.8	11.1	9.3	5.6	3.7

filter coefficient $\alpha = 0.2\,(\Delta x)^4/\,32\Delta t$.

2. Experimental setup

Our experiments are based on eight sets of ensemble calculations with different resolutions. The horizontal grid spacings are shown in table I. The vertical grid spacing for the different resolution experiments are roughly same. As in the highest resolution case, the ensemble size for each calculation is $M = 40$.

The background viscous, resolved-scale eddy, parameterized eddy, and horizontal filter terms in (2.17)-(2.19) are computed for each ensemble. For convenience, we denote the net dissipation terms by

$$\bar{f}_x = \kappa_0 \nabla^2 \bar{u} + \bar{F}_x + \bar{S}_x, \tag{2.40}$$

$$\bar{f}_z = \kappa_0 \nabla^2 \bar{w} + \bar{F}_z + \bar{S}_z, \tag{2.41}$$

$$\bar{h} = \kappa_0 \nabla^2 \bar{b} + \bar{H} + \bar{Q} \tag{2.42}$$

where the filter terms are included in the $\bar{S}_x$, $\bar{S}_z$ and $\bar{Q}$ terms. We evaluate the effect of the dissipation by computing the net PV flux

$$j_y^{PV} = \bar{f}_x \frac{\partial \bar{\theta}}{\partial z} - \bar{f}_z \frac{\partial \bar{\theta}}{\partial x} - \bar{\eta}\bar{h}, \tag{2.43}$$

as well as the associated contributions from each dissipation type.

3. Results

Figure 14 shows the calculations of the resolved PV flux (including background viscous term and resolved-scale eddy term), subgrid-scale PV flux (including parameterized eddy and filter terms) and the net PV flux (2.43) for three different resolution (horizontal grid spacings are Δ, 3.75Δ and 10Δ, respectively). Note that the flux at the highest resolution is averaged over $17 \leq Ut/L \leq 18$, while the fluxes at other two resolutions are for $Ut/L = 17.5$.

As expected, for the highest resolution case the total PV flux is composed primarily of the resolved-scale eddy contribution. With increasing grid spacing, the parameterized PV flux becomes more and more important and the resolved-scale flux decreases. By $10\triangle$ the parameterized flux is clearly dominant.

Figure 15 shows the area-average of the different parts of PV flux as a function of grid spacing. The result is mostly consistent with what we concluded from Fig. 14: the resolved eddy contribution decreases in magnitude with grid spacing while subgrid-scale contributions increase with grid spacing. The trend in the net flux shows that the subgrid-scale contributions produce too much PV flux relative to the high-resolution results. By grid spacing of $\triangle x = L/3.7$ the flux is nearly twice that computed at $\triangle x = L/56$.

Further details can be found in EQ08.

G. Summary

The mean and turbulent behavior of a breaking mountain wave has been explored using an ensemble of large-eddy simulations.

The resolved-scale TKE production in the breaking wave is shown to be driven primarily by shear generation. This generation occurs mainly along the upper edge

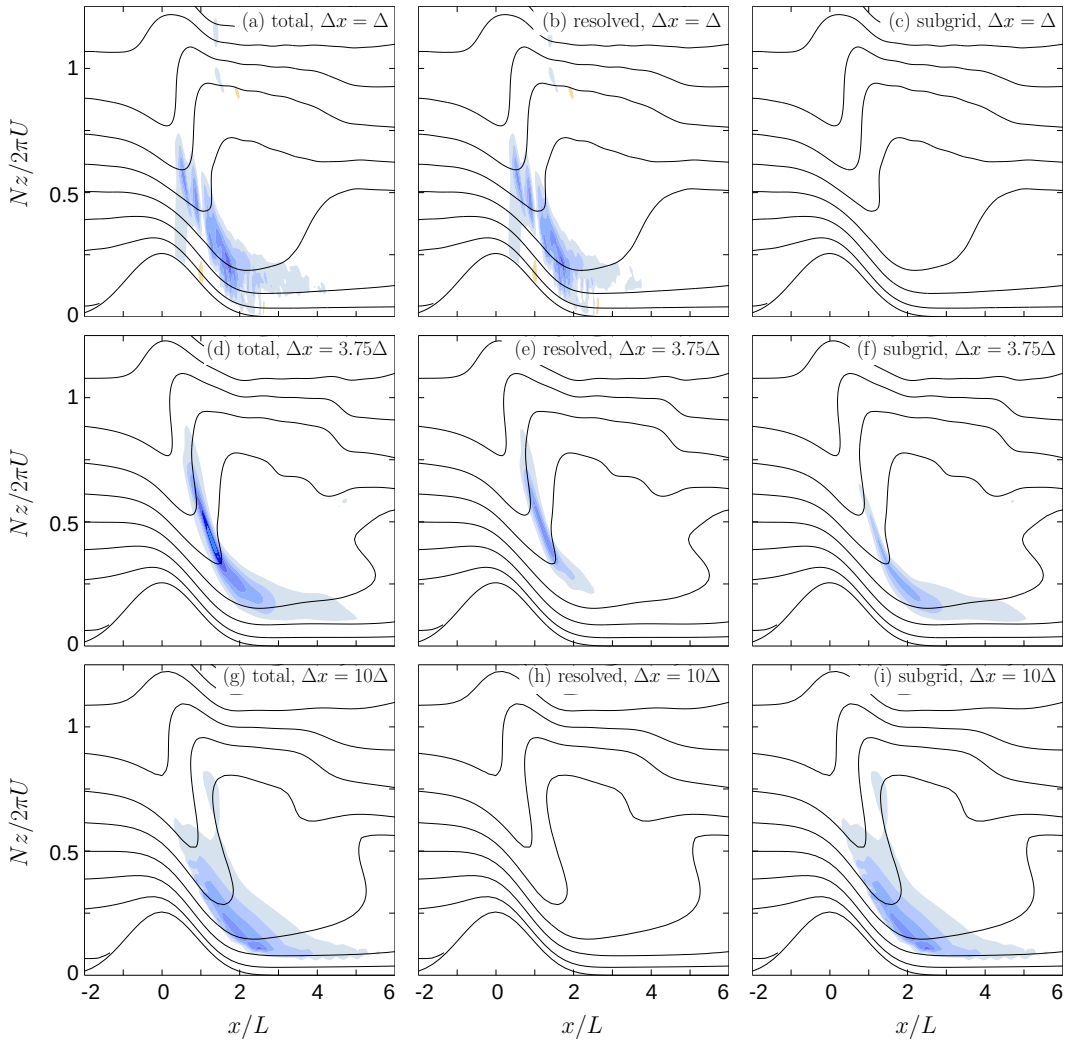

Fig. 14. (a) Total dissipative PV flux $L\, j_y^{PV} / N^2 U^2$ [see (2.43)] and (b) the resolved-scale and (c) subgrid-scale contributions to the flux [c.i. = 0.1; color shading as in Fig. 13] for $\Delta x = \Delta y = \Delta$. As in (a)–(c) except for grid spacings of (d)–(f) 3.75Δ and (g)–(i) 10Δ. (d)–(i) show $Ut/L = 17.5$, while (a)–(c) show the average over $17 \leq Ut/L \leq 18$. Solid lines in each panel show $\bar{\theta}/NU$ [c.i. = 1].

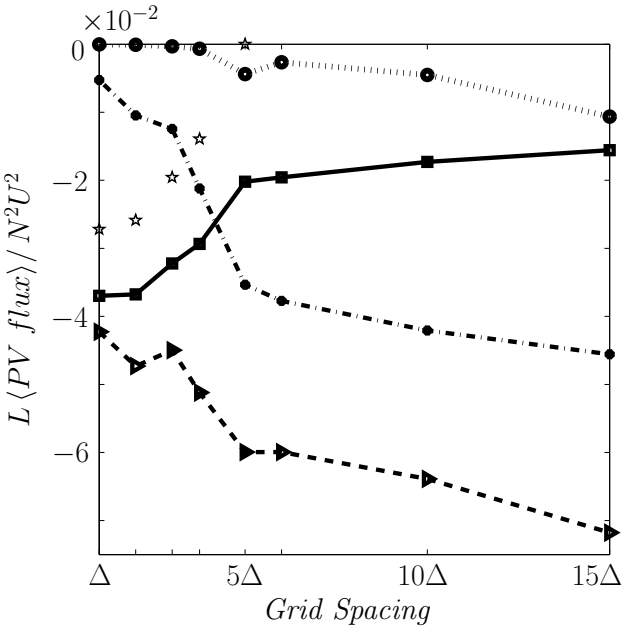

Fig. 15. Area-averaged PV fluxes as a function of grid spacing at time $Ut/L = 17.5$. Shown are the total PV flux $L < \mathrm{J}_y^{PV} > / N^2U^2$ (dashed-triangle), the net resolved-scale (resolved-scale eddy + background viscous) part of the flux (solid-square), the subgrid-scale parameterized eddy flux (dash-dot with solid circles), and the fourth-order filter contribution (dotted with open circles). The resolved-scale eddy term is shown by stars (no line), with the background viscous part then being the difference between the net resolved-scale and resolved-scale eddy parts.

of the lee-side shooting flow, where the mean-flow Richardson number is persistently less than 0.25. To a first approximation, the shear generation is balanced by the TKE dissipation. In term of TKE evolution, shortly after the onset of wave breaking a burst of TKE occurs near the ground with maximum TKE of nearly $0.5U^2$. The burst then dissipates and the TKE maximum shifts upstream and aloft and decays with time. The TKE pattern becomes roughly steady after time $Ut/L = 20$.

The dissipation of mean-flow wave energy is due mostly to the turbulent momentum fluxes and their tendency to act counter to the mean-flow disturbance wind. The resulting momentum dissipation acts mostly in the upper half of the lee-side shooting flow. This deceleration of the shooting flow leads to a loss in mean-flow Bernoulli function and the production of a cross-stream mean-flow PV flux.

The dependence of the eddy fluxes on the grid spacing was explored by computing a series of ensembles with grid spacings varying from $L/56$ to $L/3.7$. At resolution of $\triangle x = L/56$, the fluxes are mostly resolved. However, with increasing grid spacing the resolved-scale turbulent fluxes decline while the parameterized fluxes become larger. For our chosen parameter values the parameterization is found to produce too much PV flux. As a result, the area-averaged PV flux at grid spacing $L/3.7$ is almost twice that computed at $L/56$.

CHAPTER III

BACKGROUND AND OBJECTS FOR SEA BREEZE STUDY

As one of the oldest subjects in meteorology, the phenomena associated with sea breeze have been mentioned for over two hundred years. A variety of sea breeze characteristics has been documented. Many studies have investigated local features of the sea breeze. A few are about the mesoscale wave signal of sea breeze and the relation between sea breeze wave response and convective initiation, which are the main interest of our study. The following sections will briefly introduce our current understanding of each aspect. Section B will describe the motivations and objectives for the sea breeze study.

A. Background for Sea Breeze Study

1. Local features of sea breeze

The local sea breeze circulation is a closed mesoscale circulation in the vertical as predicted by the Bjerknes circulation theorem ([80]). However, this description is an oversimplification. The sea breeze is a complicated system which contains several components ([22]): sea breeze circulation, sea breeze gravity current, sea breeze front, sea breeze head, Kelvin-Helmholtz billows and convective internal boundary layer (Figure 16).

The sea breeze density current is a landward flow of the marine air ([81], [82]). It is caused by the different-density air over the land and the sea and the occurrence of it has been reproduced in numerous laboratory studies ([81], [34], [35]) and confirmed in observation studies ([83]). The top of the density current has strong shear, which often produces Kelvin-Helmholtz billows. As the density current comes onshore, the

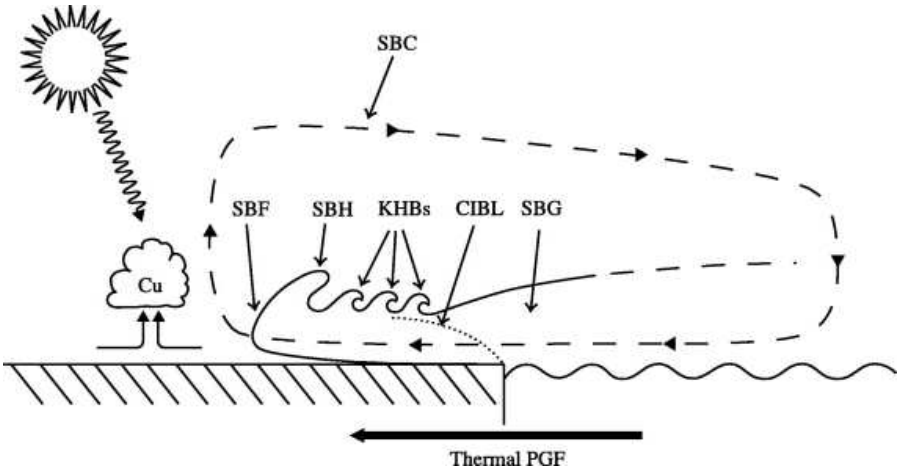

Fig. 16. Schematic sea breeze system. Details are discussed in the text.

lower part of the current comes in contact with the ground and becomes warmer. This leads to a turbulent lower layer, which is referred to the convective internal boundary layer ([84]; [85]).

The sea breeze front is the leading edge of the sea breeze density current. It is regarded to play an important role in initiating and enhancing the thunderstorms in the sea breeze ([86], [87] and [85]) and lifting pollutants aloft ([88],[89]). The formation and character of the sea breeze front have been well documented in observations and numerical models ([32], [90], [91], [92], [93], [94], [87] and so on). The sea breeze front is deeper than the gravity current behind it, with the top of sea breeze front referred to as the sea breeze head. Note that the sea breeze front is characterized by the nonlinear processes, which makes it impossible to be modeled by linear simulations ([95]).

Since these local features of the sea breeze can be observed directly, their character has been studied thoroughly through different approaches, including observational, numerical and laboratory. Knowledge of the local features of the sea breeze has been well-established on the basis of these numerous studies.

2. Mesoscale wave signal of sea breeze

A few studies have pointed out that the sea breeze also has a mesoscale wave signature. [36] were the first to discuss this wave response in terms of a linear sea-breeze model with a specified oscillating temperature gradient. The character of the waves depended on latitude and such a wave was most prominent at the equator. In their subsequent nonlinear study, [96] found that the mesoscale waves were weaker than in the linear model in the tropics.

This idea was later explored in greater detail by [37, hereafter R83], who considered the linear theory for the problem of an oscillating heat source in a resting and frictionless background state. R83 showed that the solution is a propagating wave response whenever the Coriolis parameter f is smaller than diurnal frequency ω (i.e., equatorward of 30^{o} latitude) while the sea breeze problem is elliptical when $f > \omega$. The circulation of the linear sea breeze is π out of phase with the heating in the tropics while the circulation is in phase with the heating when $f > \omega$. The vertical scale of the sea breeze is set externally by the vertical scale of the heating, with the length scale varying with latitude as $|f^2 - \omega^2|^{-1/2}$.

[38] extended many of these ideas to a nonlinear context using numerical simulations. They also concluded that the sea breeze had fundamentally different behavior when $f > \omega$ and $f < \omega$, which meant that the linear model to some extent could capture the basic dynamics of the complex nonlinear phenomena. [39] extended the linear theory of R83 to include aperiodic heat forcing. They also analyzed the time scale of the wave phenomena of sea breeze in the tropics and pointed out that it would take a long time to observe the internal-inertio wave in reality.

3. Sea breeze wave response and convective initiation

Recently, observational studies such as [40] and [41, 42] have suggested that diurnal coastal gravity waves may play a role in initiating convection far offshore. The hypothesis of a diurnal signal being propagated through gravity waves was first mentioned by [40] on the base of CLAUS satellite observation. With the CLAUS data, the oscillation of mean brightness temperature showed that well organized convection mainly appeared within the region where the orographic influence was large. This implied that the mountain effect was possibly important. The propagation speed of the diurnal signal was between 15 and 20 m/s which was consistent with a gravity wave speed. According to these phenomena, the results suggested that gravity waves might be a possible mechanism of the diurnal cycle of the oceanic convection and that this gravity wave was emanated by the diurnal heat anomaly of the elevated terrain.

The gravity wave mechanism assumption was then examined by a series of studies ([41], [97], [42]) from the perspective of observations and numerical simulations. Sensitivity experiments showed that the presence of the mountain was a dominant factor for the rainfall pattern. In their results, the observed night / morning offshore convection seemed to be activated by a wave of temperature anomaly. The propagation speed of the temperature anomaly was consistent with the linear hydrostatic gravity wave speed, leading the authors to infer that the initiation and propagation of offshore convection were through gravity waves. Since the temperature anomaly spread out from land to sea, they concluded that the forcing for the diurnal temperature wave was uneven land heating which was enhanced by the elevated mountain. The authors suggested that the properties of the waves were not fundamentally changed by their interaction with moist processes.

B. Motivations and Objectives

The gravity wave hypothesis of Mapes and others has received significant attention in recent years. Researchers have broadly used this proposition to explain the diurnal cycle of rainfall over the coastal region ([98]; [99]; [100] and so on). However, from the theory perspective the detailed understanding of these waves is limited to relatively simple cases–particularly, the no-wind and no-terrain case studied by R83 and others. The role of the background wind and the terrain in these flows has by comparison received relatively little attention.

With such motivation in mind, the general objective of this project is to explore the mesoscale wave aspects of the sea breeze from an idealized theoretical and modeling perspective. Our particular interest in this work will be the role of the background wind and the terrain in modifying the wave response. More specifically, the proposed study aims to address three goals of increasing complexity:

- To extend the linear wave theory of R83 to include the effects of background wind.
- To explore the combined effects of wind and topography on the linear wave response.
- To address the nonlinear behavior of the system by considering forcing of increasing amplitude.

To keep the problem tractable, for all three objectives our attention is limited to 2D flow with no background rotation (i.e., the equatorial case)

CHAPTER IV

LINEAR THEORY CALCULATIONS FOR THE SEA BREEZE IN A BACKGROUND WIND: THE EQUATORIAL CASE

A. Chapter Outline

A useful starting point for understanding nonlinear phenomena (like the sea breeze) is to first understand the corresponding linear problem. There is a well-established and well-known linear theory for the sea breeze when there is no terrain and when the background wind is zero (the Rotunno solution). But there is no corresponding solution for the case with background winds.

The current study seeks to extend the linear theory of R83 by including the effect of background wind on the sea breeze wave response, which, to the best of our knowledge, has never been explored analytically. Section B gives the basic equations and the associated Fourier transform solution. Section C revisits the no-wind linear theory of R83. The solution with the effect of the background wind is provided in section D. The spatial structure of the sea breeze wave response is discussed in terms of group propagation in section E. Summary is presented in section F.

B. Basic Methods

1. Basic equations and scaling parameters

We consider a 2D, Boussinesq and hydrostatic flow as linearized about a uniform background state with background wind speed U. Attention is limited to the equatorial case so that the Coriolis parameter is taken to be zero. The primitive equations

in dimensional form (as indicated by asterisks) are then given by

$$\frac{\partial u^*}{\partial t^*} + U\frac{\partial u^*}{\partial x^*} = -\frac{\partial P^*}{\partial x^*} \tag{4.1}$$

$$\frac{\partial P^*}{\partial z^*} = b^* \tag{4.2}$$

$$\frac{\partial b^*}{\partial t^*} + U\frac{\partial b^*}{\partial x^*} + N^2 w^* = Q^* \tag{4.3}$$

$$\frac{\partial u^*}{\partial x^*} + \frac{\partial w^*}{\partial z^*} = 0 \tag{4.4}$$

where u^* and w^* are the disturbance velocities in x^* and z^* directions; P^* is the Boussinesq disturbance pressure; b^* is the buoyancy; and N is the background state static stability. Q^* is the diabatic heating profile, which in principle includes both the turbulent transfer of heat by boundary-layer eddies and the effects of radiation. Following R83, we simplify the problem as much as possible by letting Q^* be strictly periodic in time. Specifically

$$Q^* = \frac{Q_0}{\pi}\left(\frac{\pi}{2} + \tan^{-1}\frac{x^*}{L}\right)\exp\left(-\frac{z^*}{H}\right)\cos(\omega t^*), \tag{4.5}$$

where Q_0, L, H and ω are the constant heating amplitude, half width of the coastal zone, heating depth and diurnal frequency, respectively. Here the coastline is at $x^* = 0$ with land to the right ($x^* > 0$) and sea to the left.

The lower boundary is assumed flat so that $w^* = 0$ at $z^* = 0$. Apart from the diurnal oscillations in b^* and P^* over land, the disturbance is assumed to vanish as $|x^*| \to \infty$.[1] The domain is unbounded aloft with a radiation condition applied as $z^* \to \infty$.

[1]The basis for this assumption is that the velocity field responds only to gradients in the heating rather than the heating itself. To see this, consider a problem in which the heat source extends uniformly to infinity in both directions. The pressure and buoyancy in this problem both oscillate, but no horizontal gradients are formed and no motion occurs [cf. (4.1) and (4.4), or equivalently (4.12)]. The same holds for our problem as $x \to \infty$.

The system is nondimensionalized using scaling factors derived from the $U = 0$ solution of R83. Specifically, R83 showed that for a resting background state the depth scale of the disturbance is set externally by the vertical scale of heating (i.e., by H). The horizontal scale is then given by $H/\delta = NH/\omega$, where $\delta = \omega/N$ is the geometric aspect ratio (depth / length) set by the associated gravity wave dispersion relation (see R83). The time scale is determined by the period of the heating forcing. The rest of the scales then follow from the dominant balances in (1)-(4). A list of all the scaling factors is

$$
\begin{aligned}
x^* &= \frac{NH}{\omega}x, & z^* &= Hz, & t^* &= \frac{t}{\omega},\\
Q^* &= Q_0 Q, & u^* &= \frac{Q_0}{N\omega}u, & w^* &= \frac{Q_0}{N^2}w,\\
b^* &= \frac{Q_0}{\omega}b, & P^* &= \frac{Q_0 H}{\omega}P,
\end{aligned}
$$

where again the asterisks indicate dimensional quantities. Substituting the scaling factors into (4.1) - (4.5), we have a set of nondimensional equations as

$$\frac{\partial u}{\partial t} + \mathcal{U}\frac{\partial u}{\partial x} = -\frac{\partial P}{\partial x} \tag{4.6}$$

$$\frac{\partial P}{\partial z} = b \tag{4.7}$$

$$\frac{\partial b}{\partial t} + \mathcal{U}\frac{\partial b}{\partial x} + w = Q \tag{4.8}$$

$$\frac{\partial u}{\partial x} + \frac{\partial w}{\partial z} = 0 \tag{4.9}$$

with

$$Q = \frac{1}{\pi}\left(\frac{\pi}{2} + \tan^{-1}\frac{x}{\mathcal{L}}\right)\exp(-z)\cos(t), \tag{4.10}$$

where $\mathcal{U} = U/NH$ is the nondimensional background wind speed[2] and $\mathcal{L} = \omega L/NH$

[2]Physically, the parameter $\mathcal{U}$ measures the size of the background wind speed relative to the characteristic phase speeds present in the $U = 0$ case. Since the depth scale for the R83 solution is H, the relevant phase speed is then NH. The

is the nondimensional half width of the coastal zone. It is obvious that the only two control parameters for the nondimensional problem are then $\mathcal{U}$ and $\mathcal{L}$.

Solutions are sought in terms of a streamfunction ψ, defined by

$$u = \frac{\partial \psi}{\partial z} \qquad \text{and} \qquad w = -\frac{\partial \psi}{\partial x}, \tag{4.11}$$

Reducing (4.6)-(4.9) to a single equation in ψ then gives

$$\left(\frac{\partial}{\partial t} + \mathcal{U}\frac{\partial}{\partial x}\right)^2 \frac{\partial^2 \psi}{\partial z^2} + \frac{\partial^2 \psi}{\partial x^2} = -\frac{\partial Q}{\partial x}. \tag{4.12}$$

2. Fourier transform solution

The Fourier transform of (4.12) gives

$$\left(\frac{\partial}{\partial t} + i\mathcal{U}\kappa\right)^2 \frac{\partial^2 \tilde{\psi}}{\partial z^2} - \kappa^2 \tilde{\psi} = -e^{-\kappa \mathcal{L}} e^{-z} \frac{e^{it} + e^{-it}}{2}, \tag{4.13}$$

where κ is the nondimensional horizontal wavenumber and $\tilde{\psi}$ is the Fourier transform of ψ defined by

$$\tilde{\psi}(\kappa, z, t) = \int_{-\infty}^{\infty} \psi(x, z, t) e^{-i\kappa x}\, dx.$$

Solutions are obtained by first decomposing the forcing into the e^{it} and e^{-it} modes and then solving for each mode independently. Writing the solution for a given mode in the form

$$\tilde{\psi}(\kappa, z, t) = \hat{\psi}(\kappa, z) e^{\pm it} \tag{4.14}$$

and substituting into the wave equation (4.13) then gives

$$\hat{\omega}^2 \frac{d^2 \hat{\psi}}{dz^2} + \kappa^2 \hat{\psi} = \frac{1}{2} e^{-\kappa \mathcal{L}} e^{-z}, \tag{4.15}$$

---

combination U/NH is also sometimes referred to as the *thermal Froude number* (e.g., [101], chap. 6)

where $\hat{\omega} = \pm 1 + \mathcal{U}\kappa$ is the dimensionless intrinsic frequency, with the $\pm$ matching that given in (4.14).

Since ψ is real, we can specify κ so as to always be positive. The e^{it} and e^{-it} modes then correspond to leftward and rightward propagating waves relative to the ground, respectively. The phase speed of the waves is given by $c_x = \mp 1/\kappa$, showing that longer waves propagate faster than shorter waves.

For concreteness we restrict attention to the case $\mathcal{U} \geq 0$. (The $\mathcal{U} < 0$ case is simply the reflection about the $x = 0$ axis.) In the flow-relative (or intrinsic) frame, the specified heat source is then seen as propagating to the left at speed $\mathcal{U}$, which causes the Fourier modes to be Doppler shifted. For leftward-moving (or e^{it}) modes, the intrinsic propagation is faster than the ground-relative value, implying that $\hat{\omega}$ for these modes is greater than the diurnal frequency (i.e., $\hat{\omega} > 1$). For rightward-moving (or e^{-it}) modes with phase speeds greater than $\mathcal{U}$ (i.e., long waves with $1/\kappa > \mathcal{U}$), the intrinsic propagation is slower than the ground-relative value so that the intrinsic frequency satisfies $\hat{\omega} > -1$. Rightward-moving waves with phase speeds less than $\mathcal{U}$ (i.e., short waves with $1/\kappa < \mathcal{U}$) are seen as leftward moving in the intrinsic frame and thus have $\hat{\omega} > 0$.

The solutions to (4.15) are obtained in terms of Green's functions in the vertical with a radiation condition applied aloft. The result is

$$\hat{\psi}(\kappa, z) = \begin{cases} -e^{-\kappa\mathcal{L}}(e^{imz} - e^{-z})/(2\hat{\omega}^2 + 2\kappa^2), & \hat{\omega} > 0 \\ -e^{-\kappa\mathcal{L}}(e^{-imz} - e^{-z})/(2\hat{\omega}^2 + 2\kappa^2). & \hat{\omega} < 0 \end{cases} \tag{4.16}$$

where $m = \kappa/|\hat{\omega}|$ is the nondimensional vertical wavenumber (defined so as to always be positive). Note that the selection of the vertical mode is determined by the intrinsic phase propagation rather than the phase propagation relative to the ground. Leftward propagating modes in the intrinsic frame ($\hat{\omega} > 0$) all have negative phase tilts (i.e.,

e^{imz} modes) while rightward propagating modes in the intrinsic frame ($\hat{\omega} < 0$) all have positive phase tilts (e^{-imz} modes). The solution for a given mode then follows from (4.14), with the full solution to (4.13) being the superposition of the e^{it} and e^{-it} cases.

According to (4.11), the Fourier transform for w is given by $\tilde{w} = -i\kappa\tilde{\psi}$, while the solution for $\tilde{u}$ follows from the appropriate z derivatives of (4.16).

C. Review: The No-Wind Case

The solution for $\mathcal{U} = 0$ has been described in some detail by R83. Here the basic properties of this solution are reviewed in preparation for the $\mathcal{U} \neq 0$ case described in section D.

1. Computation

Setting $\mathcal{U} = 0$ in (4.12) leads to the Fourier solution

$$\psi = I_1 + I_2$$

where

$$I_1 = -\frac{1}{2\pi}\int_0^\infty \frac{e^{-\kappa\mathcal{L}}}{\kappa^2+1}(e^{imz} - e^{-z})e^{i(\kappa x+t)}\,d\kappa \tag{4.17}$$

and

$$I_2 = -\frac{1}{2\pi}\int_0^\infty \frac{e^{-\kappa\mathcal{L}}}{\kappa^2+1}(e^{-imz} - e^{-z})e^{i(\kappa x-t)}\,d\kappa, \tag{4.18}$$

consist of the leftward and rightward propagating modes, respectively. It should be understood that only the real parts in (4.17) and (4.18) are physically meaningful. As in section B, the vertical wavenumber m is defined so that $m = \kappa$. Solutions for u and w follow from the derivatives of (4.17) and (4.18), as described in section B.

Inspection of the integrals shows that the integrands in (4.17) and (4.18) are well-

behaved everywhere along the real κ axis. Numerical computation of the integrals is thus straightforward and follows methods outlined for the I_1 case in the appendix.

2. Basic morphology

With $\mathcal{U} = 0$ the only nondimensional control parameter for the flow is the coastal width $\mathcal{L}$, with the figures in R83 being for $\mathcal{L} = 0.2$. An analogous calculation for $\mathcal{L} = 0.1$ is shown in Fig. 17. The solution is localized along two parallel wave beams with centers at $z = x$ and $z = -x$. As shown by R83, the slopes of these wave beams correspond to energy propagation for diurnal gravity modes. In the present case the energy propagates away from the heat source gradient near $x = 0$.

With $\mathcal{L} = 0.1$, the vertical scale of the wave beams is set by the heating depth, while the dominant horizontal scale is obtained through the aspect ratio δ (as in section B). These length and depth scales form the basis of our scaling, so that in nondimensional terms both the width and depth of the wave beams are roughly one. The phase lines of the modes propagate downward as time evolves (as seen in Fig. 17a,c or 17b,d). Surprisingly, the cross-coastline winds are nearly π out of phase with the heating. Broadly speaking, this π phase lag results from the $\pi/2$ lag between the heat source and the temperature (and hence pressure) gradient, as well as the $\pi/2$ lag between the pressure gradient and the wind. Detailed explanation can be found in R83.

Finally, Figs. 17e,f exhibit the decomposition of the horizontal velocity u into leftward and rightward propagating modes. As expected, the branch at $x > 0$ consists of rightward propagating modes, while branch at $x < 0$ consists of leftward propagating modes.

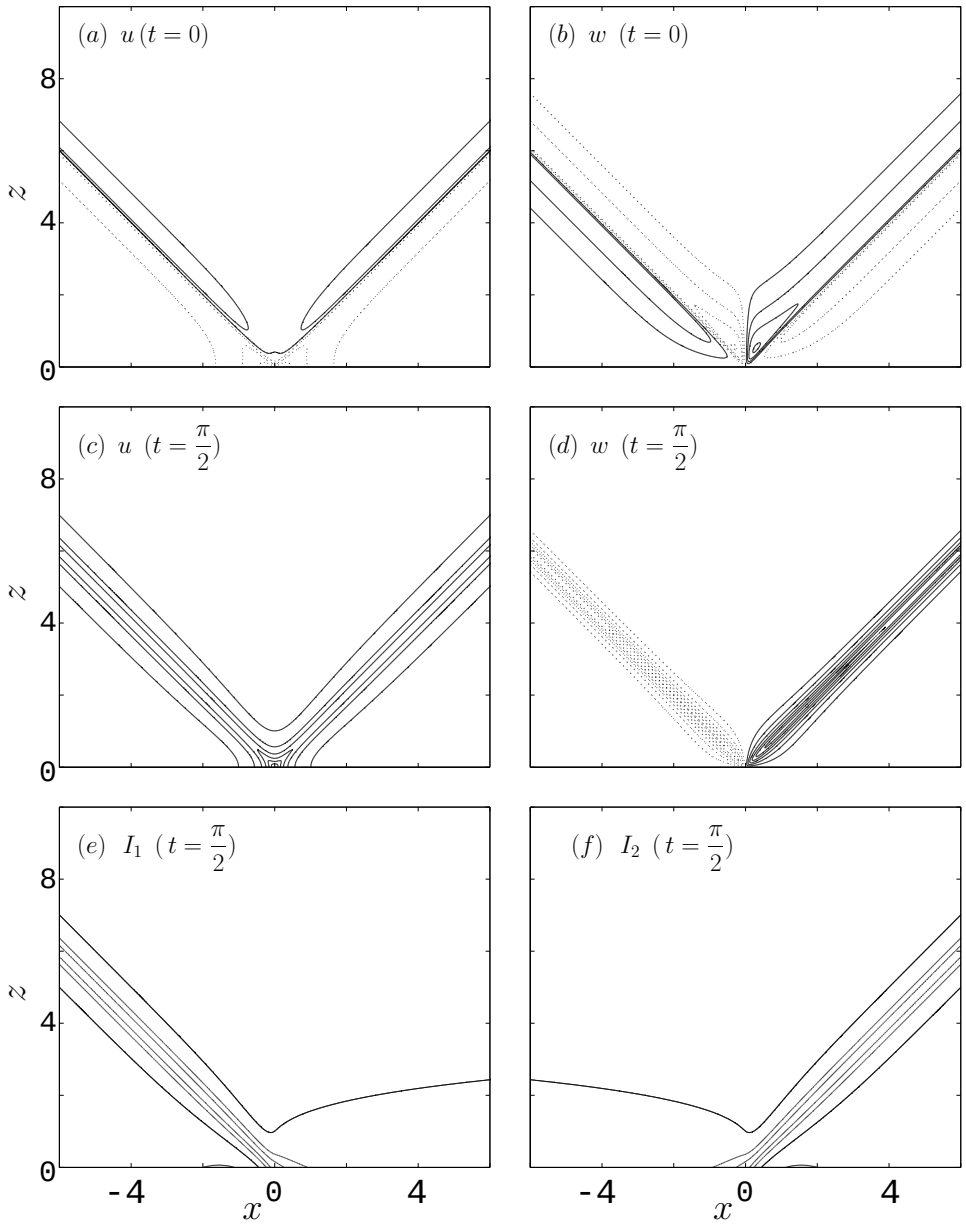

Fig. 17. Horizontal and vertical velocity components for $\mathcal{U} = 0$ and $\mathcal{L} = 0.1$. Horizontal velocity u at times $t =$ (a) 0, (c) $\pi/2$ [contour interval (c.i.) $= 0.1$; solid contours, positive; dotted contours, negative]. Vertical velocity w at times $t =$(b) 0, (d) $\pi/2$ [c.i. $= 0.05$ with zero contour straddled]. (e) Leftward-moving (or I_1) and (f) rightward-moving (or I_2) parts of u at $t = \pi/2$. Solutions for $t = \pi$ and $3\pi/2$ are simply the negatives of the solutions at $t = 0$ and $\pi/2$, respectively.

3. $\mathcal{L}$ dependence

For reference, suppose we pick characteristic dimensional values of $N = 0.01$ s^{-1}, $\omega = 2\pi$ day $^{-1}$, $H = 800$ m and $L = 10$ km. Combining these then gives a characteristic nondimensional coastal width of $\mathcal{L} \sim 0.1$, as considered above. But in reality, $\mathcal{L}$ might be larger or smaller than this value, depending on the values N, H and L in a given case.

The sensitivity of the $\mathcal{U} = 0$ solution to changes in $\mathcal{L}$ is illustrated by Figs. 17c and 18. As expected, for small $\mathcal{L}$ (Figs. 18a and 17c) the depth scale is set by the heating depth while the length scale follows from the dynamical aspect ratio. The result is that the dominant horizontal and vertical scales are both roughly independent of $\mathcal{L}$ for small $\mathcal{L}$, with the dominant wavenumber given by $m = \kappa \simeq 1$. However, according to (4.17) and (4.18) the power at this dominant wavenumber varies roughly as $e^{-\mathcal{L}}$, so that as $\mathcal{L}$ increases the amplitude of the solution becomes smaller (compare Figs. 17c and 18a). As $\mathcal{L}$ is made still larger (as shown in Fig. 18b with $\mathcal{L} = 0.5$ and Fig. 18c with $\mathcal{L} = 1$), the scales start to change so that the horizontal scale is set by $\mathcal{L}$ while the vertical scale follows from the aspect ratio. And the amplitude continues to decrease.

D. Adding the Background Wind

The character of sea breeze in a background wind is examined in this section. As will be seen, the Doppler shifting of the modes can lead to significant differences from the $\mathcal{U} = 0$ solution.

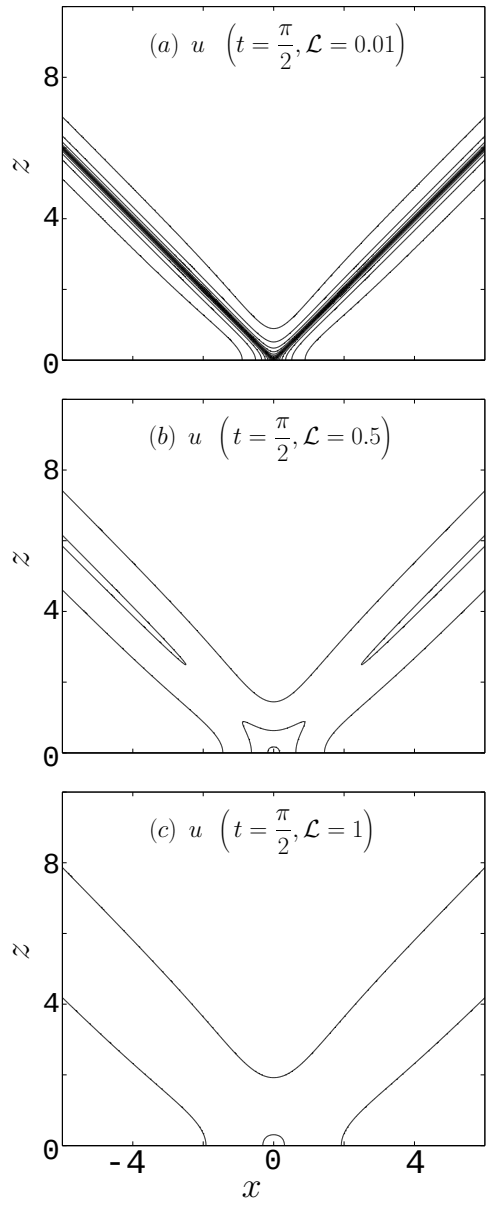

Fig. 18. Horizontal velocity u at time $t = \pi/2$ with coastal width $\mathcal{L}$ = (a) 0.01; (b) 0.5; (c) 1 [contours as in Fig. 1].

1. Computation

With $\mathcal{U} \neq 0$ in (16), the Fourier integral solution becomes

$$\psi = I_1 + I_2 + I_3$$

where the three different branches are defined by:

- Left-moving waves with $\hat{\omega} = 1 + \mathcal{U}\kappa > 0$

$$I_1 = -\frac{1}{2\pi} \int_0^\infty \frac{e^{-\kappa\mathcal{L}}}{\kappa^2 + (1+\mathcal{U}\kappa)^2} (e^{imz} - e^{-z}) e^{i(\kappa x + t)} \, \mathrm{d}\kappa \tag{4.19}$$

- Right-moving waves with $\hat{\omega} = -1 + \mathcal{U}\kappa < 0$

$$I_2 = -\frac{1}{2\pi} \int_0^{\kappa_\mathcal{U}} \frac{e^{-\kappa\mathcal{L}}}{\kappa^2 + (\mathcal{U}\kappa - 1)^2} (e^{-imz} - e^{-z}) e^{i(\kappa x - t)} \, \mathrm{d}\kappa \tag{4.20}$$

- Right-moving waves with $\hat{\omega} = -1 + \mathcal{U}\kappa > 0$

$$I_3 = -\frac{1}{2\pi} \int_{\kappa_\mathcal{U}}^\infty \frac{e^{-\kappa\mathcal{L}}}{\kappa^2 + (\mathcal{U}\kappa - 1)^2} (e^{imz} - e^{-z}) e^{i(\kappa x - t)} \, \mathrm{d}\kappa \tag{4.21}$$

The cutoff wavenumber $\kappa_\mathcal{U} = 1/\mathcal{U}$ in (4.20) and (4.21) is the critical wavenumber at which the rightward propagating phase speed matches the background wind speed. The vertical wavenumber is $m = \kappa/|\hat{\omega}|$ for all three branches.

It is worth noting that the integrands in both (4.20) and (4.21) become singular in the limit $\kappa \to \kappa_\mathcal{U}$, since $\hat{\omega} = -1 + \mathcal{U}\kappa \to 0$ in this limit so that $m \to \infty$. The result is that the $e^{\pm imz}$ terms oscillate infinitely fast with κ in this limit, which in turn complicates the numerical computation of the Fourier integrals. This is especially true for the horizontal velocity $u = \partial\psi/\partial z$, since the vertical derivative produces an amplitude singularity as well as a singular oscillation. Our approach to overcoming these problems is based on a method first proposed by [102] in the context of flow past topography. Broadly speaking, the basis of the method is to first remove the singular oscillation with an analytically integrable function and to then apply the numerical

quadrature only to the difference integral. Details of the method can be found in the appendix.

2. Basic inferences

To simplify terminology, we refer to the flow pattern illustrated by Fig. 1 as the R83 pattern and to the wavenumbers near $m \sim 1$ (which dominate the $\mathcal{U} = 0$ solution) as the R83 modes. Inspection of (4.19)-(4.21) then suggests two main impacts of the background wind: (i) the R83 modes in I_1 and I_2 will become Doppler shifted and dispersive; and (ii) the contribution from I_3 will become stonger as $\mathcal{U}$ increases. Here we briefly consider the $\mathcal{U}$ and $\mathcal{L}$ dependence of these effects.

For sufficiently small $\mathcal{U}$ the cutoff wavenumber $\kappa_{\mathcal{U}}$ in (4.21) is relatively large and the contribution from I_3 is therefore negligible. The two branches I_1 and I_2 in this limit are then analogous to the $\mathcal{U} = 0$ cases in (4.17) and (4.18), except that the R83 modes in the branches will be Doppler shifted to higher and lower intrinsic frequencies. Since the scale of R83 modes is roughly $\kappa \approx m \sim 1$, the extent of this frequency shifting will be determined premarily by $\mathcal{U}$ (and not by $\mathcal{L}$).

As $\mathcal{U}$ increases, $\kappa_{\mathcal{U}}$ becomes smaller and the I_3 modes will gradually become more important. Since $\hat{\omega}$ for these modes is dominated by $\mathcal{U}\kappa$ (instead of the diurnal frequency), the general behavior of these I_3 modes is expected to be broadly similar to flow past a stationary heat source (or equivalently to flow past topography). And as in the stationary heating or topography problems, we expect that the dominant w forcing for these modes will be near $\kappa \sim 1/\mathcal{L}$. A reasonable expectation then is that the I_3 modes will become important only once $\kappa_{\mathcal{U}} < 1/\mathcal{L}$, or equivalently $\mathcal{U}/\mathcal{L} > 1$.

3. $\mathcal{U}$ dependence

The $\mathcal{U}$ dependence of the solution for the case $\mathcal{L} = 0.1$ is illustrated in Figs. 19 and 20. Figure 19 shows the vertical velocity for increasing values of $\mathcal{U}$, while Fig. 20 shows the decomposition into I_1, I_2 and I_3 modes. For reference, thick solid lines in Fig. 20 show the raypaths for the $\mathcal{U} = 0$ solution, while the thick dashed lines show the raypaths for the R83 modes (i.e., modes with $m \sim 1$) as Doppler shifted for $\mathcal{U} \neq 0$. Details of the raypath calculations can be found in section E.

As expected, for $\mathcal{U} = 0.075$ the solution in Fig. 19a is composed primarily of the I_1 and I_2 branches (see Figs. 20a–c). For I_1 the Doppler shifting of the modes leads to higher intrinsic frequencies, and the phase lines and raypaths for this branch are thus more steeply inclined to the vertical than for $\mathcal{U} = 0$. The energy of the branch is also more widely dispersed, with shorter wavelengths having steeper energy propagation (see discussion in section E). By contrast, the I_2 modes are shifted to lower $|\hat{\omega}|$ and the phase lines and raypaths are therefore less steeply inclined (Fig. 20b).

With increasing $\mathcal{U}$ the raypaths for the I_1 and I_2 R83 modes become further rotated from the $\mathcal{U} = 0$ case (see the second through fourth rows in Fig. 20). However, a more significant change is the gradual appearance of the I_3 branch. The I_3 branch is composed of rightward propagating waves (relative to the ground) with negative phase tilts, and the character of this branch is thus fundamentally different from I_1 and I_2. Qualitatively, the wave pattern for I_3 closely resembles flow past a steady heat source or a topographic obstacle (see, e.g., [101], chaps. 5 and 6) rather than a stationary diurnal oscillation as in Fig. 17.

As suggested in section D2, the I_3 modes in Fig. 20 only become significant once $\mathcal{U}/\mathcal{L}$ is sufficiently large (roughly $\mathcal{U}/\mathcal{L} \approx 2$ in present case). For $\mathcal{U} = 0.25$ and $\mathcal{U} = 0.625$ the flow consists of relatively high wavenumber (since $\kappa_{\mathcal{U}}$ is still relatively

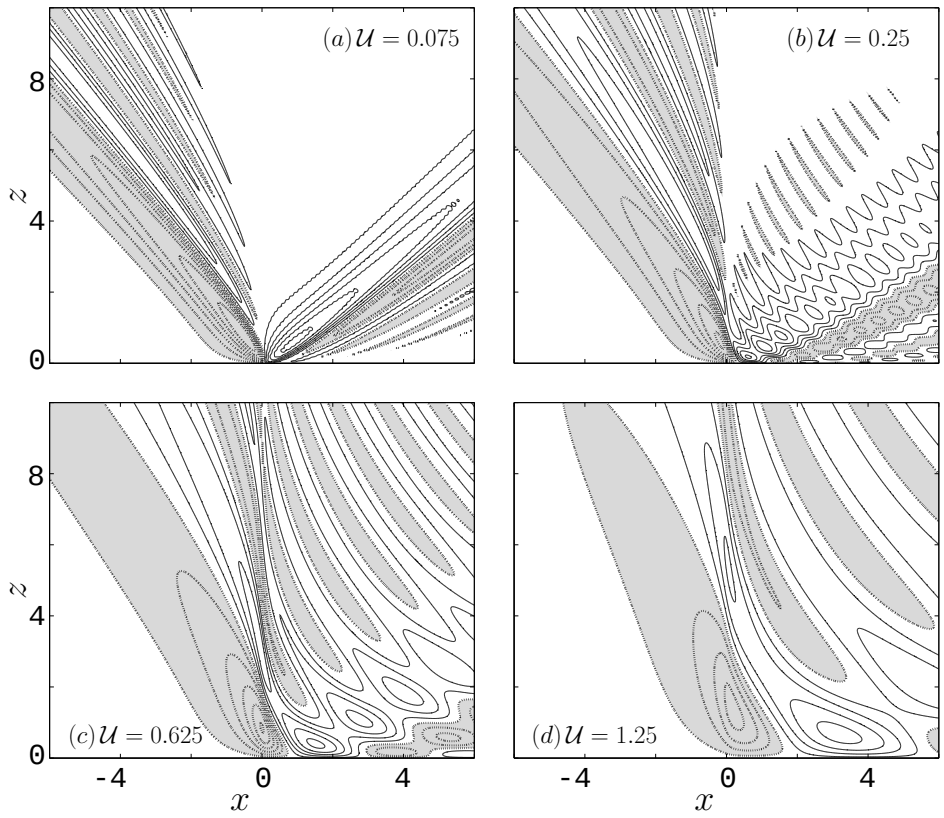

Fig. 19. Vertical velocity w at $t = \pi/2$ with $\mathcal{L} = 0.1$ and $\mathcal{U} =$ (a) 0.075, (b) 0.25, (c) 0.625; (d) 1.25 [c.i. = 0.04; solid lines, positive; dotted lines and shaded, negative].

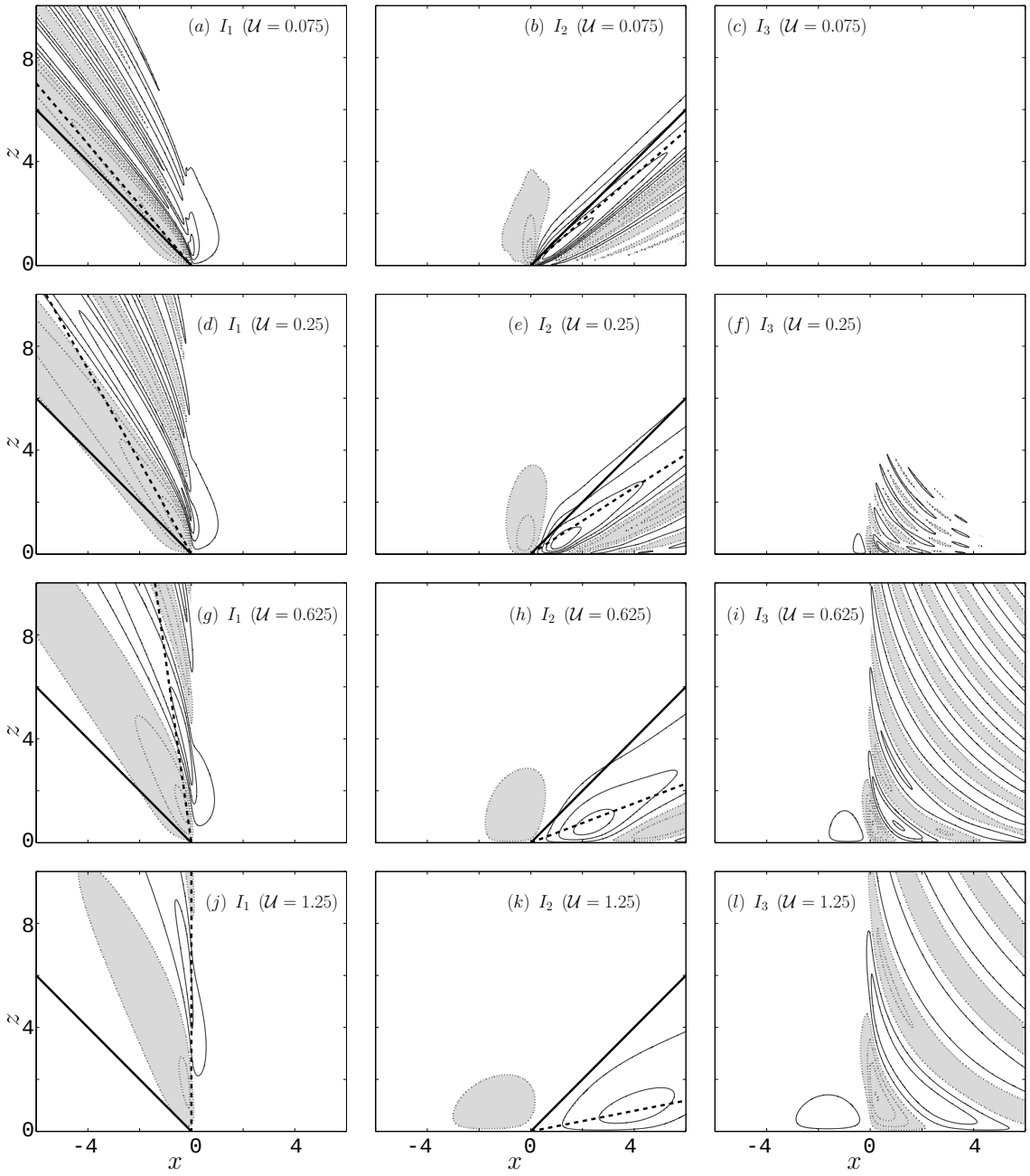

Fig. 20. I_1, I_2 and I_3 branches of vertical velocity w [c.i. $= 0.04$] at $t = \pi/2$ with $\mathcal{L} = 0.1$ and different background wind $\mathcal{U}$. (a) I_1, (b) I_2 and (c) I_3 with $\mathcal{U} = 0.075$. As in (a)–(c), but with (d)–(f) $\mathcal{U} = 0.25$, (g)–(i) $\mathcal{U} = 0.625$ and (j)-(l) $\mathcal{U} = 1.25$. Thick solid lines for I_1 and I_2 show the ray paths for the $\mathcal{U} = 0$ solution of R83. Thick dashed lines show ray paths for the Doppler-shifted R83 modes.

large) I_3 modes superimposed on a Doppler tilted R83 pattern (see Figs. 19b,c and the second and third rows of Fig. 20). However, by $\mathcal{U} = 1.25$ (or $\mathcal{U}/\mathcal{L} = 12.5$) the I_3 branch is the dominant part of the solution.

Figure 21 shows the horizontal velocity u corresponding to the vertical velocity shown in Fig. 19. The general trend in the solution with increasing $\mathcal{U}$—Doppler tilting of the R83 modes and the gradual increase in I_3—is the same as for vertical velocity. The main difference is that for large $\mathcal{U}$, the I_3 part of the u disturbance is localized downstream and closer to the ground (compare Figs. 19d and 21d). Further discussion of this point is given in section E3. Note that the $\mathcal{U}$ dependence in Figs. 19 and 21 explains some of the asymmetric features observed in previous analytical and modeling studies, such as that of [29].

4. Time evolution

Figure 22 displays the time evolution for both the decompostion and total vertical velocity fields with $\mathcal{U} = 0.875$ and $\mathcal{L} = 0.1$. As in the $\mathcal{U} = 0$ case (cf. Fig. 17) the phase lines in the I_1 and I_2 branches (Figs. 22a,d) propagate downward through the respective wave envelopes with time. However, in the ground-relative frame the I_3 modes are rightward propagating, and the phase lines for the I_3 branch (Figs. 22b,e) thus propagate upwards and downstream. The phase evolution for the total fields thus has elements of both these behaviors.

5. $\mathcal{L}$ dependence

The $\mathcal{L}$ dependence of the I_1, I_2 and I_3 modes at fixed $\mathcal{U} = 0.5$ is illustrated by Fig. 23. As expected, for the I_1 and I_2 branches the Doppler tilting and general wave patterns are essentially independent of $\mathcal{L}$ (for sufficiently small $\mathcal{L}$). However, the amplitudes of the two branches increase as $\mathcal{L}$ decreases, much as in the $\mathcal{U} = 0$ case of section C3.

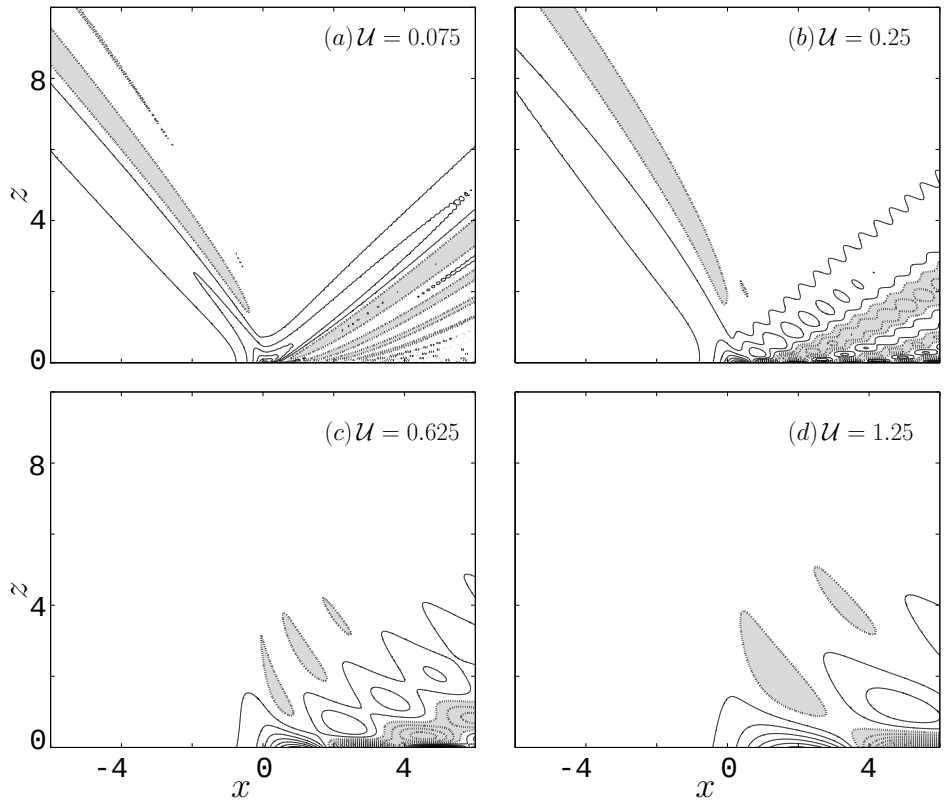

Fig. 21. Horizontal velocity u at $t = \pi/2$ with $\mathcal{L} = 0.1$ and $\mathcal{U} =$ (a) 0.075, (b) 0.25, (c) 0.625 and (d) 1.25 [c.i. $= 0.1$; solid lines, positive; dotted lines and shaded, negative].

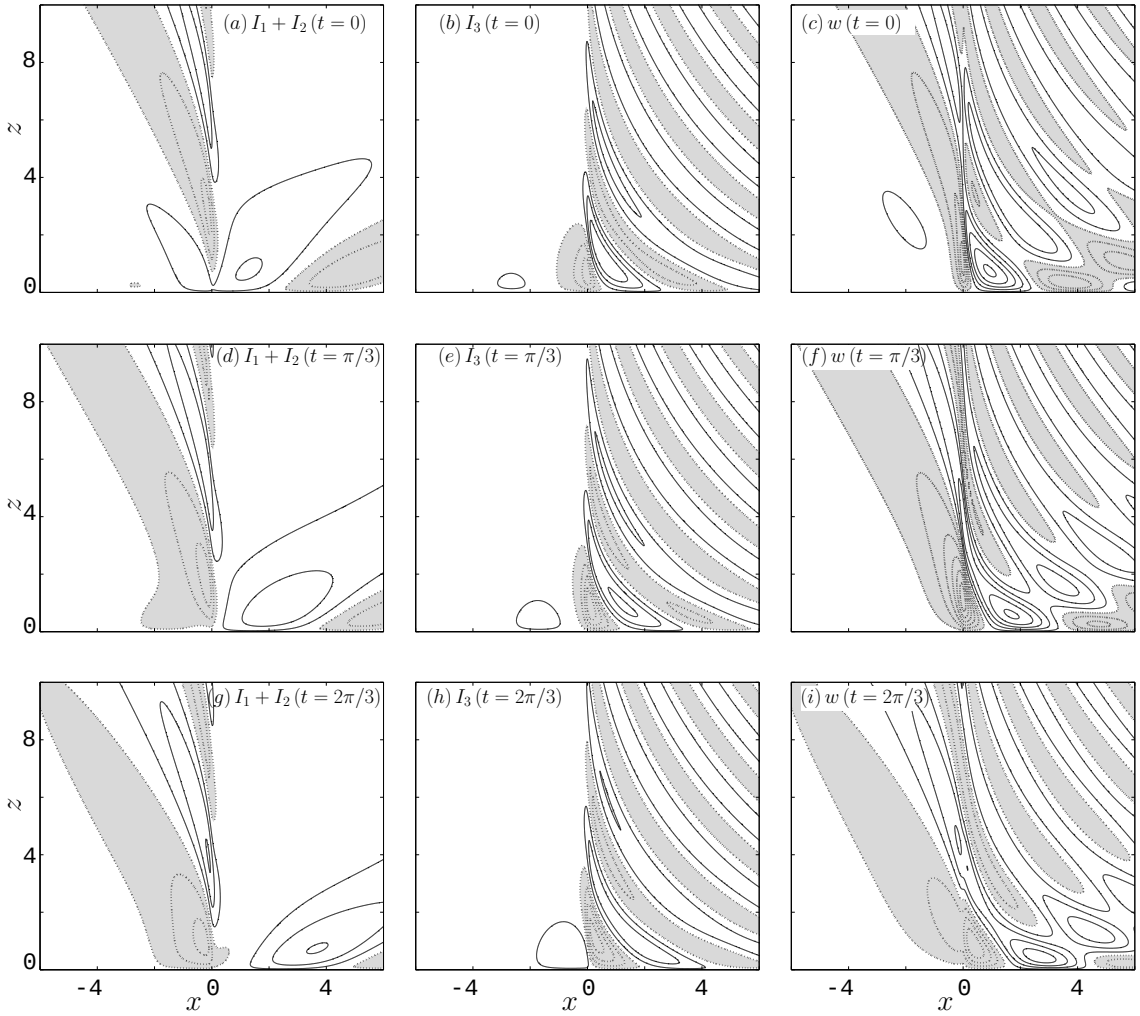

Fig. 22. Time evolution of both decomposed and total vertical velocity w [c.i. = 0.04] with $\mathcal{U} = 0.875$ and $\mathcal{L} = 0.1$. Sum of I_1 and I_2 modes at $t =$ (a) 0, (d) $\pi/3$ and (g) $2\pi/3$. As in (a), (d), (g), but for (b), (e), (h) I_3 modes and (c), (f), (i) total w.

For the I_3 branch the disturbance becomes relatively more important (compared to I_1 and I_2) as $\mathcal{L}$ decreases so that $\mathcal{U}/\mathcal{L}$ increases.[3] And as in Fig. 20, the noticeable onset of the I_3 branch occurs roughly near $\mathcal{U}/\mathcal{L} \approx 2$.

Taken together, the results shown in Figs. 19–23 generally reinforce the basic inferences made in section D2—specifically, that the I_1 and I_2 branches are determined largely by $\mathcal{U}$ while the importance of the I_3 branch (relative to I_1 and I_2) depends primarily on $\mathcal{U}/\mathcal{L}$. Various different values of $\mathcal{U}$ and $\mathcal{L}$ can thus lead to various combinations of these two effects (as seen by comparing Figs. 20 and 23). In the following section we consider the overall spatial structures of these three branches in greater detail.

E. Group Propagation and Wave Scales

The present section explores the structure and spatial scales of the three branches in terms of group propagation arguments.

Generally, the solution (4.19)-(4.21) consists of Fourier wave modes of the form of $\exp(i\kappa x + i\lambda z + i\sigma t)$, where in the present case $\lambda = \pm m$, $\sigma = \pm 1$ and κ is positive. The dispersion relation for the these Fourier modes can be described uniformly by

$$\sigma + \mathcal{U}\kappa = \frac{\kappa}{\lambda} \tag{4.22}$$

where the sign of λ accounts for direction of intrinsic phase propagation. The corresponding group propagation is given by

$$c_{gx} = -\frac{\partial \sigma}{\partial \kappa} = -\frac{1}{\lambda} + \mathcal{U} \qquad \text{and} \qquad c_{gz} = -\frac{\partial \sigma}{\partial \lambda} = \frac{\kappa}{\lambda^2},$$

[3] To see this, consider the changes in amplitudes for the three branches as $\mathcal{L}$ decreases. Between $\mathcal{L} = 0.2$ and $\mathcal{L} = 0.04$ in Fig. 23 the amplitudes of the I_1 and I_2 branches increase by 50%, whereas the increase in the I_3 amplitude is nearly a factor of 3.

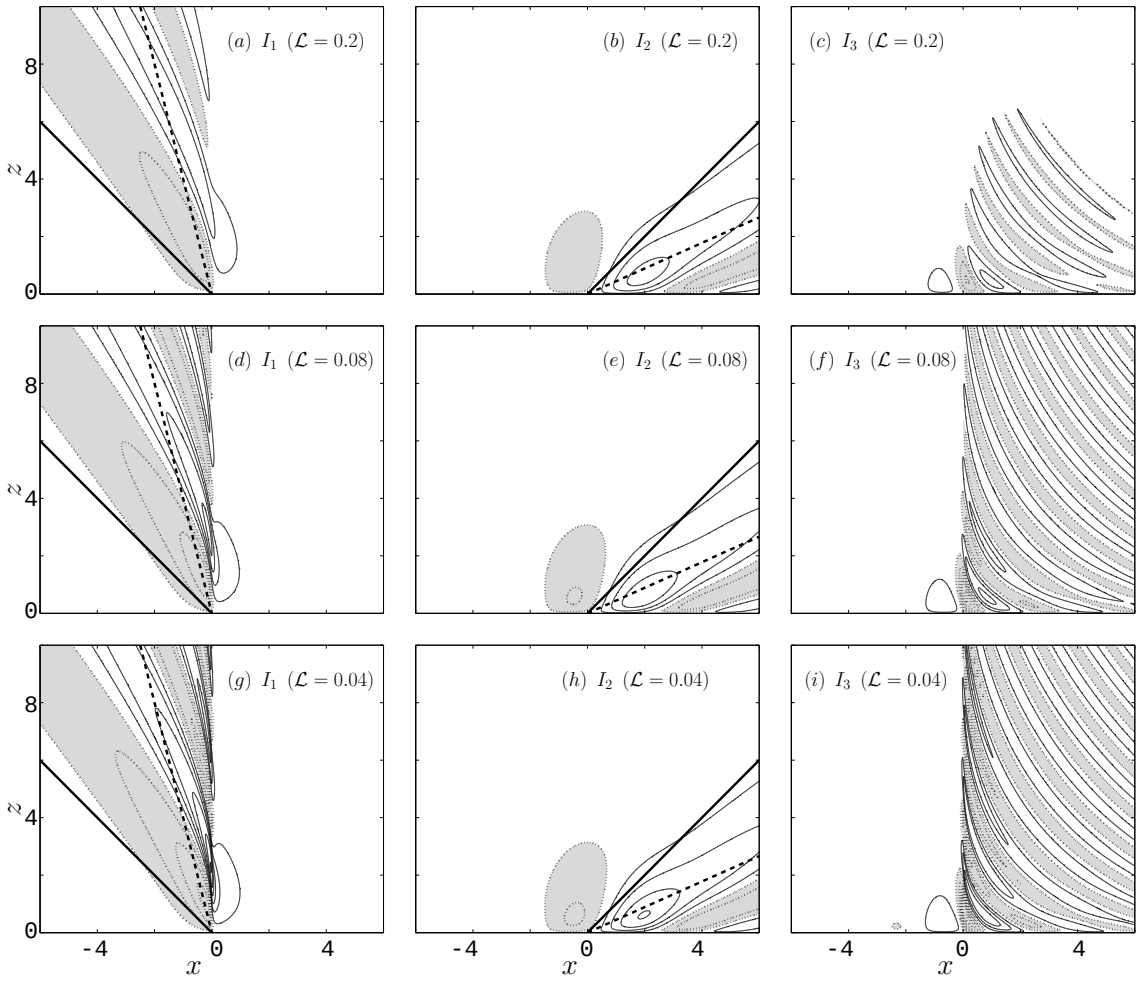

Fig. 23. Decomposition of w [c.i. $= 0.04$] into I_1, I_2 and I_3 branches for $\mathcal{U} = 0.5$ and varying $\mathcal{L}$ at time $t = \pi/2$. (a) I_1, (b) I_2 and (c) I_3 for coastal width $\mathcal{L} = 0.2$. As in (a)–(c), but for (d)–(f) $\mathcal{L} = 0.08$ and (g)–(i) $\mathcal{L} = 0.04$.

which implies raypaths of slope

$$\tan\theta = \frac{c_{gz}}{c_{gx}} = \frac{\kappa}{-\lambda + \mathcal{U}\lambda^2} \tag{4.23}$$

where θ is the angle between the raypath and the positive x axis. Note that for given $\mathcal{U}$ the raypath for fixed κ and λ is a straight line (i.e., θ is fixed).

Since σ is known, (4.22) and (4.23) can be combined to give the angle of the raypath in terms of either κ or λ independently. The result is

$$\tan\theta = -\frac{(\sigma + \mathcal{U}\kappa)^2}{\sigma} \qquad \text{or} \qquad \tan\theta = -\frac{\sigma}{(1-\mathcal{U}\lambda)^2}\,. \tag{4.24}$$

1. I_1 modes

For the I_1 branch we have $\sigma = 1$ and $\lambda = m > 0$. Solving (4.24) for the horizontal and the vertical wavenumbers then gives

$$\kappa = (\sqrt{-\tan\theta} - 1)/\mathcal{U} \qquad \text{and} \qquad m = (1 - \sqrt{-1/\tan\theta})/\mathcal{U} \tag{4.25}$$

where θ must satisfy $\pi/2 < \theta < 3\pi/4$ to give both positive κ and m. Inspection of (4.25) shows that both κ and m are zero at $\theta = 3\pi/4$ and increase as θ decreases towards the vertical. Shorter horizontal waves thus have more steeply inclined raypaths and smaller vertical wavelengths (compare to Fig. 20). The largest vertical wavenumber of $m = 1/\mathcal{U}$ occurs at $\theta = \pi/2$.

As described in section D, for small and moderate values of $\mathcal{U}$ we expect I_1 to be dominated by modes with $m \sim 1$ (i.e., the R83 modes). The raypath for these R83 modes (shown by the thick dashed line in Figs. 20a,d,g,j) is computed by setting $\lambda = 1$ [or $\kappa = 1/(1-\mathcal{U})$] in (4.24). (For $\mathcal{U} > 1$ the R83 modes do not exist—since the maximum wavenumber of $m = 1/\mathcal{U}$ is less than 1—and we simply set $\theta = \pi/2$). Note that the R83 raypaths give a good sense of the maximum disturbance envelope

even for relatively large $\mathcal{U}$.

2. I_2 modes

For the I_2 branch we have $\sigma = -1$ and $\lambda = -m < 0$. Solving (4.23) for the horizontal and the vertical wavenumbers then gives

$$\kappa = (1 - \sqrt{\tan\theta})/\mathcal{U} \qquad \text{and} \qquad m = (\sqrt{1/\tan\theta} - 1)/\mathcal{U} \tag{4.26}$$

where θ must satisfy $0 < \theta < \pi/4$ to give positive κ and negative λ. Inspection of (4.26) indicates that both κ and m are zero at $\theta = \pi/4$ and increase as θ decreases. Shorter horizontal waves thus have less steep raypaths and smaller vertical wavelengths. The largest horizontal wavenumber of $\kappa = 1/\mathcal{U}$ occurs at $\theta = 0$.

As for I_1, the solution for I_2 is dominated by modes with $m \sim 1$ (i.e., the R83 modes). The raypath for these R83 modes (shown by the thick dashed line in Fig. 20b,e,h,k) is computed by setting $\lambda = -1$ [or $\kappa = 1/(1+\mathcal{U})$] in (24).

3. I_3 modes

For the I_3 branch we have $\sigma = -1$ and $\lambda = m > 0$. The horizontal and the vertical wavenumbers are then given by

$$\kappa = (\sqrt{\tan\theta} + 1)/\mathcal{U} \qquad \text{and} \qquad m = (1 + \sqrt{1/\tan\theta})/\mathcal{U} \tag{4.27}$$

where θ satisfies $0 < \theta < \pi/2$ to give both positive κ and λ. The horizontal wavenumber increases with increasing θ, with a minimum value of $\kappa = 1/\mathcal{U}$ occuring at $\theta = 0$. The vertical wavenumber decreases with θ, reaching $m = 1/\mathcal{U}$ at $\theta = \pi/2$.

Note that these results provide some insight into the differences between u and w as observed in Figs. 19 and 21. Specifically, the u field has more amplitude near $\kappa = \kappa_{\mathcal{U}}$ than does the w field [since $\partial\hat{\psi}/\partial z \to \infty$ as $\kappa \to \kappa_{\mathcal{U}}$ for I_2 and I_3—see the

appendix]. As seen in (4.26) and (4.27), for I_2 and I_3 the $\kappa \sim \kappa_U$ modes propagate close to the ground.

4. Discussion: Wave scales at large $\mathcal{U}$ and $\mathcal{U}/\mathcal{L}$

Our group velocity results suggest that when $\mathcal{U}$ and $\mathcal{U}/\mathcal{L}$ are large, the dominant spatial scales in the solution are fundamentally different from those at $\mathcal{U} = 0$. For large $\mathcal{U}$ the I_1 part of the disturbance is found mainly over the coastline (cf. Fig. 20), and the dominant vertical scale for the I_1 branch is then $1/m \sim \mathcal{U}$. In dimensional terms this translates to U/N, which is also the scale for flow past a steady, non-oscillating source—that is, for large $\mathcal{U}$ and $\mathcal{U}/\mathcal{L}$ the flow past the heating gradient dominates the diurnal oscillation. This U/N scale also describes the large κ parts of I_3, which are likewise found over the coastline.

The I_2 disturbance at large $\mathcal{U}$ is found mainly near $\theta = 0$ (cf. Fig. 20), where the dominant horizontal scale is $1/\kappa \sim \mathcal{U}$. In dimensional terms this scale is U/ω, which measures the distance traveled by a fluid particle during one oscillation cycle. The basis for this advective scale is seen most easily from (4.3). At $\theta = 0$ we have $w^* = 0$, so that (4.3) becomes

$$\frac{\partial b^*}{\partial t^*} + U\frac{\partial b^*}{\partial x^*} = Q^*$$

showing that the buoyancy is simply advected at speed U while undergoing heating and cooling by the source. The anomaly at any point downstream thus retains a memory of the heating phase present when the particle first entered the coastal zone, and the distance between relatively warm and relatively cold particles is measured by the advective distance U/ω. This U/ω scale also describes the smaller κ parts of I_3, which are likewise found near $\theta = 0$.

These scales for large $\mathcal{U}$ and $\mathcal{U}/\mathcal{L}$ are illustrated by Fig. 24, which shows the w

disturbance for varying values of $\mathcal{U}$ and $\mathcal{L}$, but with $\mathcal{U}/\mathcal{L}$ held fixed at 15. The first column of the figure shows the total fields as displayed with the standard diurnal axis scalings. The second and third columns show the $I_1 + I_2$ and I_3 decomposition as displayed on axes using the modified scales described above. As $\mathcal{U}$ increases the fields in the first column expand spatially, reflecting the $\mathcal{U}$ dependence of the dominant spatial scales. But when rescaled with the appropriate large $\mathcal{U}$ and $\mathcal{U}/\mathcal{L}$ scalings, the disturbance structure is relatively uniform (apart from small changes in I_2 as $\mathcal{U}$ becomes sufficiently large).

It is worth pointing out that the importance of I_3 (as measured by the ratio of I_3 amplitude to $I_1 + I_2$ amplitude) in Fig. 24 is essentially constant. This reinforces the notion that the relative amount of power in I_3 is determined largely by $\mathcal{U}/\mathcal{L}$ (since $\mathcal{U}/\mathcal{L}$ in the figure is fixed).

F. Summary

Building upon R83, this study has explored the linear wave response to a diurnally oscillating heating gradient in a background wind. This model can be considered a simple analog to the equatorial coastal circulation. Under a diurnal wave scaling, the wave response is a function of two control parameters: a nondimensional coastal width $\mathcal{L} = \omega L/NH$ and a nondimensional windspeed $\mathcal{U} = U/NH$.

For $\mathcal{U} \neq 0$ the Fourier integral solution consists of three distinct wave branches: I_1, I_2 and I_3. The I_1 and I_2 branches correspond directly to the two branches described by R83, except with Doppler shifting and associated tilting of the raypaths. The extent of this Doppler shifting is determined directly by $\mathcal{U}$, with larger $\mathcal{U}$ leading to greater raypath tilting and more widely dispersed wave energy.

The I_3 branch exists only for $\mathcal{U} \neq 0$ and is shown to be broadly similar to

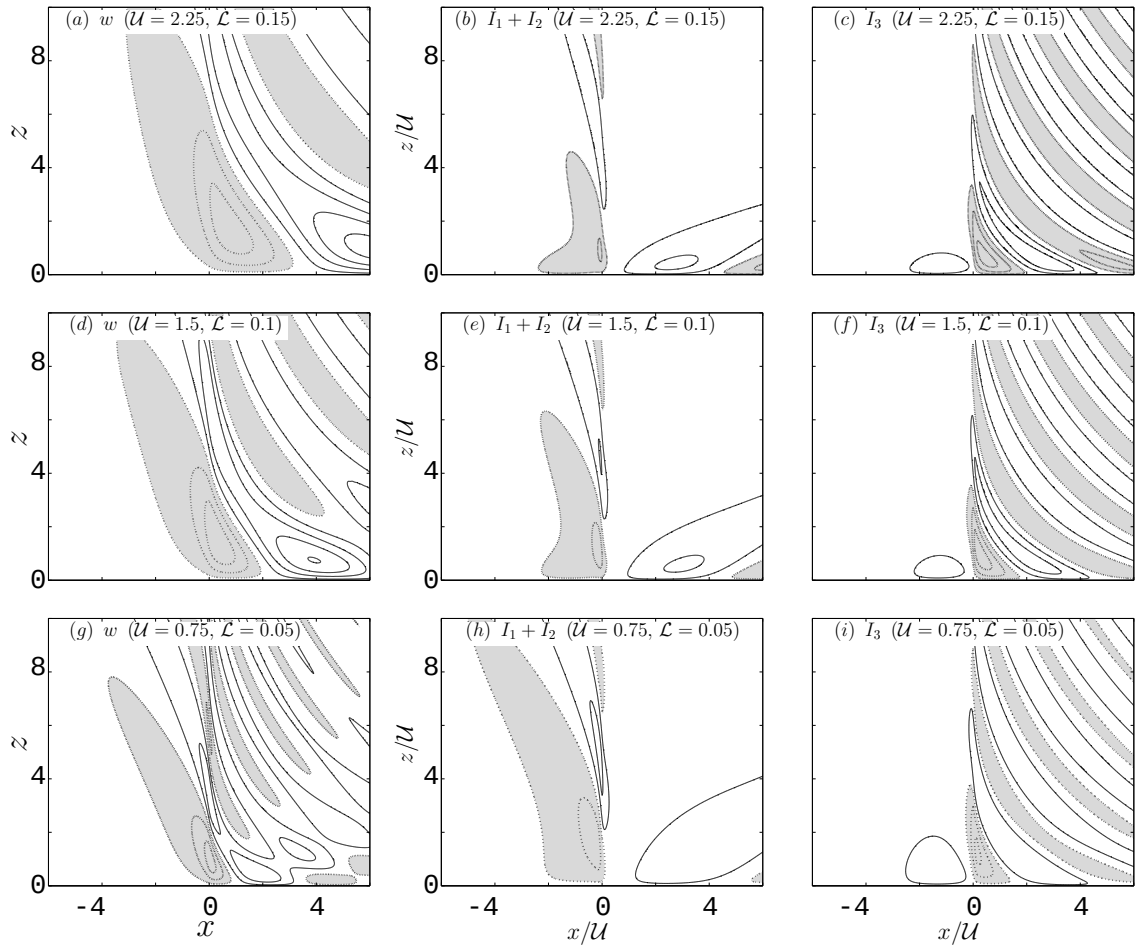

Fig. 24. Total w and decomposition into $I_1 + I_2$ and I_3 branches for fixed $\mathcal{U}/\mathcal{L} = 15$ at time $t = \pi/2$. (a) Total w, (b) $I_1 + I_2$ and (c) I_3 [c.i. $= 0.0267$] with $\mathcal{U} = 2.25$ and $\mathcal{L} = 0.15$. As in (a)–(c), but for (d)–(f) $\mathcal{U} = 1.5$ and $\mathcal{L} = 0.1$ [c.i. $= 0.04$] and (g)–(i) $\mathcal{U} = 0.75$ and $\mathcal{L} = 0.05$ [c.i. $= 0.08$]. (a), (d) and (g) use standard diurnal axis scalings, all other panels use modified large $\mathcal{U}$ and $\mathcal{U}/\mathcal{L}$ scalings. Contours vary with $1/\mathcal{L}$ to account for increased amplitude with decreasing $\mathcal{L}$.

flow past a stationary heat source or a topographic obstacle. The importance of this branch (relative to I_1 and I_2) increases as $\mathcal{U}/\mathcal{L}$ increases, with the amplitude becoming similar to the other two branches once $\mathcal{U}/\mathcal{L} \sim 2$. For typical dimensional parameters (such as those given in section C3), a characteristic threshold wind for the importance of the I_3 mode is roughly $U \sim 1.5$ m/s (with smaller L implying smaller thresholds). For still larger $\mathcal{U}/\mathcal{L}$, the I_3 branch becomes the dominant part of the solution.

The spatial scales present in all three branches can be explained reasonably well using group velocity arguments. At large $\mathcal{U}$ and $\mathcal{U}/\mathcal{L}$, the dominant scales are fundamentally different from the $\mathcal{U} = 0$ case.

It should be emphasized that we do not expect our simple linear theory to provide an accurate description of the sea breeze in its entirety. Most notably, the model completely misses the low-level sea-breeze front and the associated density current. However, it is reasonable to expect that the model provides some insight into the larger-scale wave response associated with the sea breeze. Such waves are difficult to observe directly but have been noted in some recent real-world modeling studies (e.g., [42]). There has also been speculation that such coastally generated gravity waves are involved in the observed diurnal propagation of convection off tropical coastlines ([41] ; [40],among others). At the very least, the current study provides a simple conceptual reference point for the study of these waves.

G. Appendix: Computational Methods for I_2 and I_3

As noted in section C1, the integrals I_2 and I_3 in (4.20) and (4.21) feature rapid oscillations in the integrands near $\kappa = \kappa_{\mathcal{U}}$. These oscillations lead to poor numerical resolution near the singularity, which in turn compromises the accuracy of the quadra-

ture. The problem is particularly acute for $u = \partial\psi/\partial z$, since for u the amplitude is singular as well as the phase.

To address this problem we use a method first introduced by [102] in the context of rotating flow past topography. Details of the method are given in section 2 below. However, we begin by briefly describing the more conventional methods used for I_1.

1. Computation of I_1

Inspection of (4.19) shows that the integrand is well-behaved for all $\kappa > 0$, and computation of the integral is therefore straightforward. In the present study we use the substitution $\kappa = \kappa_1(1/s-1)$ to map the indefinite interval $0 \le \kappa < \infty$ to the finite range $0 < s \le 1$. A quadrature using the trapezoidal rule is applied using a uniform discretization in s. Varying the parameter κ_1 shifts the point density to smaller or larger κ, with half the total points at $\kappa < \kappa_1$ and half at larger κ. The choice $\kappa_1 = 5$ was found to give reasonable results with modest effort.

2. Desingularization for I_2 and I_3

To account for the singularities in I_2 and I_3, we use two approaches in combination. First we identify an integrable function whose behavior at the singular point matches that of the function to be integrated. Subtracting this matching function from the integrand then effectively damps the singularity. The second step is to then stretch the remaining singular oscillation using an appropriate coordinate mapping.

To illustrate, we consider our most singular case, specifically the I_3 contribution to the horizontal velocity u. Taking a vertical derivative of (4.21) gives

$$\frac{\partial I_3}{\partial z} = -\frac{1}{2}\int_{\kappa\mathcal{U}}^{\infty} \frac{e^{-\kappa\mathcal{L}}}{\kappa^2 + (\mathcal{U}\kappa - 1)^2} e^{i(\kappa x - t)} (im\, e^{imz} + e^{-z})\, d\kappa \tag{4.28}$$

where $m = \kappa/(\mathcal{U}\kappa - 1)$. The second term in the last parentheses is well-behaved, but

the $im\,e^{imz}$ term has both phase and amplitude singularities as $\kappa \to \kappa_{\mathcal{U}}^{+}$.

To transform to a finite range we use the trigonometric substitution

$$\kappa = \kappa_{\mathcal{U}}\,\frac{1}{1-\sin\theta}$$

which maps (4.28) to

$$\frac{\partial I_3}{\partial z} = -\frac{1}{2\kappa_{\mathcal{U}}}\int_0^{\pi/2} C_3(\theta)\,e^{-z}\cos\theta\,d\theta - \frac{i}{2}\int_0^{\pi/2} C_3(\theta)\exp(i\kappa_{\mathcal{U}} z\csc\theta)\cot\theta\,d\theta \quad (4.29)$$

where

$$C_3(\theta) = \frac{\kappa^2\,e^{-\kappa\mathcal{L}}}{\kappa^2+(\mathcal{U}\kappa-1)^2}\,e^{i(\kappa x-t)}$$

is a well-behaved amplitude factor. The first integral in (4.29) can be directly discretized without problems. However, the second integral inherets the original phase and amplitude singularities as $\theta \to 0^{+}$.

To remove these singularities, we note that sufficiently near the singular point the integrand in (4.29) matches that of a tabulated integral, specifically the exponential integral E_1 (e.g., [103], section 5.1). That is, with a change of variable [102] the exponential integral can be written for $\mathrm{Re}(\xi) \geq 0$ as

$$E_1(\xi) = \int_0^{\pi/2} \exp(-\xi\csc\theta)\cot\theta\,d\theta \quad (4.30)$$

which for imaginary ξ has the same singular phase and amplitude behavior as (4.29). Combining (4.29) with (4.30) then gives

$$\begin{aligned}\frac{\partial I_3}{\partial z} = &-\frac{1}{2\kappa_{\mathcal{U}}}\int_0^{\pi/2} C_3(\theta)\,e^{-z}\cos\theta\,d\theta \\ &-\frac{i}{2}\int_0^{\pi/2} A_3(\theta)\,\exp(i\kappa_{\mathcal{U}} z\csc\theta)\cot\theta\,d\theta \\ &-\frac{i}{2}\,C_3(0)\,E_1(-i\kappa_{\mathcal{U}} z)\end{aligned} \quad (4.31)$$

where the difference amplitude

$$A_3(\theta) = C_3(\theta) - C_3(0)$$

now has a first-order zero at $\theta = 0^+$ so that $A_3(\theta)\cot\theta$ remains finite.

Because of the $\cot\theta$ term (4.29), the subtraction step in (4.31) damps the amplitude singularity but leaves a finite-amplitude singular oscillation. To regularize this oscillation we apply a second coordinate mapping

$$\theta = \frac{\pi}{2}\, s^{\alpha} \tag{4.32}$$

with s ranging from 0 to 1. Setting $\alpha > 1$ causes the singular oscillation near $\theta = 0^+$ to be stretched, in the sense that $d\theta = \alpha(\pi/2)s^{\alpha-1}ds \to 0$ as $s \to 0$. The resulting integrand for $0 \le s \le 1$ then has an order $\alpha - 1$ zero at the singular endpoint.

Finally, the desingularized integral (4.31) with (4.32) is computed with a trapezoidal quadrature using a uniform discretization in s. Similar methods are used to compute the I_2 integral for u as well as the w integrals (which are one order less singular in amplitude and thus easier to compute).

3. An example

Figure 25 shows an example calculation for the case $\mathcal{U} = 0.625$ with $\mathcal{L} = 0.1$. Shown in Fig. 25a is a direct quadrature of (4.29)—that is, without the subtraction step in (4.31) and with $\alpha = 1$ in (4.32)—using a uniform discretization of $ns = 2000$ points. The analogous desingularized quadrature of (4.31) with $\alpha = 3$ and $ns = 2000$ is shown in Fig. 25b. As can be seen, the direct trapezoidal quadrature of (4.29) features significant numerical artifacts due to the singular nature of the integrand. By contrast, in the desingularized case these artifacts are effectively removed.

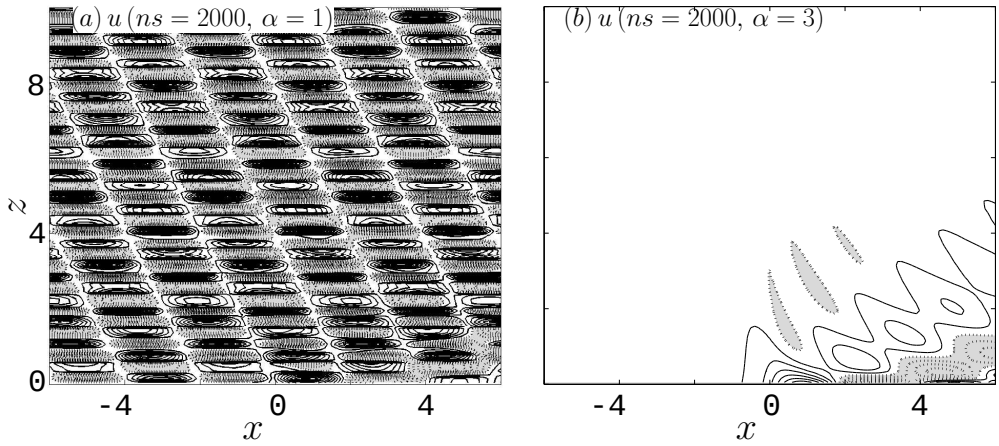

Fig. 25. Horizontal velocity u with $\mathcal{U} = 0.625$ and $\mathcal{L} = 0.1$ at time $t = \pi/2$. (a) Direct quadrature of (4.29) with 2000 points and $\alpha = 1$. (b) Desingularized quadrature of (4.31) with 2000 points and $\alpha = 3$.

CHAPTER V

THE WAVE RESPONSE TO TERRAIN AND NONLINEARITY

A. Introduction

The previous chapter explored coastal wave dynamics for the case of a flat lower boundary and for a linearized disturbance. In the present chapter we extend this analysis in two ways: (i) the role of terrain is addressed by adding topography to the linear problem; and (ii) nonlinear effects are explored through nonlinear model calculations.

As discussed in chapter III A3, observational studies show that offshore convection in coastal regions is often tied to the presence of coastal topography. To begin addressing this issue, we start by adding topography to the linear wave problem of chapter IV. In the linear problem, the terrain is expected to have three effects on the disturbance flow: (i) additional interior wave generation due to elevated heating gradients along the terrain slopes; (ii) boundary wave generation due to the disturbance flow passing over the sloped boundary; and (iii) wave-wave interactions between the linear sea-breeze response and the background mountain wave. Our first goal in this chapter is to explore the relative importance of these three effects.

The linear problems described above provide a useful starting point for understanding the basic wave dynamics, particularly for small topography. However, the real problem to be considered is strongly nonlinear. As a first step towards addressing this issue, we explore several examples of the nonlinear behavior of the system by varying the heating amplitude in the context of the nonlinear model described in chapter II. Exploring the changes in the nonlinear solution as the heat source increases is our second goal in this chapter.

The first part of the chapter focuses on the linear problem. The following section describes the physical context for the linear study and provides an overview of the associated numerical model and experimental design. Section C examines the role of terrain in the linear wave response. The three terrain effects described above are computed through Taylor expansions in small mountain height.

The second part of the chapter discusses the nonlinear problem. Section D takes a look at some examples of nonlinear phenomena for both zero and non-zero background wind, and for a range of mountain heights. A summary will be given in the last section.

B. Basic Physics and Computational Methods

1. Linear problem formulation

The problem of flow past coastal terrain has two potential wave sources: (i) the background flow past the topography; and (ii) the heating gradients due to the coastline and the terrain. Here our interest is the second source. To isolate this source, we take a steady nonlinear mountain wave as our background state (as computed through a nonlinear model run) and then consider the linear disturbance produced when a heat source is added to the problem.

The basic physical formulation of the problem is same as in chapter IV except for two differences: (i) terrain is added to the lower boundary; and (ii) instead of the constant background wind, the steady mountain wave is used as the background state. To define notation, we divide the total background mountain wave into a constant upstream wind speed U and a nonlinear wave disturbance u_0, w_0, etc.. The disturbance linear response to the heat source is then denoted by u', w', etc., so that the total wind in the x direction (for example) is $u = U + u_0 + u'$. Linearizing the 2D compressible Boussinesq system about the steady mountain wave then gives the

disturbance system

$$\frac{\partial u'}{\partial t} + U\frac{\partial u'}{\partial x} + u_0\frac{\partial u'}{\partial x} + w_0\frac{\partial u'}{\partial z} + u'\frac{\partial u_0}{\partial x} + w'\frac{\partial u_0}{\partial z} = -\frac{\partial P'}{\partial x}, \tag{5.1}$$

$$\frac{\partial w'}{\partial t} + U\frac{\partial w'}{\partial x} + u_0\frac{\partial w'}{\partial x} + w_0\frac{\partial w'}{\partial z} + u'\frac{\partial w_0}{\partial x} + w'\frac{\partial w_0}{\partial z} = -\frac{\partial P'}{\partial z} + b', \tag{5.2}$$

$$\frac{\partial b'}{\partial t} + U\frac{\partial b'}{\partial x} + u_0\frac{\partial b'}{\partial x} + w_0\frac{\partial b'}{\partial z} + u'\frac{\partial b_0}{\partial x} + w'\frac{\partial b_0}{\partial z} + N^2 w' = Q, \tag{5.3}$$

$$\frac{\partial P'}{\partial t} + c_s^2\left(\frac{\partial u'}{\partial x} + \frac{\partial w'}{\partial z}\right) = 0, \tag{5.4}$$

with

$$w' = u'\frac{\partial h}{\partial x} \qquad \text{at} \qquad z = h(x). \tag{5.5}$$

The terrain shape is a plateau with steep sides, with length scales modeled roughly on the equatorial Andes. The shape of the topography is described by the smooth 2D plateau profile

$$h(x') = \begin{cases} \frac{h_0}{16}\left[1 + \cos\left(\frac{\pi x'}{4L_s}\right)\right]^4, & \text{for } L_p \le |\, x' \,| \le L_p + 4L_s; \\ h_0, & \text{for } |\, x' \,| < L_p; \\ 0, & \text{otherwise,} \end{cases} \tag{5.6}$$

where L_p corresponds to the half width of the flat part of the plateau, and L_s is roughly half width of the slope of the plateau. Here we set the two slopes to be symmetric. The variable x' in (5.6) is defined to be the distance as measured from the center of the plateau. If the coastline is located at $x = 0$ and the distance from the coastline to the point where $h(x)$ first reaches its maximum height is L_c, then

$$x' = x - (L_c + L_p/2). \tag{5.7}$$

The diabatic oscillating heat source Q is defined by [c.f. (4.5)]

$$Q(x, z, t) = \frac{1}{\pi}\left(\frac{\pi}{2} + \tan^{-1}\frac{x}{L}\right)\exp(-\frac{z-h}{H})\cos(\omega t). \tag{5.8}$$

Different from the heating profile used in chapter IV, this definition of the heat source includes the elevated heating gradient associated with the topography. As mentioned above, the center of the coastal zone is taken to be $x = 0$.

The disturbance is scaled using the diurnal scaling factors described in chapter IV, section B1. As before, the nondimensional control parameters then include the nondimensional background wind speed $\mathcal{U} = U/NH$, the nondimensional half width of the coastal zone $\mathcal{L} = \omega L/NH$ and the nondimensional dynamical aspect ratio $\delta = \omega/N$. The use of a compressible pressure equation (5.4) introduces a Mach number $Ma = NH/c_s$. When terrain is added, four additional parameters are introduced: the nondimensional terrain height $\mathcal{H} = h_0/H$, the nondimensional half width of the slope $\mathcal{L}_s = \omega L_s/NH$, the nondimensional half with of the plateau $\mathcal{L}_p = \omega L_p/NH$, and the nondimensional distance between the coastline and the topography $\mathcal{L}_c = \omega L_c/NH$. To simplify the parameter space, only the parameters $\mathcal{U}$ and $\mathcal{H}$ will be varied in our calculations. The remaining parameters are held fixed with $\mathcal{L} = 0.0909$, $\delta = 0.0073$, $Ma = 0.0267$, $\mathcal{L}_s = 0.1364$, $\mathcal{L}_p = 1.364$, $\mathcal{L}_c = 2.182$. Dimensional values for the parameters are given below.

The eight parameters given above completely describe the disturbance parameter space. However, for cases with background wind it is also useful to indicate the mountain-wave parameters as defined in chapter II. Thus for $U \neq 0$ we give the mountain height in terms of both h_0/H and Nh_0/U.

2. Computational method

With the terrain added, the linear problem can no longer be addressed analytically because of the non-constant coefficients in (5.1)-(5.5). To overcome this problem, we use a linearized numerical model to compute the solutions.

The computation methodology involves two steps. First, using a nonlinear model,

the mountain wave problem is computed without the heat source until a steady state mountain wave is achieved. A second simulation is then computed in which the model is linearized about the steady state mountain wave from the first model run. The oscillating heat source is added and the linear model is run until a steady oscillation is achieved. In this way, we can separate the disturbance due to the specified heating from the background mountain wave.

The linear simulations are calculated using a linearized version of the nonhydrostatic, compressible Boussinesq model described in chapter II. The lateral boundary condition is realized through the damping layer. Both a damping layer and the radiation condition are applied at the upper boundary. Terrain is included by use of the terrain-following vertical coordinate (2.13), which in the linearized problem implies the boundary condtion (5.5).

The 2D calculations are computed in a domain with horizontal extent $300L$ and depth $18.75H$. The damping layers are imposed for the outer $48L$ of the domain in x and the upper $8.75H$ in z. The horizontal grid spacing is $\triangle x = 0.2L$. The vertical grid spacing is $\triangle z = 0.05H$ with vertical stretching factor of 1.005. Such small vertical grid spacing is needed to fully resolve the disturbance raypaths for $U = 0$ and to resolve the flow near the ground for $U \neq 0$. In dimensional terms, $L = 10$km, $H = 800$m, $N = 0.01$ s^{-1}, $\triangle x = 2$km and $\triangle z = 40$m. The terrain parameters are given by $L_s = 15$km, $L_p = 150$km and $L_c = 90$km.

3. Verification

The linear model was verified by comparison to the theoretical solution described in chapter IV. Figures 26 and 27 show the vertical velocity and the horizontal velocity obtained from the analytical calculation and from the linear numerical model at cycle time $\omega t = \pi/2$. It is clear that the model simulation matches the theory calcuations

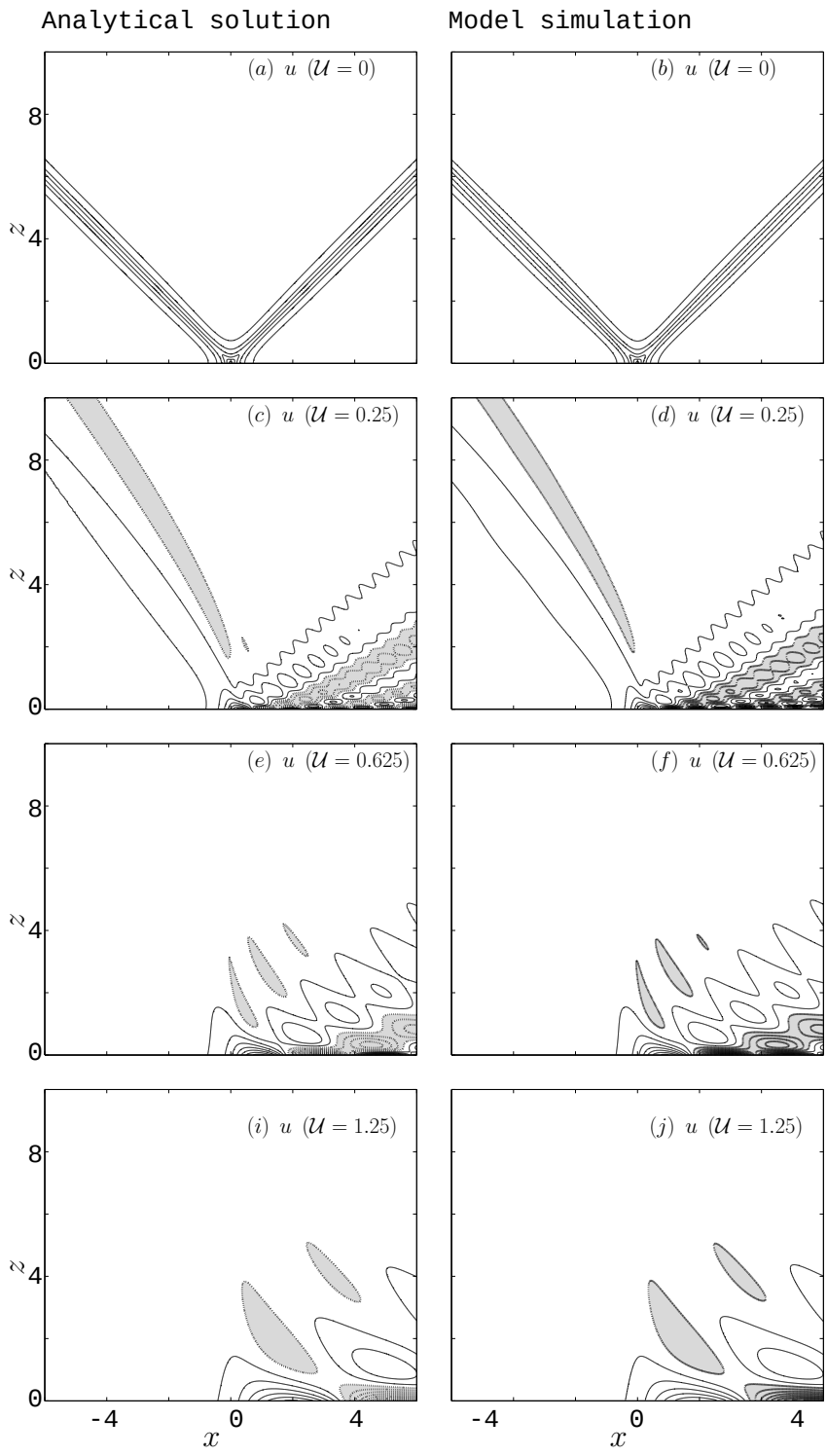

Fig. 26. The comparison of the horizontal velocity with the different background wind $\mathcal{U}$ at $\pi/2$ day between the analytical calculation results and the linear numerical results.

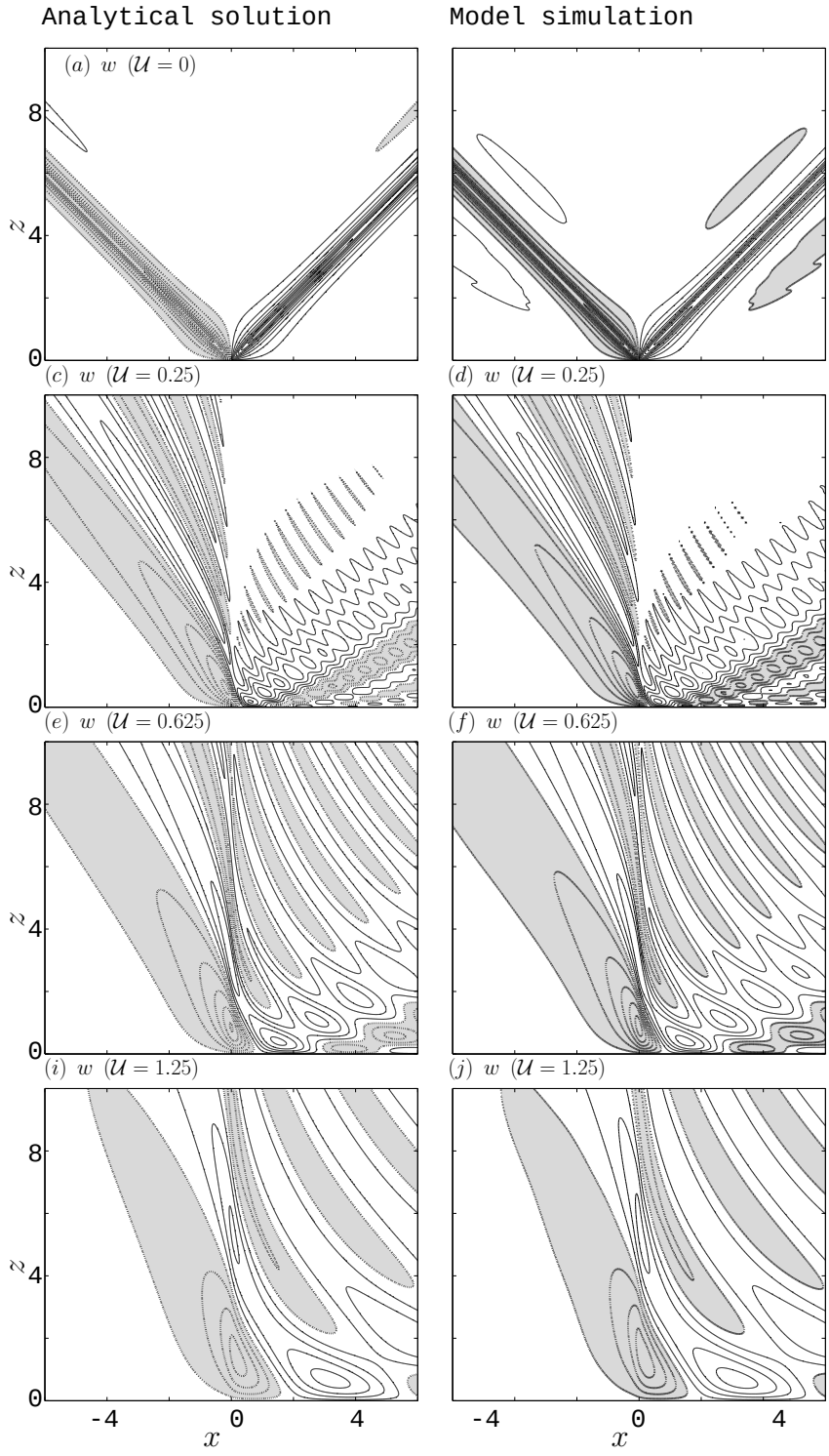

Fig. 27. The comparison of the vertical velocity with the different background wind $\mathcal{U}$ at $\pi/2$ day between the analytical calculation results and the linear numerical results.

very well. This reliable linear model can be used as a replacement for linear theory when more complicated studies of the sea breeze are investigated.

C. Linear Wave Response to Small Topography

The linear behavior of the wave response to small topography is explored in this section. Our main interest in this part is to explore the relative importance of the three effects of topography mentioned in section A.

1. Resting background state

For $\mathcal{U} = 0$ only two of the mountain effects are non-zero: the elevated heating gradients and the disturbance sea breeze flow past the topography slopes. Figure 28 shows the linear wave response for the case $\mathcal{U} = 0$ and for topgraphy heights $\mathcal{H} = 0.0625$, $\mathcal{H} = 0.125$ and $\mathcal{H} = 0.625$. At small topography height the disturbances are dominated by the sea breeze solution discribed by R83, but there are also small additional disturbances excited over the plateau slopes (Fig. 28a). The amplitude of this additional disturbance increases with topography height (Fig. 28b). When topography height is $\mathcal{H} = 0.625$, the additional disturbance becomes the same order as the sea breeze wave disturbanc (Fig. 28c).

Figure 29 shows the solution for the same mountain heights but with no coastline, that is with the heat source (5.8) replaced by

$$Q(x, z, t) = \exp(-\frac{z - h}{H}) \cos(\omega t). \tag{5.9}$$

With no coastline the sea breeze disturbance disappears and the only wave source is then the elevated heating gradients. Figs. 29a and b show that the elevated heating gradients produce disturbances over both slopes, with the amplitude of the

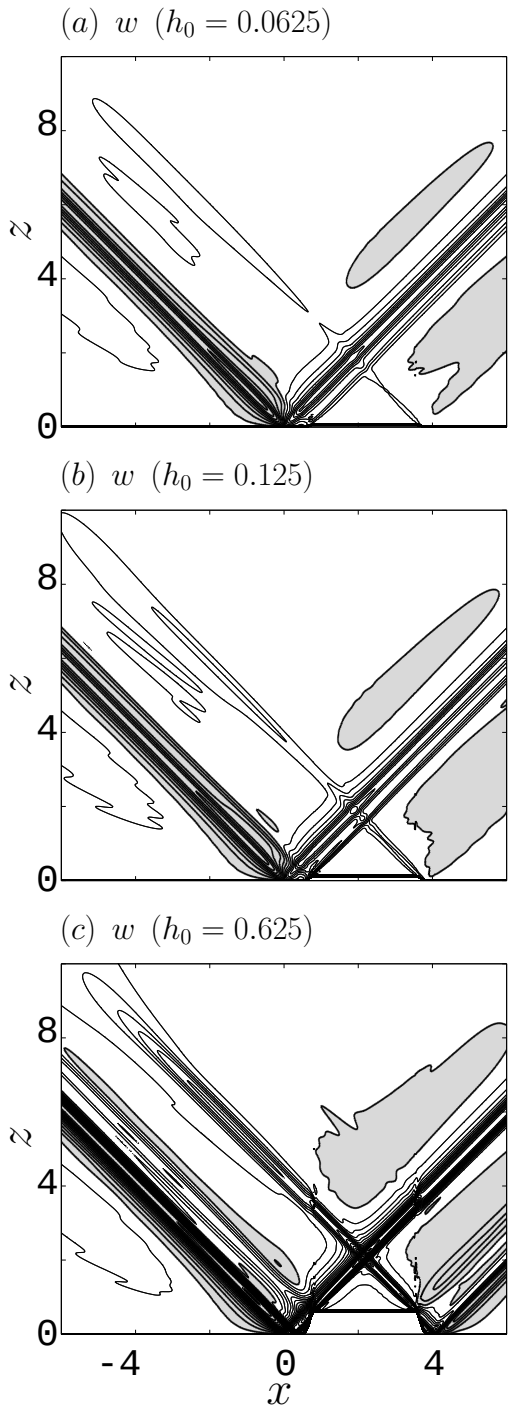

Fig. 28. Vertical velocity response to the diurnal heating at $t = \pi/2$. Terrain height $h_0$is (a) 0.0625, (b) 0.125 and (c) 0.625.

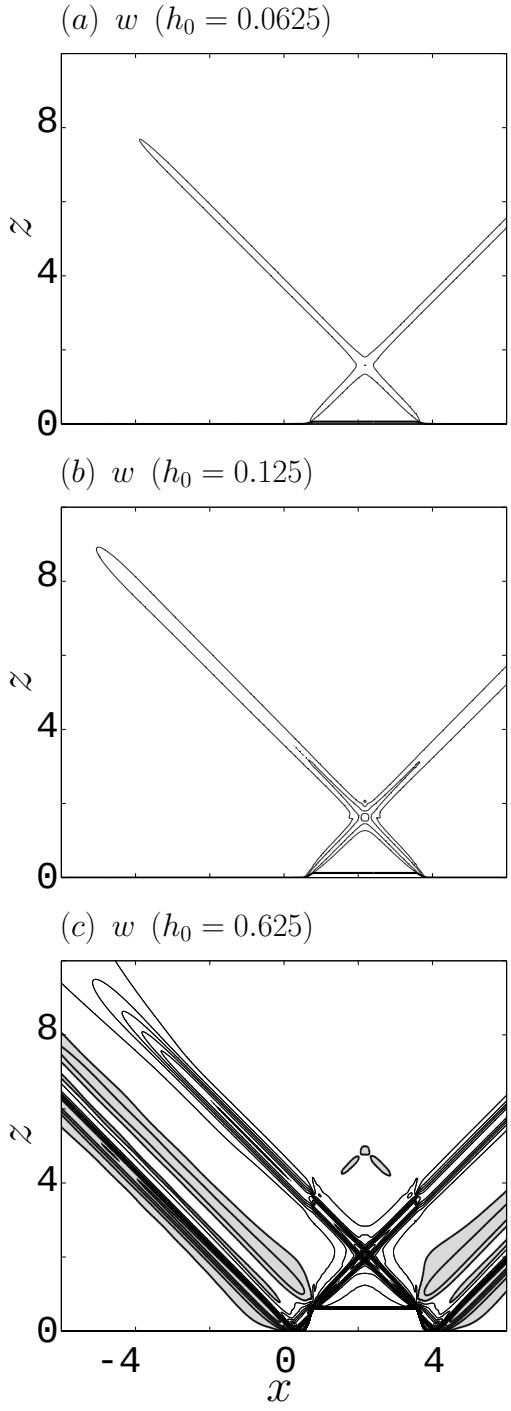

Fig. 29. Vertical velocity response to the diurnal heating at $t = \pi/2$. Coastline is not included. Vertical velocity response to the diurnal heating at $t = \pi/2$. Terrain height $h_0$is (a) 0.0625, (b) 0.125 and (c) 0.625.

disturbance similar to that in Fig. 28 except for Fig. 29c (in which the new branch in Fig. 29c is apparently due to the wave reflection). This suggests that the elevated heating source is the dominant terrain effect for $\mathcal{U} = 0$. As in Fig 28 the amplitude of the response increases with the terrain height.

Note that the maximum w disturbance occurs where the disturbance raypaths intersect over the plateau. We revisit this point in section D.

2. Mountain-wave background state

Figure 30 shows the linear disturbance produced by the heat source for the case $\mathcal{U} = 0.625$. Figure 30a shows the sea breeze disturbance without topography. Figure 30b shows the case with $\mathcal{H} = 0.0625$ (or $Nh_0/U = 0.1$) and indicates that the effect of the terrain is to introduce wave disturbances over the two slopes of the plateau. Fig. 30c shows these disturbances with no coastline. As before, this indicates the wave generation by the elevated heating gradients in the absence of the sea breeze. Comparing Fig. 30b and c shows that the disturbance excited by the elevated heating is relatively small in this case. The disturbance produced by the other two topography effects will be diagnosed in the following section.

Calculations with larger mountain heights suggest that the disturbance becomes unstable once the mountain height reaches some critical value. The form of the instability is similar to the instability seen in the mountain-wave problem described by [104]. This suggests the instablity is likely to be caused by the triad interaction.

3. Diagnostic calculations

Figure 30 shows that the main effect of the terrain in the calculations with the background wind is to introduce additional wave disturbances over the topographic slopes. The present section explores the forcing mechanism that produces these slope distur-

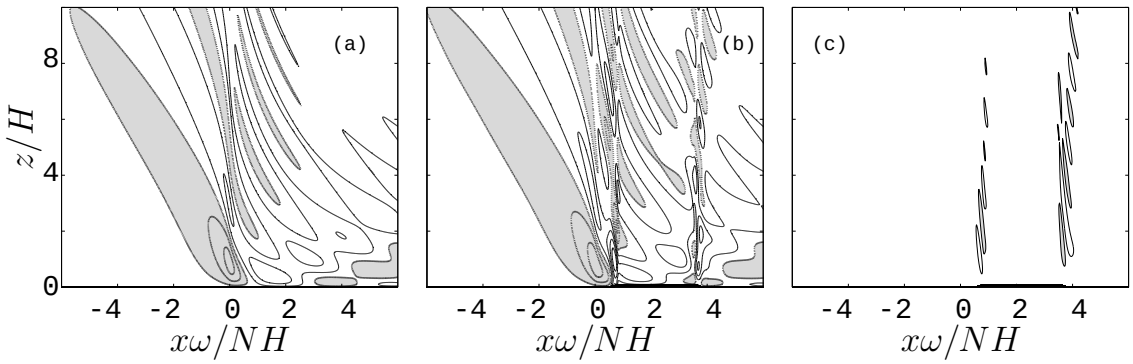

Fig. 30. Vertical velocity with background wind $\mathcal{U} = 0.625$ at $t = \pi/2$. Vertical velocity [c.i. = 0.08] in case with (a) no terrain; (b) $h_0 = 0.0625$ and coastline included; (c) $h_0 = 0.0625$ and coastline excluded.

bances.

As pointed out previously, in the basic equations (5.1)-(5.8) there are three modifications due to the imposed topography: the elevated heat gradients (included in the heating profile Q), the disturbance flow over the slopes (included in the lower boundary condition) and the interaction with the background mountain wave (included in the advection terms). In general, these three effects are interconnected– for example, the flow produced by the elevated heating will in principle produce a disturbance flow over the sloped boundary. However, as shown below, for small terrain heights the three effects can be cleanly separated.

To begin, assume small terrain height h and expand the disturbance fields in powers of h as

$$u' = u^{(0)} + u^{(1)} + ..., \qquad w' = w^{(0)} + w^{(1)} + ...,$$

$$b' = b^{(0)} + b^{(1)} + ..., \qquad P' = P^{(0)} + P^{(1)} + ...,$$

$$Q = Q^{(0)} + Q^{(1)} + ...$$

where $u^{(0)} \sim O(0)$, $u^{(1)} \sim O(h)$, $u^{(2)} \sim O(h^2)$, etc. Here the forcing terms are derived

from the Taylor series expansion as

$$Q^{(0)} = \frac{Q_0}{\pi}\left(\frac{\pi}{2} + \tan^{-1}\frac{x}{L}\right)\exp\left(-\frac{z}{H}\right)\cos(\omega t), \tag{5.10}$$

and

$$Q^{(1)} = \frac{Q_0 h}{\pi H}\left(\frac{\pi}{2} + \tan^{-1}\frac{x}{L}\right)\exp(-z/H)\cos(\omega t). \tag{5.11}$$

The background mountain wave also depends on h and is expanded as

$$u_0 = u_0^{(1)} + u_0^{(2)} + ..., \qquad w_0 = w_0^{(1)} + w_0^{(2)} + ..., \qquad b_0 = b_0^{(1)} + b_0^{(2)} + ...$$

where it should be noted that the zero-order terms for the mountain wave are zero. In the present context these background terms are assumed to be known.

Then we substitute the above expressions into the basic equations. For small h, the zero-order system is

$$\frac{\partial u^{(0)}}{\partial t} + U\frac{\partial u^{(0)}}{\partial x} + \frac{\partial P^{(0)}}{\partial x} = 0, \tag{5.12}$$

$$\frac{\partial P^{(0)}}{\partial z} - b^{(0)} = 0, \tag{5.13}$$

$$\frac{\partial b^{(0)}}{\partial t} + U\frac{\partial b^{(0)}}{\partial x} + N^2 w^{(0)} = Q^{(0)}, \tag{5.14}$$

$$\frac{\partial u^{(0)}}{\partial x} + \frac{\partial w^{(0)}}{\partial z} = 0 \tag{5.15}$$

with

$$w^{(0)}(z = 0) = 0. \tag{5.16}$$

The solution to (5.12)-(5.16) are the linear sea-breeze solutions described in chapter

IV. The first order system (in h) is then

$$\frac{\partial u^{(1)}}{\partial t} + U\frac{\partial u^{(1)}}{\partial x} + \frac{\partial P^{(1)}}{\partial x} = -u_0^{(1)}\frac{\partial u^{(0)}}{\partial x} - w_0^{(1)}\frac{\partial u^{(0)}}{\partial z} - u^{(0)}\frac{\partial u_0^{(1)}}{\partial x} - w^{(0)}\frac{\partial u_0^{(1)}}{\partial z}, \tag{5.17}$$

$$\frac{\partial}{\partial x}P^{(1)} - b^{(1)} = 0, \tag{5.18}$$

$$\frac{\partial b^{(1)}}{\partial t} + U\frac{\partial b^{(1)}}{\partial x} + N^2 w^{(1)} = -u_0^{(1)}\frac{\partial b^{(0)}}{\partial x} - w_0^{(1)}\frac{\partial b^{(0)}}{\partial z} - u^{(0)}\frac{\partial b_0^{(1)}}{\partial x} - w^{(0)}\frac{\partial b_0^{(1)}}{\partial z} + Q^{(1)}, \tag{5.19}$$

$$\frac{\partial u^{(1)}}{\partial x} + \frac{\partial w^{(1)}}{\partial z} = 0 \tag{5.20}$$

with

$$w^{(1)} = u^{(0)}\frac{\partial h}{\partial x} \qquad \text{at} \qquad z = 0 \tag{5.21}$$

For small terrain height the system (5.17)-(5.21) describes the leading-order effects of the terrain.

The system (5.17)-(5.21) shows that at leading order the three terrain effects mentioned in section A can be cleanly seperated: (i) the elevated heating gradients are described by $Q^{(1)}$ term in (5.19); (ii) the sea-breeze flow past the terrain slopes is described by (5.21); and (iii) the interaction between the sea breeze and the background mountain wave is described by the advection terms on the right in (5.17) and (5.19). Since the system is linear, the response to these three forcing terms can be computed independently.

Solutions to the first-order system (5.17)-(5.21) are computed using a modified version of the linear model described previously. The model assumes a flat lower boundary but allows w to be specified at the boundary according to (5.21). For simplicity of coding, the calculations were implemented using a hydrostatic version of the model.

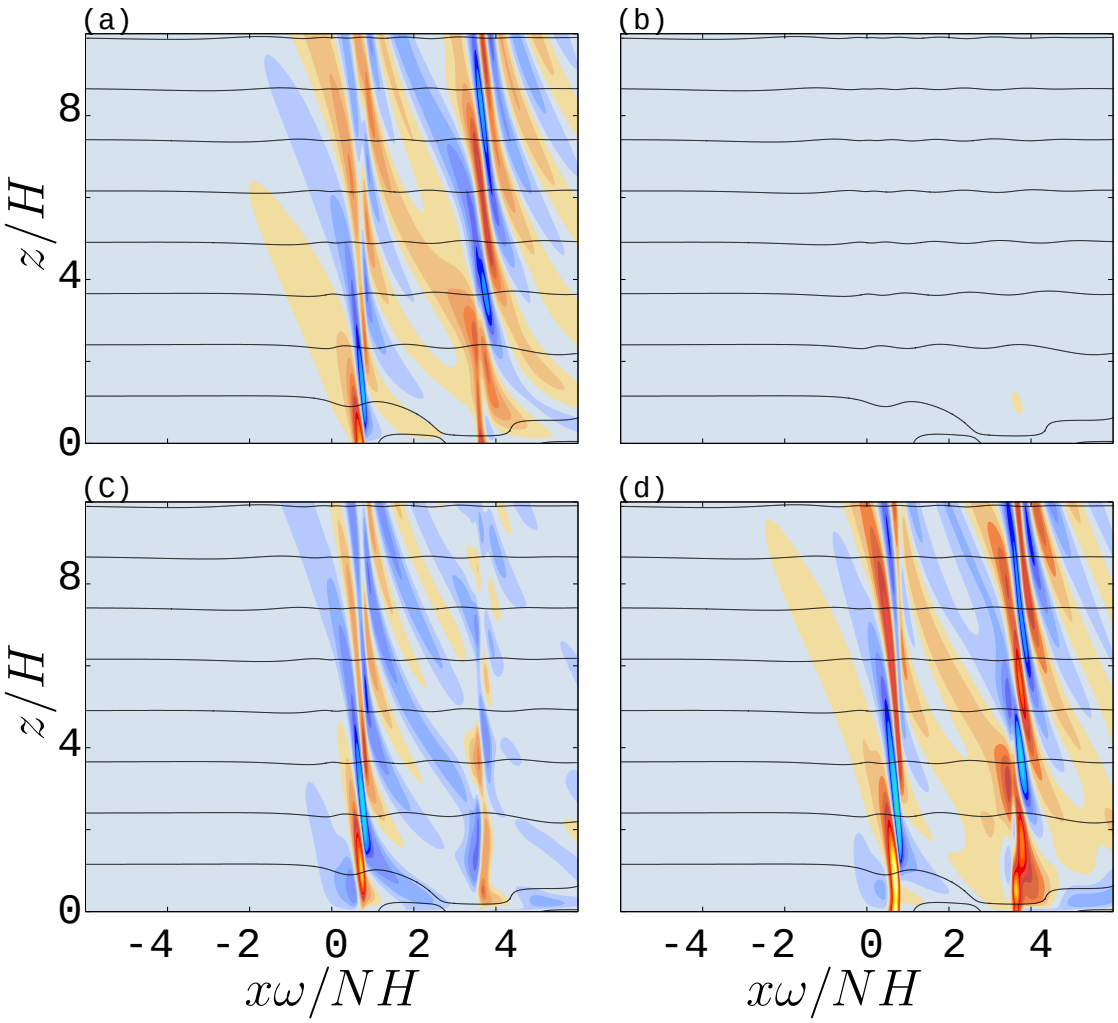

Fig. 31. Three effects of topography for cases with background wind $\mathcal{U} = .625$ and $\mathcal{H} = 0.0031$ at $t = \pi/2$. Vertical velocity [c.i. $= 5e - 5$m/s] due to (a) the disturbance flow over slope (b) the elevated temperature gradient, (c) the wave-wave interaction between sea breeze and mountain wave, (d) the total disturbuance.

Figure 31 displays the three separate effects of topography at leading order. The effects of (i) the sea breeze flow over the slopes (Fig. 31a) and (iii) the interaction between sea-breeze and mountain wave (Fig. 31c) are similar in size. The effect of the elevated heating gradient is found to be negligible in this case.

D. Nonlinear Phenomena

The calculations described above give some insight into the effects of terrain on the sea breeze as considered in the linear context. However, the real problem is strongly nonlinear. In this section we consider several examples of the nonlinear behavior of the sea breeze wave response by computing numerical simulations with varying interior heating amplitude. Note that the results in this section are work in progress and thus should probably be considered preliminary.

1. Basic physics and computational methods for nonlinear calculations

The simulations in this section are computed using the nonlinear compressible Boussinesq model described in chapter II. For the present simulations the model is modified in two ways: (i) interior heating source described in (5.8) is added to the domain; and (ii) instead of bell-shaped topography, the plateau described in (5.6) is added to the lower boundary. The positions and parameters for the coastline and terrain are the same as in section B1.

The scalings for the nonlinear problem are the same for the linear problem in section B1. The use of the nonlinearity model introduces two additional control parameters: a Reynolds number for nonlinear mountain wave $Re = U^3/\kappa N^2 L$ and the nondimensional heating amplitude $\epsilon = Q_0/N^2\omega H$. In our nonlinear calculations there are thus three parameters that will be varied: $\mathcal{U}$, $\mathcal{H}$ and ϵ. The rest of the

parameters are held fixed as in last section and the Reynolds number is set to be $Re = 125$.

As in the previous work, we briefly check the reliablity of the nonlinear model by comparing to the linear problem when the heating amplitude is very small. The comparison between Figs. 32, 26 and 27 shows that the nonlinear model reproduces the linear results when the small heating is applied.

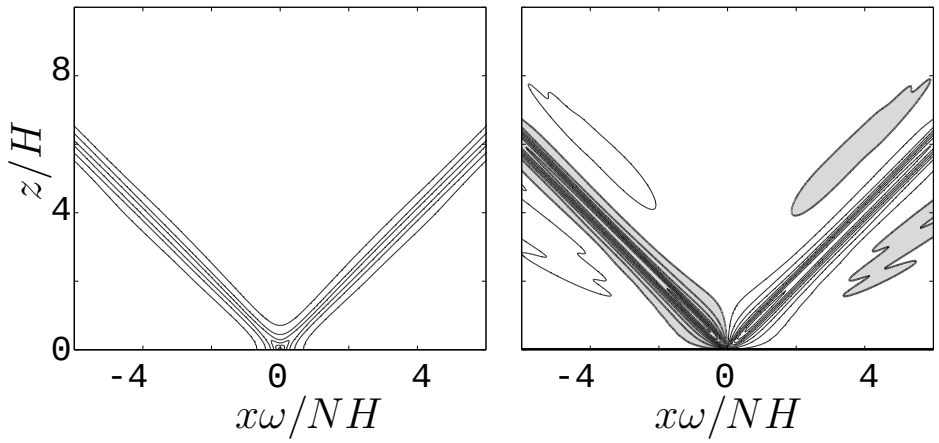

Fig. 32. (a) Horizontal and (b) vertical velocity without background wind at cycle time $\omega t = \pi/2$ for $\epsilon = 0.001$ and $\mathcal{U} = 0$ and $\mathcal{H} = 0$.

2. Resting background state

Figure 33 shows the transition of the system from linear to nonlinear for $U = 0$ and varying mountain height cases. The first column revisits the results in [105]. As expected, for small ϵ the solutions are similar to the linear theory calculations. However, with increasing heating amplitude the nonlinear factor introduces fronts to both left and right sea breeze branches. For the leftward propagating front, the intensity and propagation speed increase strongly with heating amplitude, with only a weaker secondary dependence on the terrain height. At the larger terrain heights, the

rightward propagating front becomes distorted. Note that the raypath intersection over the plateau seen in the linear solutions is found to trigger convetive overturning when the heating amplitude is large enough.

Figure 34 shows the time evolution of the system with $\epsilon = 1.5$ and no terrain. For the resting background case, the fronts form near the ends of the heating and cooling cycles and propogate onshore and offshore.

3. Flows with background wind

For the no-terrain cases, adding the background wind $\mathcal{U} = 0.625$ leads to significant differences from $\mathcal{U} = 0$ solution due to the Doppler-shifting of the wave modes. As shown in the first column in figure 35, the leftward propagating branch of the linear sea breeze remains essentially unchanged with heating amplitude when the terrain is flat. However, when terrain is added an upstream propagating front is formed and the sea breeze pattern is distorted. As with the $\mathcal{U} = 0$ case, the intensity and propagation speed of the front depends largely on the heating amplitude. The time evolution of the system both with and without terrain is illustrated in Figs. 36 and 37.

The intensity and position of the front versus the heating amplitude at time $\omega t = \pi/2$ is illustrated for both $\mathcal{U} = 0$ and $\mathcal{U} = 0.625$ in figure 38. For $\epsilon > 0.25$, the distance of the front from the coastline and the intensity of the front both increase roughly linearly with the heating amplitude. Interestingly, the addition of the background wind leads to essentially no change in the propagation speed of the front, while the intensity of the front with the background wind is stronger.

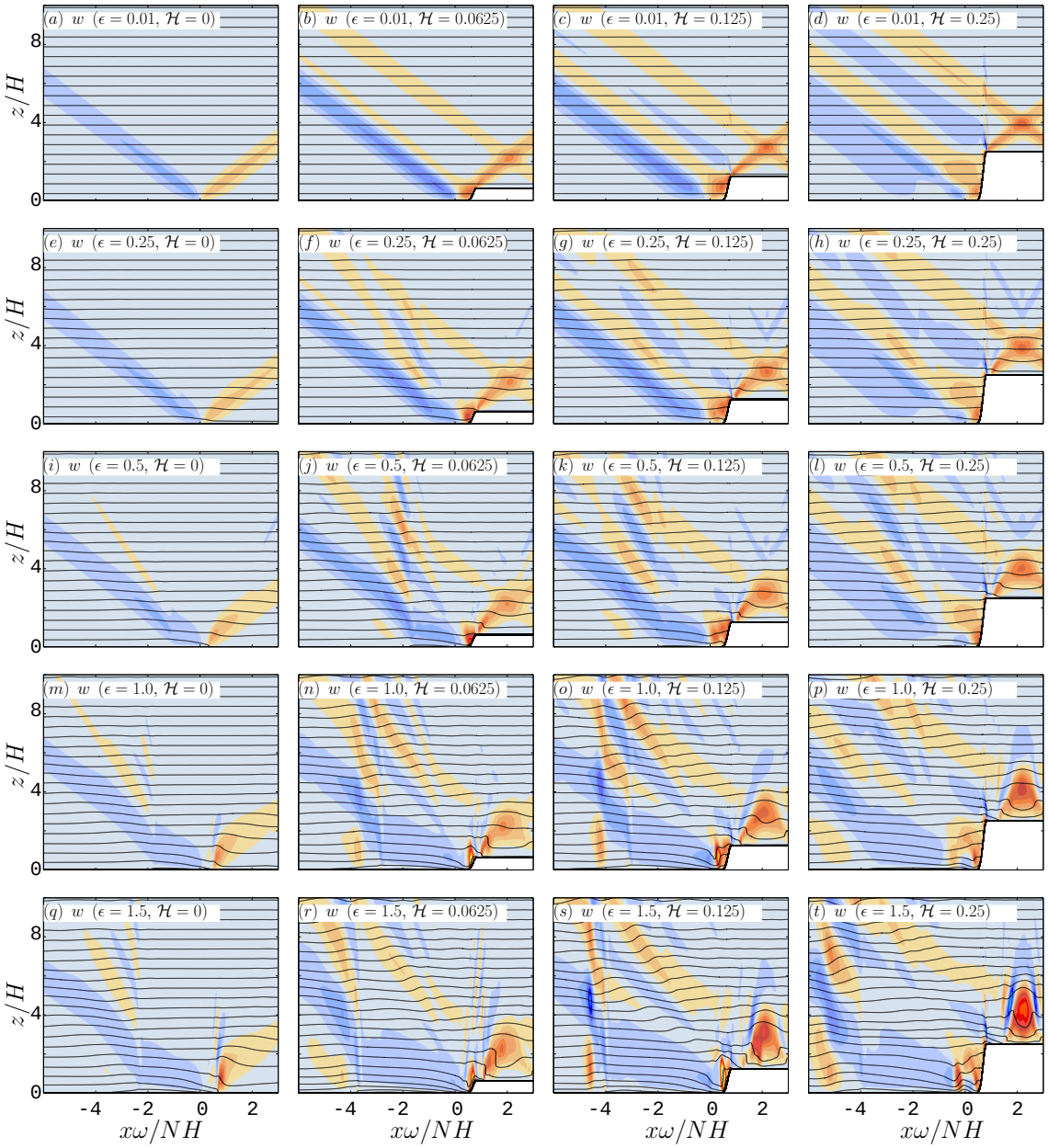

Fig. 33. Vertical velocity [c.i. $= 0.12$] for the case with the background wind $\mathcal{U} = 0$, different heating amplitude and topography height at time $\omega t = \pi/2$. Different heating amplitude ϵ are (a),(b),(c),(d) 0.01; (e),(f),(g),(h) 0.25; (i),(j),(k),(l) 0.5; (m),(n),(o),(p) 1; (q),(r), (s),(t) 1.5. The topography heights from left to right are 0, 0.0625, 0.125 and 0.25.

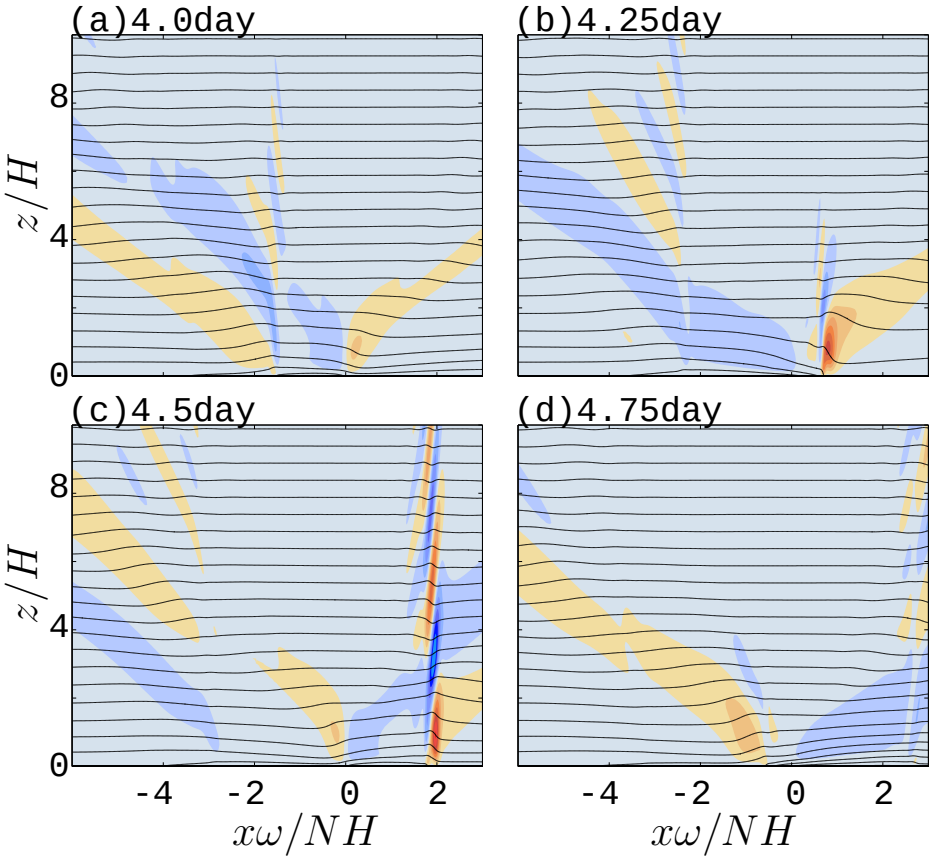

Fig. 34. Vertical velocity [c.i. = 0.12] for $\epsilon = 1.5$, $\mathcal{H} = 0$ and $\mathcal{U} = 0$ case at time (a) 4.0day; (b) 4.25day; (c) 4.5day; (d) 4.75day.

E. Summary

The effects of topography on the sea breeze were investigated from the linear and nonlinear perspectives by using a numerical model.

In the linear problem, adding topography introduces new wave disturbances over the slopes of the plateau. With no background wind this disturbance has a spatial structure similar to the sea breeze response. The amplitude of the disturbance increases with terrain height, with the disturbance amplitude as large as the sea breeze for the case $\mathcal{H} = 0.625$. Calculations with no coastline suggest that the disturbance is produced largely by the elevated heating gradients along the topography slopes.

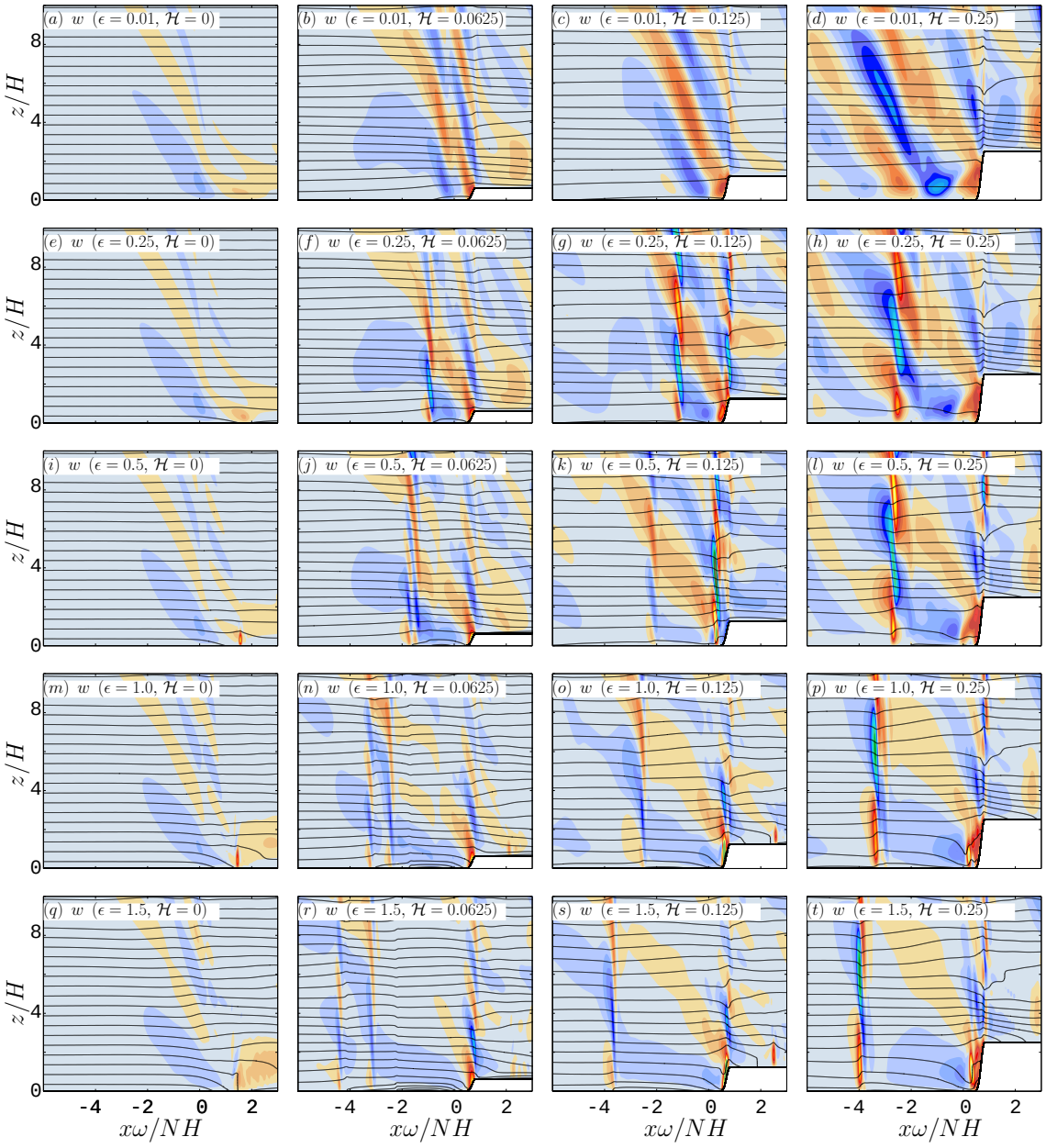

Fig. 35. Vertical velocity [c.i. = 0.12] for the case with background wind $\mathcal{U} = 0.625$, different heating amplitude and topography height at time $\omega t = \pi/2$. Different heating amplitude ϵ are (a),(b),(c),(d) 0.01; (e),(f),(g),(h) 0.25; (i),(j),(k),(l) 0.5; (m),(n),(o),(p) 1; (q),(r), (s),(t) 1.5. The topography heights from left to right are 0, 0.0625, 0.125 and 0.25.

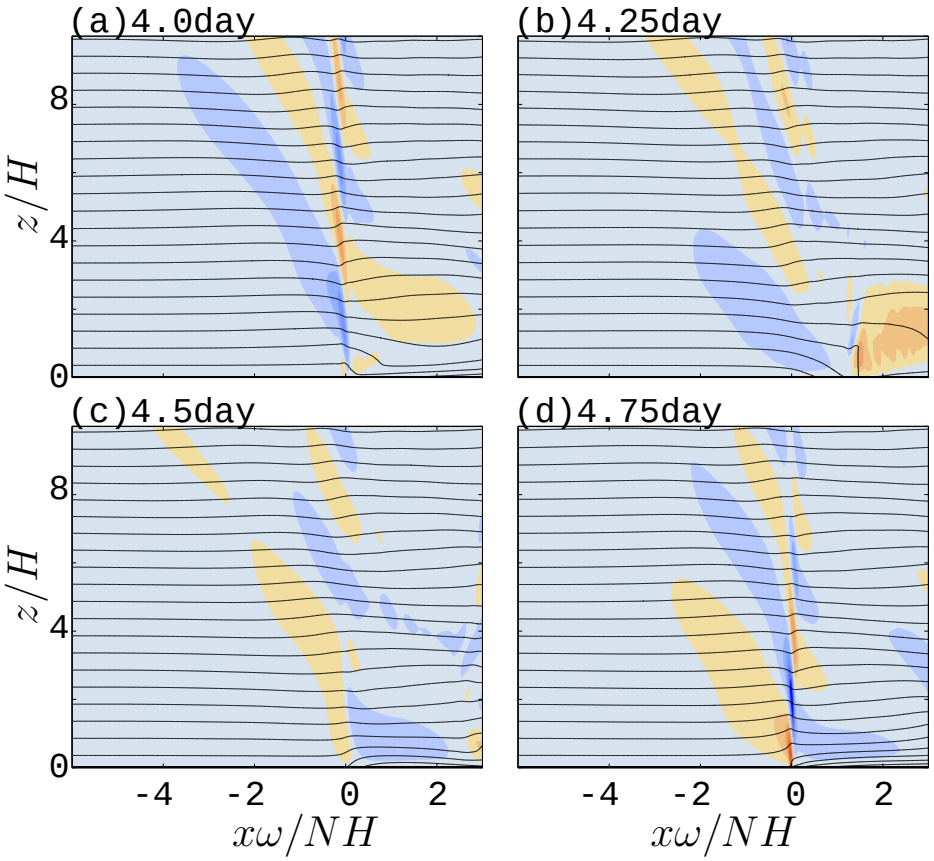

Fig. 36. Vertical velocity for $\epsilon = 1.5$ and $\mathcal{U} = 0.625$ case at time (a) 4.0day; (b) 4.25day; (c) 4.5day; (d) 4.75day.

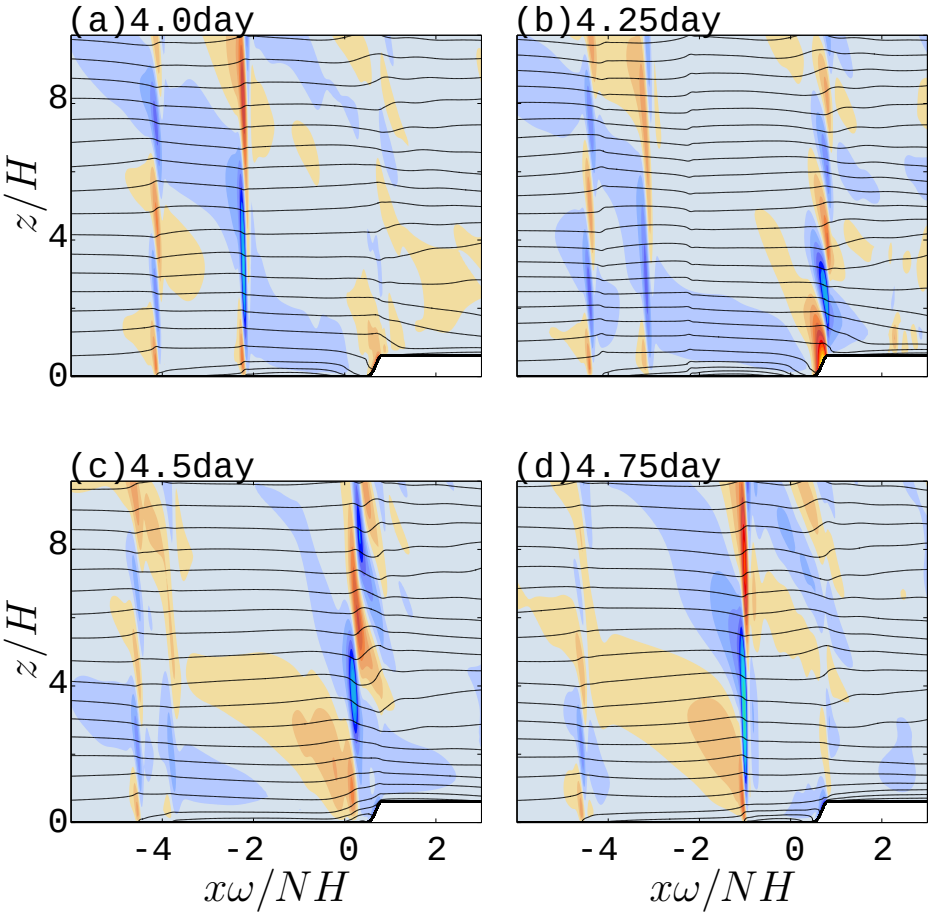

Fig. 37. Vertical velocity for $\epsilon = 1.5$, $\mathcal{U} = 0.625$ and $\mathcal{H} = 0.625$ at time (a) 4.0day; (b) 4.25day; (c) 4.5day; (d) 4.75day.

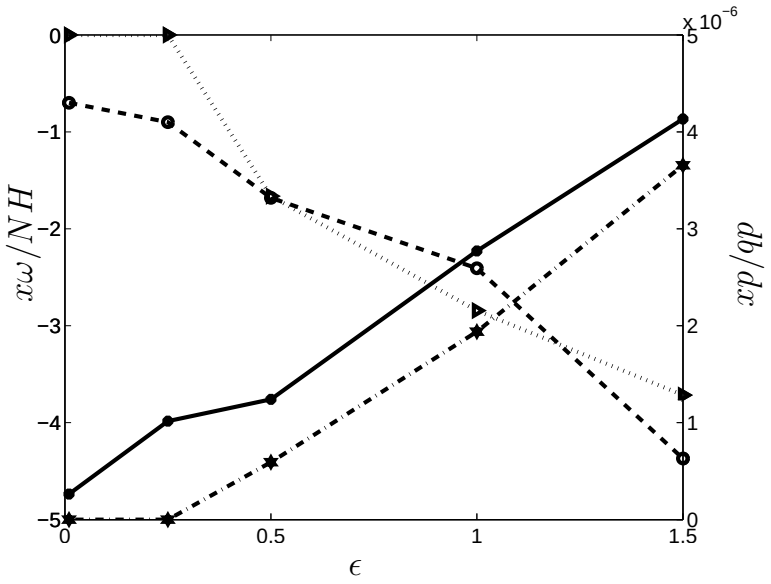

Fig. 38. Position (circle-dash line) and intensity (star-solid line) of the front at time $t = \pi/2$ for the case $\mathcal{U} = 0.625$ and position (triangle-dotted line) and intensity (hexagram-dashdot line) of the front at time $t = \pi/2$ for the case $\mathcal{U} = 0$

When background wind is added to the linear problem, the disturbance produced by the terrain is located directly above the topography slopes. Diagnostic calculations show that for small terrain heights the disturbance is mainly due to the other two terrain effects mentioned in section A, i.e., the flow of the sea breeze over the terrain slope and the interaction between the sea breeze and the background mountain wave. Different from the hypothesis of [42], the linear wave generation by the elevated heating gradient in this problem was found to be negligible

Several nonlinear experiments were considered to provide some preliminary insight into the nonlinear phenomena. In the nonlinear results, fronts appear with increasing heating amplitude ϵ. In most cases, the propagation speed and intensity of the fronts are largely determined by ϵ and not the terrain height. However, for the case with $\mathcal{U} = 0.625$ the leftward propagating front was found only when the terrain height was sufficiently large. In the case with $\mathcal{U} = 0$, the wave beam intersection

over the top of the plateau in the linear simulations is found to trigger convective overturning in the nonlinear results.

CHAPTER VI

SUMMARY AND DISCUSSION

A. Discussion for Wave Breaking over Terrain

The wave-turbulence interactions in a breaking mountain wave were investigated using an ensemble of 40 high-resolution wave-breaking calculations for 3D flow past a 2D ridge. The TKE budget, turbulent fluxes, PV fluxes and the dependence of the turbulent fluxes on grid spacing in the breaking mountain wave were all explored. A detailed summary of the results can be found in chapter II, section G.

It is worth pointing out that our conclusions for this study have a number of limitations First, as discussed in [9] and [106], the flow past the 2D obstacle misses some important dynamical phenomena found in the 3D topography case. Second, our narrow domain width limits the turbulent eddy spectrum in our calculations, which could potentially affect our turbulent mixing rates. Finally, the assumption of a free-slip surface oversimplifies the lower boundary condition. Adding a frictional surface layer would change the acceleration of the shooting flow and the shear production of TKE, as well as the associated mean-flow dissipation.

Future studies could address any of the topics in the previous paragraph. Perhaps the most important topic would be addressing the flow past 3D topography.

B. Discussion for Coastal Wave Generation

The effect of background wind and topography on the mesoscale wave response associated with the sea breeze was explored using linear theory calculations and idealized numerical modeling. The sea breeze dependence on background wind and coastal width was studied in the linear context using Fourier transform solutions. The re-

sults were then extended to include both terrain and nonlinearity using linear and nonlinear numerical model calculations. Summaries of the results can be found in chapter IV, section F and chapter V, section E.

Our sea breeze study is based on simplified and idealized models, which leads to certain limitations. First, our specification of an interior heat source is an over-simplification of the effects of boundary layer eddies. A more realistic study would consider fluxes of heat across the lower boundary. The heat source in our study is also strictly diurnal, whereas the real world features higher frequency components as well. Second, our study is limited to the non-rotating (or equatorial) case. The extension to higher latitudes would require the addition of the Coriolis force. Finally, our study completely neglects the effects of 3D coastlines.

The preliminary results for the nonlinear phenomena in chapter V, section D will be further diagnosed. Future work could then address any of the topics mentioned in the previous paragraph. Perhaps the most interesting work would be to consider the Coriolis effect on the sea breeze in a background wind.

REFERENCES

[1] J. W. Miles, "Lee waves in a stratified flow. Part II: Semi-circular obstacle," *J. Fluid Mech.*, vol. 33, pp. 803–814, 1968.

[2] I. P. Castro and W. H. Snyder, "Experiments on wave-breaking in stratified flow over obstacles," *J. Fluid Mech.*, vol. 255, pp. 195–211, 1993.

[3] P. G. Baines, *Topographic Effects in Stratified Flows*, Cambridge University Press, 1995.

[4] Q. Jiang and J. Doyle, "Gravity wave breaking over the central alps: Role of complex terrain," *J. Atmos. Sci.*, vol. 61, pp. 2249–2266, 2004.

[5] T. L. Clark, "Severe downslope windstorm calculations in two and three spatial dimensions using anelastic interactive grid nesting: A possible mechanism for gustness," *J. Atmos. Sci.*, vol. 41, pp. 329–350, 1984.

[6] R. B. Smith, "Aerial observations of the Yugoslavian bora," *J. Atmos. Sci.*, vol. 44, pp. 269–297, 1987.

[7] R. Smith, J. Paegle, T. Clark, W. Cotton, D. Durran, G. Forbes, J. Marwitz, C. Mass, J. McGinley, H. Pan, and M. Ralph, "Local and remote effects of mountains on weather: Research needs and opportunities," *Bull. AMS*, vol. 78, pp. 877–892, 1997.

[8] C. Schär and R. B. Smith, "Shallow-water flow past isolated topography. Part I: Vorticity production and wake formation," *J. Atmos. Sci.*, vol. 50, pp. 1373–1400, 1993.

[9] C. Schär and D. R. Durran, "Vortex formation and vortex shedding in continously stratified flows past isolated topography," *J. Atmos. Sci.*, vol. 54, pp. 534–554, 1997.

[10] R. Rotunno, V. Grubišić, and P. K. Smolarkiewicz, "Vorticity and potential vorticity in mountain wakes," *J. Atmos. Sci.*, vol. 56, pp. 2796–2810, 1999.

[11] C. C. Epifanio and D. R. Durran, "Lee vortex formation in free-slip stratified flow over ridges. Part II: Mechanisms of vorticity and PV production in nonlinear viscous wakes," *J. Atmos. Sci.*, vol. 59, pp. 1166–1181, 2002.

[12] R. B. Smith, A. C. Gleason, and P. A. Gluhosky, "The wake of St. Vincent," *J. Atmos. Sci.*, vol. 54, pp. 606–623, 1997.

[13] Q. Jiang, R. B. Smith, and J. Doyle, "The nature of the mistral: Observations and modelling of two MAP events," *Quart. J. Roy. Meteor. Soc.*, vol. 189, pp. 857–877, 2003.

[14] Ya. D. Afanasyev and W. R. Peltier, "The three-dimensionalization of stratified flow over two-dimensional topography," *J. Atmos. Sci.*, vol. 55, pp. 19–39, 1998.

[15] Ø. Andreassen, P. Ø. Hvidsten, D. C. Gritts, and S. Arendt, "Vorticity dynamics in a breaking internal gravity wave. Part 1. initial instability evolution," *J. Fluid Mech.*, vol. 367, pp. 27–46, 1998.

[16] Ya. D. Afanasyev and W. R. Peltier, "Numerical simulations of internal gravity wave breaking in the middle atmosphere: The influence of dispersion and three-dimensionalization," *J. Atmos. Sci.*, vol. 58, pp. 132–153, 2001.

[17] E. Halley, "An historical account of the trade winds, and monsoons, observable in the seas between and near the tropicks, with an attempt to assign physical

cause of said winds.," *Phil. Trans. Roy. Soc. London*, vol. 16, pp. 153–168, 1686.

[18] E. L. Fisher, "An observational study of the sea breeze," *J. Meteor.*, vol. 17, pp. 645–660, 1960.

[19] W. M. Davis, G. Schultz, and R. D. Ward, "An investigation of the sea-breeze," *New Engl. Meteor. Soc. Obser.*, vol. 21, pp. 214–264, 1889.

[20] K. Finkele, J. M. Hacker, H. Kraus, and R. A. Byron-scott, "A complete sea-breeze circulation cell derived from aircraft observations," *Bound. Layer Met.*, vol. 73, pp. 299–317, 1995.

[21] E. Adams, "Four ways to win the sea breeze game," *Sailing World*, pp. 44–49, 1997.

[22] S. T. K. Miller, B. D. Keim, R. W. Talbot, and H. Mao, "Sea breeze: Structure, forecasting, and impacts," *Rev. Geoph.*, vol. 41, pp. 1–31, 2003.

[23] V. Puygrenier, F. Lohou, B. Campistron, F. Saïd, G. Pigeon, B. Bénech, and D. Serca, "Investigation of the fine structure of sea-breeze during escompte experiment," *Atmos. Res.*, vol. 74, pp. 329–353, 2005.

[24] H. Jeffreys, "On the dynamics of wind," *Quart. J. Roy. Meteor. Soc.*, vol. 48, pp. 29–46, 1922.

[25] B. Haurwitz, "Comments on the sea-breeze circulation," *J. Meteor.*, vol. 4, pp. 1–8, 1947.

[26] F. H. Schmidt, "An elementary theory of the land- and sea-breeze circulation," *J. Meteor.*, vol. 4, pp. 9–15, 1947.

[27] W. J. Pierson, "The effects of eddy viscosity, coriolis deflection, and temperature fluctuation on the sea breeze as a function of time and height," *Meteor. Pap., College of Engineering, New York University*, vol. 1, pp. 30, 1950.

[28] F. Defant, *Compendium of Meteorology*, American Meteorological Society, Boston, 1951.

[29] J. E. Walsh, "Sea breeze theory and applications," *J. Atmos. Sci.*, vol. 31, pp. 2012–2026, 1974.

[30] R. P. Pearce, "The calculation of a sea-breeze circulation in terms of the differential heating across the coast line," *Quart. J. Roy. Meteor. Soc.*, vol. 81, pp. 351–391, 1955.

[31] R. P. Pearce, R. C. Smith, and J. S. Malkus, "The calculation of a sea-breeze circulation in terms of the differential heating across the coast line," *Quart. J. Roy. Meteor. Soc.*, vol. 82, pp. 235–241, 1956.

[32] M. A. Estoque, "A theoretical investigation of the sea breeze," *Quart. J. Roy. Meteor. Soc.*, vol. 86, pp. 523–534, 1961.

[33] E. L. Fisher, "An theoretical study of the sea breeze," *J. Meteor.*, vol. 18, pp. 216–233, 1961.

[34] J. E. Simpson, *Gravity Currents in the Environment and the Laboratory*, vol. 4, Cambridge Univ. Press, New York, 1997.

[35] A. Cenedese, M. Miozzi, and P. Monti, "A laboratory investigation of land and sea breeze regimes," *Experiments in Fluids*, vol. 29, pp. 291–299, 2000.

[36] W. Y. Sun and I. Orlanski, "Large scale convection and sea breeze circulation. Part I: Stability analysis," *J. Atmos. Sci.*, vol. 38, pp. 1675–1693, 1981.

[37] R. Rotunno, "On the linear theory of the land and sea breeze," *J. Atmos. Sci.*, vol. 40, pp. 1999–2009, 1983.

[38] H. Yan and R. A. Anthes, "The effect of latitude on the sea breeze," *Mon. Wea. Rev.*, vol. 115, pp. 936–956, 1987.

[39] G. A. Dalu and R. A. Pielke, "An analytical study of the sea breeze," *J. Atmos. Sci.*, vol. 46, pp. 1815–1825, 1989.

[40] G. Yang and J. Slingo, "The diurnal cycle in the tropics," *Mon. Wea. Rev.*, vol. 129, pp. 784–801, 2001.

[41] B. E. Mapes, T. T. Warner, and M. Xu, "Diurnal patterns of rainfall in northwestern South America. Part I: Observations and context," *Mon. Wea. Rev.*, vol. 131, pp. 799–812, 2003.

[42] B. E. Mapes, T. T. Warner, and M. Xu, "Diurnal patterns of rainfall in northwestern South America. Part III: Diurnal gravity waves and nocturnal convection offshore," *Mon. Wea. Rev.*, vol. 131, pp. 830–844, 2003.

[43] C. C. Epifanio and T. Qian, "Wave-turbulence interactions in a breaking mountain wave," *J. Atmos. Sci.*, vol. 65, pp. 3139–3158, 2008.

[44] T. Qian, C. C. Epifanio, and F. Zhang, "Linear theory calculations for the sea breeze in a background wind: The equatorial case," *JAS*, 2009, in press.

[45] G. Lyra, "Theorie der stationären leewellenströngmung in freier atmosphäre," *Z. Angew. Math. Mech.*, vol. 23, pp. 1–28, 1943.

[46] P. Queney, "Theory of perturbations in stratified currents with applications to airflow over mountain barriers," in *Misc. Report No. 23*. Univ. of Chicago, 1947.

[47] R. S. Scorer, "Theory of lee waves of mountains," *Quart. J. Roy. Meteor. Soc.*, vol. 75, pp. 41–56, 1949.

[48] G. D. Crapper, "A three dimensional solution for waves in the lee of mountains," *J. Fluid Mech.*, vol. 6, pp. 51–76, 1959.

[49] R. B. Smith, "Linear theory of stratified hydrostatic flow past an isolated mountain," *Tellus*, vol. 32, pp. 348–364, 1980.

[50] A. Eliassen and E. Palm, *On the transfer of energy in stationary mountain waves.*, Geofysiske Publikasjoner, Norway, 1960, 23 pp.

[51] R. R. Long, "Some aspects of the flow of stratified fluids. I. A theoretical investigation," *Tellus*, vol. 5, pp. 42–58, 1953.

[52] R. R. Long, "Some aspects of the flow of stratified fluids. III. Continuous density gradient," *Tellus*, vol. 7, pp. 341–357, 1955.

[53] R. B. Smith, "The steepening of hydrostatic mountain waves," *J. Atmos. Sci.*, vol. 34, pp. 1634–1654, 1977.

[54] D. K. Lilly and E. J. Zipser, "The Front Range windstorm of 11 January 1972: A meteorological narrative," *Weatherwise*, vol. 25, pp. 56–63, 1972.

[55] D. K. Lilly, "A severe downslope windstorm and aircraft turbulence event induced by a mountain wave," *J. Atmos. Sci.*, vol. 35, pp. 59–77, 1978.

[56] J. D. Doyle, M. A. Shapiro, Q. Jiang, and D. L. Bartels, "Large-amplitude mountain wave breaking over Greenland," *J. Atmos. Sci.*, vol. 62, pp. 3106–3126, 2005.

[57] T. L. Clark and W. R. Peltier, "On the evolution and stability of finite-amplitude mountain waves," *J. Atmos. Sci.*, vol. 34, pp. 1715–1730, 1977.

[58] J. B. Klemp and D. K. Lilly, "Numerical simulation of hydrostatic mountain waves," *J. Atmos. Sci.*, vol. 35, pp. 78–107, 1978.

[59] D. R. Durran and J. B. Klemp, "Another look at downslope winds. Part II: Nonlinear amplification beneath wave-overturning layers," *J. Atmos. Sci.*, vol. 44, pp. 3402–3412, 1987.

[60] R. B. Smith, "On severe downslope winds," *J. Atmos. Sci.*, vol. 42, pp. 2597–2603, 1985.

[61] R. T. Pierrehumbert and B. Wyman, "Upstream effects of mesoscale mountains," *J. Atmos. Sci.*, vol. 42, pp. 977–1003, 1985.

[62] H. Ólafsson and P. Bougeault, "Nonlinear flow past an elliptic mountain ridge," *J. Atmos. Sci.*, vol. 53, pp. 2465–2489, 1996.

[63] C. C. Epifanio and D. R. Durran, "Three-dimensional effects in high-drag-state flows over long ridges," *J. Atmos. Sci.*, vol. 58, pp. 1051–1065, 2001.

[64] W. R. Peltier and T. L. Clark, "The evolution and stability of finite-amplitude mountain waves. Part II: Surface wave drag and severe downslope windstorms," *J. Atmos. Sci.*, vol. 36, pp. 1498–1529, 1979.

[65] T. L. Clark, D. H. William, and M. B. Robert, "Two- and three-dimensional simulations of the 9 January 1989 severe Boulder windstorm: Comparison with observations," *J. Atmos. Sci.*, vol. 51, pp. 2317–2343, 1994.

[66] C. C. Epifanio and D. R. Durran, "Lee vortex formation in free-slip stratified flow over ridges. Part I: Comparison of weakly nonlinear inviscid theory and

fully nonlinear viscous simulations," *J. Atmos. Sci.*, vol. 59, pp. 1153–1165, 2002.

[67] D. C. Fritts, J. R. Isler, and Ø. Andreassen, "Gravity wave breaking in two and three dimensions, 2. Three-dimensional evolution and instability structure," *J. Geophys. Res.*, vol. 99, pp. 8109–8123, 1994.

[68] A. E. Gill, *Atmosphere-Ocean Dynamics*, Academic Press, San Diego, 1982, 662 pp.

[69] P. H. Haynes and M.E. McIntyre, "On the evolution of vorticity and potential vorticity in the presence of diabatic heating and frictional or other forces," *J. Atmos. Sci.*, vol. 44, pp. 828–841, 1987.

[70] M. E. McIntyre and W. A. Norton, "Dissipative wave-mean interactions and the transport of vorticity or potential vorticity," *J. Fluid Mech.*, vol. 212, pp. 403–435, 1990.

[71] R. B. Smith, "Mountain induced stagnation points in hydrostatic flow," *Tellus*, vol. 41A, pp. 270–274, 1989.

[72] C. Schär, "A generalization of Bernoulli's theorem," *J. Atmos. Sci.*, vol. 50, pp. 1437–1443, 1993.

[73] C. Schär, M. Sprenger, D. Lüthi, Q. Jiang, R. B. Smith, and R. Benoit, "Structure and dynamics of an Alpine potential-vorticity banner," *Quart. J. Roy. Meteor. Soc.*, vol. 189, pp. 825–856, 2003.

[74] V. Grubišić, "Bora-driven potential vorticity banners over the Adriatic.," *Quart. J. Roy. Meteor. Soc.*, vol. 130, pp. 2571–2603, 2004.

[75] C. Flamant, E. Richard, C. Schär, R. Rotunno, L. Nance, M. Sprenger, and R. Benoit, "The wake south of the Alps: Dynamics and structure of the lee-side flow and secondary potential vorticity banners," *Quart. J. Roy. Meteor. Soc.*, vol. 130, pp. 1275–1304, 2004.

[76] K. B. Winters and E. A. D'Asaro, "Three-dimensional wave breaking near a critical level," *J. Fluid Mech.*, vol. 272, pp. 255–284, 1994.

[77] D. C. Fritts, J. F. Garten, and Ø. Andreassen, "Wave breaking and transition to turbulence in stratified shear flows," *J. Atmos. Sci.*, vol. 53, pp. 1057–1085, 1996.

[78] P. J. Mason, "Large-eddy simulation: A critical review of the technique," *Quart. J. Roy. Meteor. Soc.*, vol. 120, pp. 1–26, 1994.

[79] B. Stevens, C.-H. Moeng, and P. P. Sullivan, "Large-eddy simulations of radiatively driven convection: Sensitivi ties to the representation of small scales," *J. Atmos. Sci.*, vol. 56, pp. 3963–3984, 1999.

[80] J. R. Holton, *An Introduction to Dynamic Meteorology*, Academic, San Diego, CA, ninth edition, 1992.

[81] J. E. Simpson, "A comparison between laboratory currents and atmospheric density currents," *Quart. J. Roy. Meteor. Soc.*, vol. 95, 1969.

[82] W. L. Physick and R. K. Smith, "Observations and dynamics of sea-breezes in northern Australia," *Aust. Meteor. Mag*, vol. 33, pp. 51–63, 1985.

[83] R. Wood, I. M. Stromberg, and P. R. Jonas, "Aircraft observations of sea-breeze frontal structure," *Quart. J. Roy. Meteor. Soc.*, vol. 125, pp. 1959–1995, 1999.

[84] S. Zhong and E. S. Takle, "An observational study of sea- and land-breeze circulation in an area of complex coastal heating," *J. App. Met.*, vol. 31, pp. 1426–1438, 1992.

[85] P. Rao and H. E. Fuelberg, "An investigation of convection behind the cape canaveral sea-breeze front," *Mon. Wea. Rev.*, vol. 128, pp. 3437–3458, 2000.

[86] R. A. Pielke, A. Song, P. J. Michaels, W. A. Lyons, and R. W. Arritt, "The predictability of sea-breeze generated thunderstorms," *Atmosfera*, vol. 4, pp. 65–78, 1991.

[87] T. N. Atkins, R. M. Wakimoto, and T. M. Weckwerth, "Observations of the sea-breeze front during cape, Part II: Dual-doppler and aircraft analysis," *Mon. Wea. Rev.*, vol. 123, pp. 944–969, 1995.

[88] W. A. Lyons and L. E. Olsson, "Detailed mesometeorological studies of air pollution dispersion in the Chicago lake breeze," *Mon. Wea. Rev.*, vol. 101, pp. 387–403, 1973.

[89] F. Bastin, P. Drobinski, A. Dabin, P. Delville, and O. Reitebuc C. Wemer, "Impact of the Rhone and Durance valleys on sea-breeze circulation in the Marseille area," *Atmospheric Research*, vol. 74, pp. 303–328, 2005.

[90] M. A. Estoque, "The sea breeze as a function of the prevailing synoptic situation," *J. Atmos. Sci.*, vol. 19, pp. 244–250, 1962.

[91] R. W. Arritt, "Effects of the large-scale flow on characteristic features of the sea breeze," *J. Atmos. Sci.*, vol. 32, pp. 116–125, 1993.

[92] O. Chiba, "The turbulent characteristics of the lowest part of sea breeze front in the atmospheric surface layer," *Bound. Layer Met.*, vol. 65, pp. 181–195,

1993.

[93] C. G. Helmis, D. N. Asimakopoulos, D. G. Deligiorgi, and D. P. Lalas, "Observations of sea-breeze fronts near the shoreline," *Bound. Layer Met.*, vol. 38, pp. 395–410, 1987.

[94] R. M. Wakimoto and Nolan T. Atkins, "Observations of the sea-breeze front during cape. Part I: Single-doppler, satellite, and cloud photogrammetry analysis," *Mon. Wea. Rev.*, vol. 122, pp. 1092–1114, 1994.

[95] J. E. Simpson, *Sea Breeze and Local Wind*, Cambridge Univ. Press, New York, 1994.

[96] W. Y. Sun and I. Orlanski, "Large scale convection and sea breeze circulation. Part II: Nonlinear numerical model," *J. Atmos. Sci.*, vol. 38, pp. 1694–1706, 1981.

[97] T. T. Warner, B. E. Mapes, and M. Xu, "Diurnal patterns of rainfall in northwestern South America. Part II: Model simulation," *Mon. Wea. Rev.*, vol. 131, pp. 813–829, 2003.

[98] P. Zuidema, P. Davies, and R. Moroney C, "On the angular radiance closure of tropical cumulus congestus clouds observed by the multiangle imaging spectroradiometer," *J. Geophys. Res.*, vol. 108, pp. 1426–1438, 2003.

[99] P. Zuidema, "Convective clouds over the Bay of Bengal," *Mon. Wea. Rev.*, vol. 131, pp. 780–798, 2003.

[100] C. Vera, "Toward a unified view of the American Monsoon Systems," *Journal of Climate*, vol. 19, pp. 4977–5000, 2006.

[101] Y. L. Lin, *Mesoscale Dynamics*, Cambridge University Press, 2007.

[102] D. J. Muraki, "Revisiting Queney's flow over a mesoscale ridge," *in Ninth Conf. on Mountain Meteorology, Aspen, CO, Amer. Meteor. Soc.*, vol. 5.3, 2000, Preprints.

[103] M. Abramowitz and I. A. Stegun, *Handbook of Mathematical Functions*, Dover Publications, New York, ninth edition, 1972.

[104] Y. Lee, D. J. Muraki, and D. E. Alexander, "A resonant instability of steady mountain waves," *J. Fluid Mech.*, vol. 568, pp. 303–327, 2006.

[105] K. R. Walter, "The nonlinear dynamics of the sea breeze," M.S. thesis, Texas A & M University, 2004.

[106] C. C. Epifanio and R. Rotunno, "The dynamics of orographic wake formation in flows with upstream blocking," *J. Atmos. Sci.*, vol. 62, pp. 3127–3150, 2005.

VITA

My name is Tingting Qian. I received my B.S. in Atmospheric Science from Nanjing University in 2001, and my M.S. in Atmospheric Science from Peking University in 2004. I received my Ph.D. from Texas A&M University in May 2009. My research interests focus on mesoscale gravity wave dynamics. I plan to find a job in Beijing, China. I can be reached at the following address through my husband, Duozhi Zhu: 29 Jinrong Ave. Xicheng District, Beijing 100032, China. My email address is qttpeking@hotmail.com.

The typist for this dissertation was Tingting Qian.